Time-resolved terahertz spectroscopy of semiconductor nanostructures

Porte, Henrik

Publication date:
2011

Document Version
Publisher's PDF, also known as Version of record

Time-resolved terahertz spectroscopy of semiconductor nanostructures

Henrik Porte

Time-resolved terahertz spectroscopy of semiconductor nanostructures

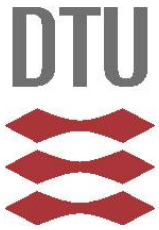

by

Hendrik Pieter Porte

April 28, 2011

Submitted in accordance with the requirement for the degree of Doctor of Philosophy.

Technical University of Denmark
DTU Fotonik - Department of Photonics Engineering

Supervisors:
Proffesor Peter Uhd Jepsen
Dr. Dmitry Turchinovich

Time-resolved terahertz spectroscopy of semiconductor nanostructures

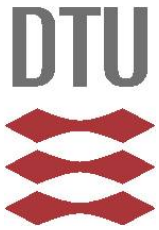

by

Hendrik Pieter Porte

July 2011

Submitted in accordance with the requirement for the degree of Doctor of Philosophy.

Technical University of Denmark
DTU Fotonik - Department of Photonics Engineering

Supervisors:
Professor Peter Uhd Jepsen
Associate Professor Dmitry Turchinovich

Abstract

This thesis describes time-resolved terahertz spectroscopy measurements on various semiconductor nanostructures. The aim is to study the carrier dynamics in these nanostructures on a picosecond timescale. In a typical experiment carriers are excited with a visible or near-infrared pulse and by measuring the transmission of a terahertz probe pulse, the photoconductivity of the excited sample can be obtained. By changing the relative arrival time at the sample between the pump and the probe pulse, the photoconductivity dynamics can be studied on a picosecond timescale.

The first studied semiconductor nanostructures are InGaAs/GaAs quantum dots. By exciting carriers into the GaAs barrier, a fast decay of the photoconductivity after optical excitation is observed, due to trapping of charge carriers into the quantum dots. If the carriers were excited into the ground state of the quantum dots, a slow rise of the photoconductivity is observed, due the release of carriers from the quantum dots into the conducting barrier states.

Secondly, the carrier dynamics in InGaN/GaN quantum wells subject to a built-in piezoelectric field is described. An initial fast decay of the photoconductivity as the piezoelectric field is screened by the dipole field of the excited electron-hole pairs is observed. The decay of the photoconductivity slows down as the carriers recombine and the piezoelectric field is restored.

Finally, the photoconductivity dynamics in black silicon is described. Black silicon is microstructured silicon, which is in this case produced by laser annealing of amorphous silicon films. The amplitude and the decay time of the photoconductivity depends strongly on the method and annealing fluence used in the production process. Furthermore, it is shown that by adding copper to the black silicon, the decay time of the photoconductivity can be significantly reduced. Besides time-resolved terahertz spectroscopy measurement, optical transmission, Raman spectroscopy, scanning electron microscope, energy dispersive X-ray, and X-ray diffraction spectroscopy experiments on black silicon are presented.

Resumé

Denne afhandling omhandler tids-opløste terahertz spektroskopi målinger på forskelligartede halvleder nanostrukturer. Formålet er at studere ladninsbærerdynamikken i disse nanostrukturer på en picosekund tidsskala. I et typisk eksperiment exciteres ladningsbærere med en synlig eller nær-infrarød puls og ved at måle transmissionen af en terahertz probe puls kan fotokonduktiviteten af den exciterede prøve udledes. Ved at variere ankomsttidspunktet ved prøven for pumpe- og probepulsen relativt til hinanden, kan fotokonduktivitetsdynamikken studeres på en picosekund tidsskala.

De først undersøgte halvleder nanostrukturer er InGaAs/GaAs kvantepunkter. Ved at excitere ladningsbærere i GaAs barriere-laget observeres, på grund af indfangning af ladningsbærere i kvantepunkterne, et hurtigt henfald af fotokonduktiviteten efter optisk excitation. Når ladninsbærere exciteres til grundtilstanden for kvantepunkterne observeres en langsom forøgelse af fotokonduktiviteten på grund af frigivelse af ladningsbærere fra kvantepunkterne til de ledende elektrontilstande i barriere-laget.

Herefter beskrives fotokonduktivitetsdynamikken i InGaN/GaN kvantebrønde med et indbygget piezoelektrisk felt. Et hurtigt henfald af fotokonduktiviteten observeres til at starte med, da det piezoelektriske felt afskærmes af dipol-feltet fra de genererede elektron-hul-par. Henfaldsraten for fotokonduktiviteten falder derefter i takt med at ladningsbærerne rekombinerer og det piezoelektriske felt genoprettes.

Til sidst beskrives fotokonduktivitetsdynamikken i sort silicium. Sort silicium er mikrostruktureret silicium, som i dette tilfælde er fremstillet ved laser annealing af amorfe silicium film. Amplituden og henfaldstiden for fotokonduktiviteten afhænger kraftigt af den anvendte fluence og annealingmetode anvendt under produktionsprocessen. Endvidere vises det at henfaldstiden kan reduceres betydeligt ved at tilføje kobber til det sorte silicium. Udover tids-opløste terahertz spektroskopi målinger præsenteres optisk transmissions-, Raman spektroskopi-, skanning elektron mikroskopi-, 'energy dispersive X-ray´- samt røntgen-diffraktions-målinger på sort silicium.

Preface

Most results presented in thesis are obtained at DTU Fotonik - Department of Photonics Engineering, Technical University of Denmark.

The InGaAs/GaAs quantum dots (chapter 5) were provided by the group of E. U. Rafailov, School of Engineering, Physics and Mathematics, University of Dundee. The InGaN/GaN multiple quantum wells (chapter 6) were produced in the group of A. Hangleiter, Technical University Braunschweig. The black silicon samples (chapter 7) were produced in the group of M. J. Rose, School of Engineering, Physics and Mathematics, University of Dundee.

The scanning electron microscopy images of black silicon without copper and the Raman spectroscopy measurement, presented in chapter 7, were taken at the School of Engineering, Physics and Mathematics, University of Dundee. The author of this thesis was not directly involved in these measurements.

The scanning electron microscopy images of black silicon with copper, presented in chapter 7, were taken at DTU CEN - Center of Electron Nanoscopy, Technical University of Denmark.

The X-ray diffraction spectrometry measurements, presented in chapter 7, were performed at Risø DTU - National Laboratory for Sustainable Energy, Technical University of Denmark.

The PhD-project was financed by the Højteknologi-fonden (Danish National Advanced Technology Foundation) (2/3) and DTU Fotonik - Department of Photonics Engineering, Technical University of Denmark (1/3).

Hendrik Pieter Porte,
August 29, 2011

Contents

Part I

Terahertz spectroscopy

Chapter 1

Introduction

Terahertz (THz) radiation is part of the electromagnetic spectrum, laying between infrared and microwaves (Fig. 1.1). The THz region is not well defined, but is approximately from 0.1 - 10 or several tens of THz. This region is or was also known as the THz gap. The word "gap" comes from the situation in the beginning of the 1980s. At that time there was technology available to generate and detect light at every part of the electromagnetic spectrum, from radiowaves until X-ray, except light at THz frequencies. The question is should we still call it a gap? In the original meaning of the "THz gap", the answer is no. Several ways to generate and detect these THz waves have been developed. However in terms of commercialization and finding its way into the daily life of people, THz waves have still some catching up to do.

Within the scientific community, THz technology is a fast growing field and became a powerful spectroscopy tool. The THz field started in 1984, where Auston *et al.* used a photoconductive switch, a technology used to generate microwaves [1] and extended it into the THz frequency range [2, 3]. In the late 1980s this technique was further developed [4–6]. Not much later in the beginning of the 1990s an other technique was developed to reach THz frequencies. High frequency optical pulses were used to generate THz pulses by optical rectification in nonlinear crystals [7–9].

Because of the special properties of THz waves, like e.g. its sensitivity

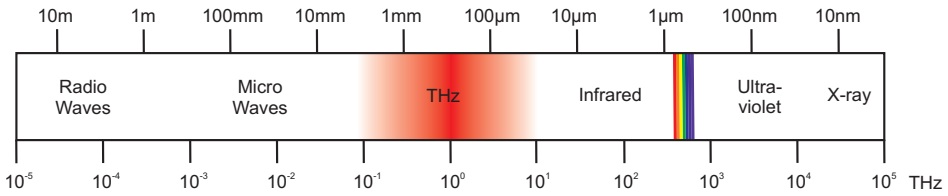

Figure 1.1: The electromagnetic spectrum. The THz region lays between microwaves and infrared.

to molecular vibration and free charge carriers, THz spectroscopy became a widely used spectroscopy technique to study both the static [10–13] as well as the dynamical [14–20] properties of a wide range of materials [21–27]. This thesis describes experiments where THz spectroscopy is used to study dynamical properties of semiconductor nanostructures. The availability to fabricate high quality semiconductor nanostructures improved the efficiency of many electrooptic devices like e.g light emitting diodes [28–30], semiconductor laser [31–35], solarcells [36–38] and photodetectors [39–43]. The reduced dimension of these nanostructures and quantum confinement of the charge carriers change the optical and electronic properties of the material. With THz spectroscopy the dynamic optic and electronic properties of semiconductor materials can be measured at a subpicosecond timescale which helps in understanding and improving these electooptic devices [44–51].

Light can be described with different units, like e.g. wavelength, frequency, and energy. In this thesis visible and infrared light are usually described by their wavelength, while the THz radiation will be described by its frequency. The conversion of THz into other units reads:

$$1 \text{ THz} \equiv 300 \ \mu\text{m} \equiv 4.14 \text{ meV} \equiv 33.3 \text{ cm}^{-1} \equiv 47.6 \text{ K}$$

This thesis consits of two parts. The first part is about the measurement technique THz spectroscopy. In chapter 2 the experimental setups used in the experiments are described. Special attention is taken into the mechanisms of generation and detecting broadband THz pulses. For describing the spectroscopy technique, first time-domain THz spectroscopy is explained (chapter 3), which can be used to measure the static properties of a material. To illustrate this technique, the refractive index of GaAs is measured. In the last chapter of the first part (chapter 4), the spectroscopy technique used for the experiments in this thesis, time-resolved THz spectroscopy is explained. Time-resolved THz spectroscopy can be used to measure the dynamical properties of a material. Again, GaAs is used to illustrate the method.

The second part is the experimental part. Three different semiconductor nano- or microstructures are studied. In chapter 5, the trapping of electrons into InGaAs quantum dots and the release of electrons from the quantum dots into the GaAs barriers is described. Chapter 6, describes the photoconductivity decay dynamics in biased InGaN/GaN quantum wells subject to the quantum confined Stark effect. The final chapter (7) is about a material called black silicon, where microstructures on the surface of a silicon film leads to an increased absorption of visible and infrared light. The main experiment on black silicon is THz spectroscopy, where the photoconductivity dynamics is investigated. In addition, Raman spectroscopy, optical transmission spectroscopy, electron microscopy, energy dispersive X-ray and X-ray diffraction spectroscopy experiments are described.

Chapter 2

Experimental setup

Although this thesis will describe experiments on different materials and structures, the measurement technique time-resolved THz spectroscopy will be the same. This chapter will describe the experimental setups that are used for the experiments described in this thesis. In the first section a description of the femtosecond laser used in all experiments is given, followed by a description of the generation and detection mechanisms of THz pulses. Various ways of generating and detecting terahertz radiation have been developed [52]. A short overview of these methods are presented. However, only the optical methods used in our experiments, i.e. optical rectification and free-space electro-optic sampling will be explained in more detail. This chapter ends with a detailed description of the entire setups. Two different setups will be shown, which both were used in the experiments described in this thesis.

2.1 Laser system

Ultrafast or broadband THz spectroscopy requires the generation of short THz pulses that span a broad frequency range. For generating and detecting a signal of 1 THz ($\equiv$ 1 ps) the laser pulses should be sub-ps. For generating and detecting higher frequencies, shorter pulses are needed. Therefore femtosecond lasers are generally used to generate and detect short broadband THz pulses. Although a different method has been developed recently [53], by using the equidistance frequency spacing between the different modes in a continuous wave semiconductor laser.

In our case Spectra physics' "Spitfire" system was used in the experiments. This is a combined laser system containing four parts: The "Millenia pro", the "Tsunami", the "Em-power" and the "Spitfire". The "Millennia pro" which is a Nd:YVO_4 laser pumped by diode lasers. The output wavelength of the "Millennia pro" (532 nm) is obtained by frequency doubling the typical 1064 nm lasing wavelength of the Nd:YVO_4 crystal in a nonlin-

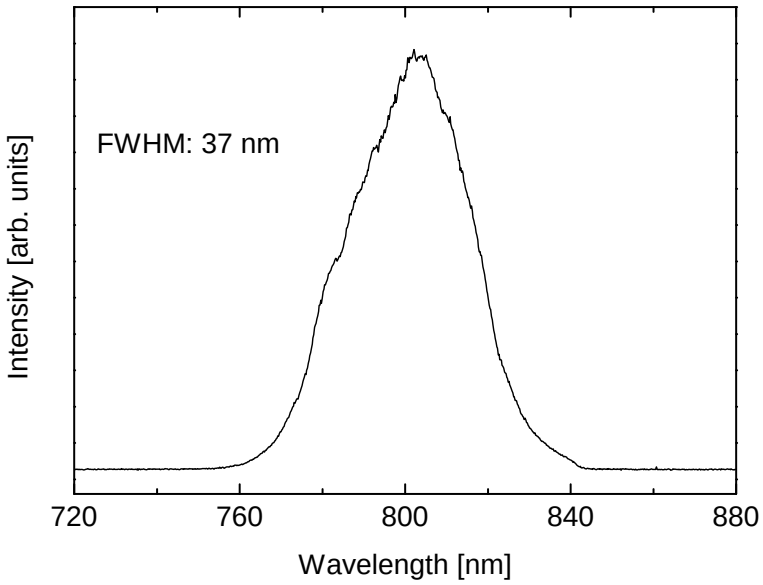

Figure 2.1: Spectrum of the generated laser pulses.

ear crystal. The 532 nm beam is used to pump a Ti:sapphire crystal in the "Tsunami". The Tsunami delivers ultrashort sub-100 fs pulses at a repetition rate of 80 MHz. The central wavelength is tunable by moving a slit through a by prisms expanded beam inside the laser. After the expansion, the different wavelenght are spatially overlapped by another set of prisms. In our case the laser central wavelength is kept at 800 nm. The output power of the Tsunami is approximately 600 mW at optimum operation. The Tsunami is used as a seed for the "Spitfire", which is a Ti:sapphire amplifier. The Ti:sapphire crystal is pumped by the "Em-power", which is Nd:YLF laser pumped by a series of diode lasers, The laser wavelength of 1053 nm is frequency doubled to the green (527 nm) to pump the Ti:sapphire crystal. In the Spitfire the pulses are amplified to a pulse energy of 3.5 mJ at a 1 kHz repetition rate. Due to the high energy the pulses are stretched before amplification and afterwards compressed again, thereby avoiding any damage to the Ti:sapphire crystal. The compression can be adjusted so that various pulse durations can be obtained. The shortest pulses that can be generated in this laser system is 35 fs, which corresponds to a peak power of 100 GW.

Fig. 2.1 shows the typical spectrum of the pulses from the "Spitfire". The broad spectrum with a full-width-half-maximum (FWHM) of 37 nm enables to generate broadband THz pulses. Fourier limited broad spectra translate in the time-domain to ultrashort pulses. Fig. 2.2 shows the autocorrelation of the laser pulses. Measuring the autocorrelation is a commonly used method to obtain the pulse duration of ultrashort pulses [54]. For the autocorrelation, the laser beam is split and mixed with itself in a nonlinear crystal, where

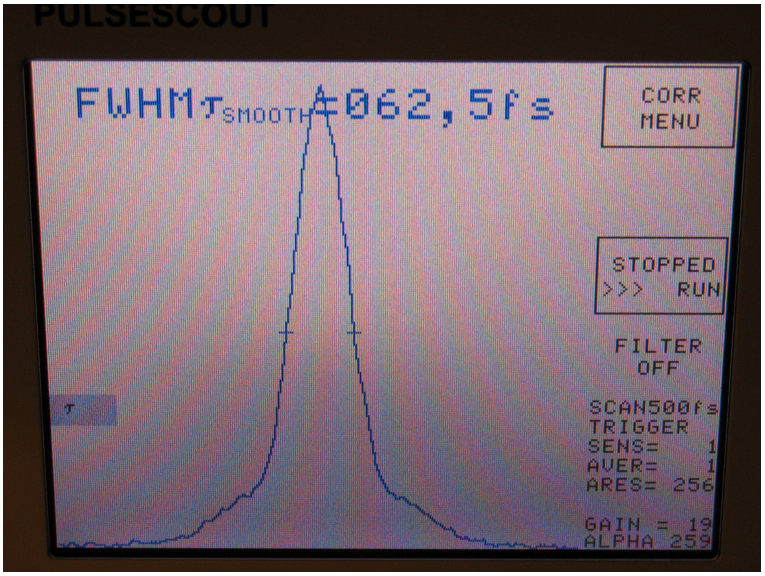

Figure 2.2: Autocorrelation of the generated laser pulses.

the second harmonic of the original beam is generated. One of the pulses can be delayed, thereby changing the temporal overlap between the pulses and hence the efficiency of the second harmonic generation. By using a non-collinear method, only the second harmonic that is generated when the pulses overlap in time is measured. For getting the real pulse duration, the FWHM of the autocorrelation should be divided by a form factor depending on the pulse shape. For a Gaussian pulse shape this factor is 1.414 [55]. So for a FWHM of 62.5 fs, the pulse duration of the Spitfire output is 44 fs.

Except directly using the 800 nm pulses from the laser, this thesis also describes experiments were a wavelength of 400 nm (chapter 6) and 1028 nm (chapter 5) were used. The 400 nm is generated by frequency doubling the 800 nm pulses in a Beta Barium Borate (BBO) crystal. For the generation of the 1028 nm pulses, an optical parametric amplifier (OPA) was used [56]. In an OPA part of the 800 nm beam is used to generate a white light continuum in a sapphire crystal. Part of the spectrum of the white light continuum is amplified by mixing it with the original 800 nm beam in a nonlinear crystal. The wavelength of the OPA can be chosen by changing the time delay between the 800 nm beam and the white light continuum. This will change with which part of the spectrum of the white light continuum it is mixed. The amplified signal is mixed with the original 800 nm beam in a nonlinear crystal again for a second amplification. As output, either the amplified signal or the idler beam can be used. The idler beam is generated in the second nonlinear crystal by difference frequency generation between the signal and the 800 nm beam. Together with the option of using

second harmonic generation, a broad wavelength range (0.4-20 μm) can be generated. An example of a spectrum from the OPA is shown in Fig. 5.4.

2.2 Generation of terahertz radiation

To understand how terahertz light can be generated, we have to look to some properties of light in general. Light is an electromagnetic wave that fulfill the wave equation.

$$\nabla^2 \overrightarrow{E} - \frac{1}{c^2}\frac{\partial^2 \overrightarrow{E}}{\partial t^2} = \mu_0 \left(\frac{\partial \overrightarrow{J}_q}{\partial t} + \frac{\partial^2 \overrightarrow{P}}{\partial t^2}\right), \tag{2.1}$$

where $\overrightarrow{E}$ is the electric field, c is the speed of light, μ_0 is the permeability of free space, $\overrightarrow{J}_q$ is the current from moving charges. The subscript is added to distinguish it with the displacement current $\overrightarrow{J}_{disp} = \partial \overrightarrow{P}/\partial t$, where $\overrightarrow{P}$ is the polarization. A derivation of this equation and its implications for the light-matter interaction in general will be given in ch. 3. From this equation it can be seen that there are two source terms for radiation and both can be applied to generate terahertz radiation.

First there is the change in the current or the acceleration of charges. This method is applied in the widely used photoconductive switches [1, 10]. Two electrodes are placed on a semiconductor material creating an electric field between them. A short laser pulse excite charge carriers in the semiconductor material that due to the present of an electric field will be accelerated. By using a femtosecond laser and the right material properties, these accelerated charges will emit photons at terahertz frequencies.

At the other side is optical rectification in a nonlinear crystal [7–9], where the terahertz photons are generated by a change in the polarization of a material. Since this method is used for all the THz experiments described in this thesis, this method will be explained in more detail. Besides the use of photoconductive switches and optical rectification, many more methods have been developed for the generation of light at terahertz frequencies: e.g. synchrotron radiation [57], free-electron lasers [58], quantum cascade lasers [31, 59], continuous wave terahertz generation by difference frequency generation in a semiconductor photomixer [60], and air-plasma generation [61, 62]. For more information about these methods, the reader is referred to the references.

Light-matter interaction can be described classically by the polarization generated in the material. The polarization is the dipole moment per unit volume. The induced polarization in the material can be with good approximation described with a power series to the electric field, where is assumed that no permanent dipoles are present.

$$P_i(\omega_i, k_i) = \varepsilon_0 \chi^{(1)}_{ij} E_j(\omega_j, k_j) + \chi^{(2)}_{ijk} \varepsilon_0 E_j(\omega_j, k_j) E_k(\omega_k, k_k) +$$

$$\chi^{(3)}_{ijkl}\varepsilon_0 E_j(\omega_j,k_j)E_k(\omega_k,k_k)E_l(\omega_l,k_l)..., \tag{2.2}$$

where the first term is the linear polarization which depends linear on the electric field, the second term is the quadratic polarization, depending quadratic on the electric field, etc. ε_0 is the electric permittivity of free space, $\chi^{(n)}$ is the susceptibility tensor of rank $n+1$, ω is the angular frequency and k is the wavevector. For any nonlinear effect, any of the higher order susceptibility tensors $n \geq 2$ should be nonzero. Optical rectification is a $\chi^{(2)}$ process, so for the generation of THz radiation a nonlinear crystal with a high $\chi^{(2)}$ value should be used.

For a traveling electromagnetic wave the electric field component can be described by

$$\overrightarrow{E}(\omega,k) = A(t)\exp[-i(\omega t - kz)] + c.c., \tag{2.3}$$

where $A(t)$ is the amplitude and $c.c. = A(t)^*\exp[i(\omega t - kz)]$ stands for complex conjugate. Note that for a continuous wave A is a constant, but for a short pulse it is time dependent. Now consider two electromagnetic waves $\overrightarrow{E}_1$ and $\overrightarrow{E}_2$ with angular frequencies ω_1 and ω_2, wavevectors k_1 and k_2 and amplitudes A_1 and A_2 respectively. If they interact in a nonlinear crystal with a nonzero $\chi^{(2)}$ component, according to Eq. 2.2, the induced quadratic polarization in the material reeds

$$\begin{aligned}
\overrightarrow{P}^{(2)}(\omega,k) &= \chi^{(2)}_{ijk}\varepsilon_0 \overrightarrow{E}_1(\omega_1,k_1)\overrightarrow{E}_2(\omega_2,k_2) \\
&= \chi^{(2)}_{ijk}\varepsilon_0(A_1(t)\exp[-i(\omega_1 t - k_1 z)] + c.c.)\cdot \\
&\quad (A_2(t)\exp[i(\omega_2 t - k_2 z)] + c.c.) \\
&= \chi^{(2)}_{ijk}\varepsilon_0(A_1(t)A_2^*(t)\exp[-\imath((\omega_1-\omega_2)t - (k_1-k_2)z)] + \\
&= c.c.) + (A_1(t)A_2(t)\exp[-i((\omega_1+\omega_2)t - (k_1+k_2)z)] + \\
&\quad c.c.).
\end{aligned} \tag{2.4}$$

As can be seen from Eq. 2.4, the frequency and wavevector of the induced quadratic polarization have two components, i.e. the sum of and the difference between the two original frequencies and wavevectors. This describes the process of sum and difference frequency generation.

Now consider there is only one electromagnetic wave, which means that $\omega = \omega_1 = \omega_2$, $k = k_1 = k_2$ and $A = A_1 = A_2$. Eq. 2.4 then becomes

$$\overrightarrow{P}^{(2)}(\omega,k) = (\chi^{(2)}_{ijk}\varepsilon_0 A(t)^2\exp[-i(2\omega t - 2kt)] + c.c) + 2\chi^{(2)}_{ijk}\varepsilon_0 A(t)A^*(t). \tag{2.5}$$

The first term has double the original frequency. This describes the process of second harmonic generation. From this equation follows also that the intensity of the generated second harmonic will depend quadratic on the

original intensity. The second term describes the process of optical rectification. For a continuous wave this term is constant, so a static polarization in the material is generated. However, for a short pulse the amplitude A is time dependent and hence the polarization will be time dependent. For a short laser pulse with a Gaussian pulse shape, the amplitude or the envelope of the wavepacket is described by

$$A(t) = E_0 \exp[-\frac{(t-t_0)^2}{2b^2}], \tag{2.6}$$

where E_0 is the amplitude or maximum electric field strength of the wavepacket, t_0 is the time of the center of the pulse and b is the pulse duration. Fig. 2.3(a) shows a pulse for $t_0 = 0$, $E_0 = 1$ and $b = 100$ fs. For a better visibility a longer wavelength than the actual 800 nm is used in this figure. If we put Eq. 2.6 into Eq. 2.5, the optical rectification term in $P^{(2)}$ reads

$$P^{(2)}(t) = 2\chi^{(2)}_{ijk}\varepsilon_0 E_0^2 \exp[-\frac{(t-t_0)^2}{b^2}]. \tag{2.7}$$

Fig. 2.3(b) shows the optical rectification term of the polarization induced by the pulse shown in Fig. 2.3(a), where all pre-constants are set to one. As explained before (Eq. 2.1) a time varying polarization leads to the generation of an electromagnetic wave, where the pulse shape is proportional to the second order time-derivative of the induced polarization. The second order time-derivative of the polarization (Fig. 2.3(b)) is shown in Fig. 2.3(c). The spectrum of this pulse is shown in Fig. 2.3(d). As shown from the spectrum of this pulse, the optical rectification of a femtosecond pulse in a nonlinear crystal leads to radiation at terahertz frequencies. These simple calculations show that a 100 fs long pulse can generate light up to ~ 50 THz (Fig. 2.3(d)). Although in most cases the crystal properties will prevent the generation of these high frequencies. Very large bandwidths have been generated by different frequency mixing in a thin GaSe crystal [63]. Using a longer pulse duration will shift the spectrum to lower frequencies. However, this can increase the efficiency if a better overlap between the maximum bandwidth that can be generated for a given pulse duration and the maximum bandwidth that can be generated based on the crystal properties is created.

The energy of the generated THz photons comes from a small red-shift of the original pulse. Every time a THz photon with energy $\hbar\omega$ is generated a pump photon shift its energy to a $\hbar\omega$ lower value. Every pump photon can generate multiple photons by a cascaded process [64].

How efficient THz light can be generated depends on two important parameters. First, the second order nonlinear susceptibility $\chi^{(2)}$. A higher $\chi^{(2)}$ leads to a stronger induced polarization and hence a higher THz electric field strength. The second is phase-matching between the optical and the generated THz beam. Some nonlinear crystals with a high $\chi^{(2)}$ coefficient

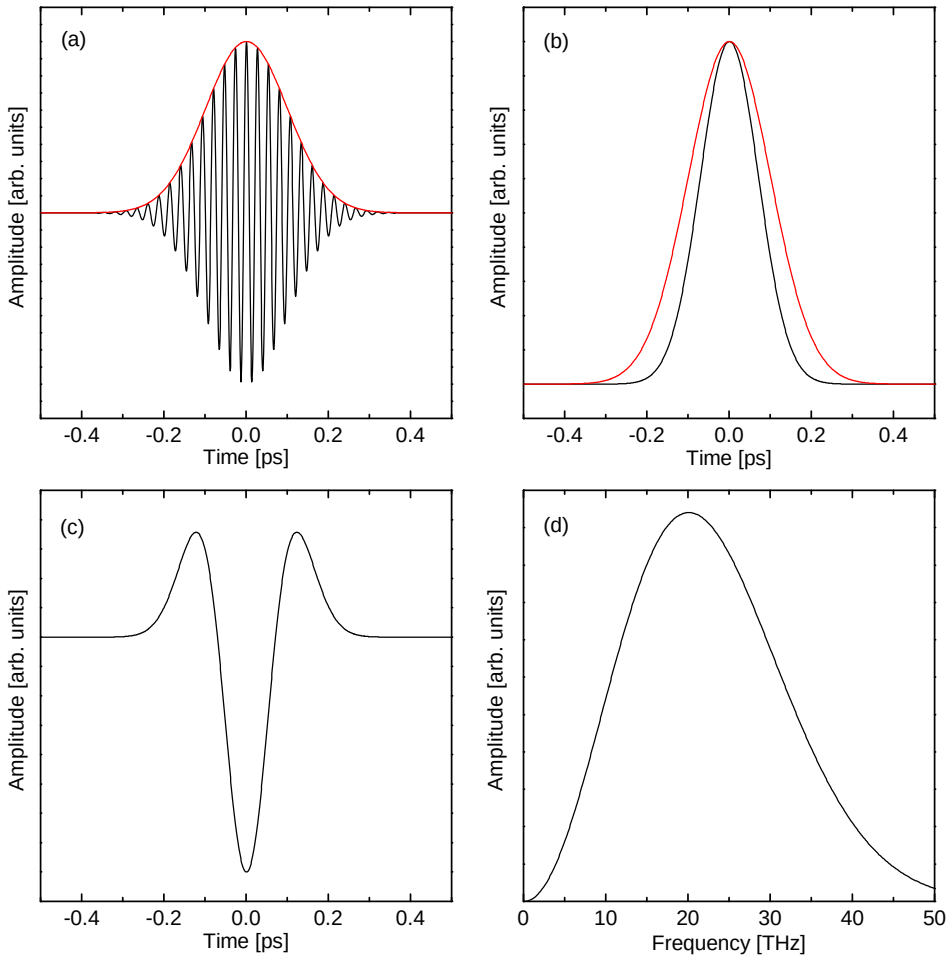

Figure 2.3: (a) Gaussian pulse with a pulse duration b of 100 fs (black line), envelope wavefunction of the gaussian pulse (red line). (b) Envelope wavefunction squared (black line) which is the optical rectification term of the induced polarization, envelope wavefunction (red line). (c) Second order time-derivative of the polarization shown in (b). It shows the shape of a generated THz pulse. (d) Fourier transform of the pulse shown in (c). Frequencies in the THz regime are generated.

like BBO are very efficient in second harmonic generation but very poor THz emitters, because there is a large phase mismatch between the optical beam and the optical rectified signal. Besides there are several optical phonon modes in the THz frequency regime [65]. Phase matching means that the wavevectors of the optical beam and the terahertz beam $k = \omega/c \cdot n(\omega)$ are such that conservation of impulse is fulfilled. Since conservation of impulse is always required, a mismatch leads to generation of terahertz light at different phases that can destructively interfere and hence limited the generation efficiency. Other nonlinear crystals like ZnTe are efficient in generating THz radiation, where there is good collinear phase matching for optical rectification at a certain wavelength. ZnTe is widely used for generation because of good phasematching conditions between THz frequecies and the 800 nm output of a Ti:sapphire laser. For other materials that offer good electro-optic properties like $LiNbO_3$, no collinear phase mathching can be achieved. However by periodically pole the crystal [66, 67] or using a tilted pulse front [68, 69], THz pulses can be generated. The amplitude and spectrum that is generated depends not only on phase matching, but also on which crystal is used. The THz bandwidth for ZnTe crystals is always limited to a maximum of about 5 THz because of the optical phonon frequency for ZnTe at 5.31 THz. THz photons generated at that frequency will immediately be absorbed again, creating phonons.

For the experiments in this thesis two different crystals were used for the generation of THz light: ZnTe and N-benzyl-2-methyl-4-nitroaniline (BNA) [70, 71]. In the experiments relatively thick crystals were used (1-2 mm), which has two consequences. The generated THz power is relatively large, due to a longer interaction length between the light and the material. A disadvantage of using thick crystals is that the bandwidth is limited. The bandwidth for the THz pulses used in the experiments in this thesis is in most cases limited from 0.3 THz up to 2-2.5 THz. For higher frequencies the phase mismatch is larger and this results together with the long interaction length that the optical 800 nm and the generated THz beam run out of phase in the crystal.

Only for the experiments described in chapter 6, ZnTe is used as generation crystal for THz radiation. In the other experiments BNA is used. BNA is more efficient in the generation of THz radiation than ZnTe [70, 71]. The disadvantage of BNA as for all organic crystals is that the damage threshold in lower than for semiconductor materials like ZnTe. In practise, pulses of maximum 150 μJ were used for the generation of THz light in BNA. Although lower energy was used than for the generation in ZnTe, still higher THz power could be generated. The bandwidth that can be generated with BNA, up to 4 THz [71], is also larger than for ZnTe. However the bandwidth of the experiments described here was more limited by the detection crystal (section 2.3), which was ZnTe in all experiments.

2.3 Detection of terahertz radiation

The energy of a THz photon is much too low to measure the light intensity with a conventual photodetector. Although a similar method can still be applied. THz light is absorbed in a material, which in this case does not create carriers like in a photodetector but produce heat. The rise in temperature can be measured and related to the intensity of the THz beam. Examples of such detectors are Bolometers [72], which are semiconductor diodes where the change in temperature changes the resistivity and Golay Cells [73], where an increase of the temperature causes expansion. Other detection methods include Schottky diode mixers [74] and pyroelectric detectors [75]. One very common used technique in THz time-domain spectrometers is using photoconductive antennas [10, 76, 77]. Where for the generation of THz radiation a bias is applied between the electrodes, for detection the bias is supplied by the THz electric field. Carriers are again generated by an ultrafast laser pulse. If no THz light is present, there is no bias and no current will be measured. If a THz pulse is present, the carriers will be accelerated and a current is measured. The measured current is linearly proportional to the electric field strength of the THz pulse and to the conductivity of the material $J(\omega) = \sigma(\omega)E(\omega)$. Important properties for the material of the THz detector is a high mobility, which will give larger signals and a short carrier lifetime, which results in a larger detection bandwidth.

The other commonly used method is free-space electro-optic sampling [78–81]. This method will be described in more detail, because this method is used in the experiments. When a voltage is applied on a electrooptic crystal, the refractive index of the material will change. This is also reffered as the linear electrooptic effect or Pockels effect. In freespace electrooptic sampling the voltage is supplied by the THz electric field. Because the THz pulse has a certain polarization, the refractive index changes only in one direction, inducing an extra birefringence in the material. Electrooptic crystal are already birefringence without applied electric field. This extra induced birefringence can be measured by observing a change in the polarization of a near-infrared probe. An initially linearly polarized light pulse traveling in a birefringence crystal will observe different refractive indices for the ordinary and extraordinary axes. This results in a phase shift between the two polarizations. This phase shift is given by

$$\Delta\phi = \Delta n \frac{\omega}{c} L, \tag{2.8}$$

where Δn is the difference in refractive index between the ordinary and extraordinary axes and L is the length of the crystal. Note that Eq. 2.8 is only valid if the linearly polarized probe observes the same difference in refractive index between the ordinary and extraordinary axes throughout the whole crystal. Since the change in refractive index is supplied by the THz

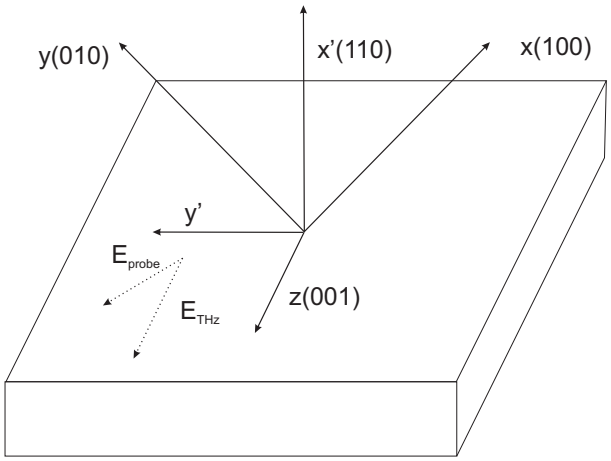

Figure 2.4: Orientation of the axes of the original (x,y,z) and deformed refractive index ellipsoid in a <110> oriented ZnTe crystal. The THz electric field E_{THz} is applied along the z axis. E_{probe} shows the polarization of the near-infrared probe.

pulse traveling through the crystal, phasematching between the THz pulse and the near-infrared probe pulse is required. The change in refractive index induced by the THz electric field is approximately linearly proportionally to the electric field strength. Only for very large electric field strengths it starts to differ from linearly dependence. The THz pulses generated in our experiments are well below that regime. In all the experiments described here, ZnTe is used as a detection crystal, because of the large electrooptic coefficient of 4 pm/V and good phasematching between the THz frequencies up to 2.5 THz and the 800 nm laser beam used to probe the electrooptic effect.

The efficiency of electrooptic sampling depends on the angle between the polarization of the THz beam and the near-infrared probe. For calculating the effect of the electric field applied on the polarization of a near-infrared probe traveling through the the nonlinear crystal, the refractive index ellipsoid is used as in Ref. [82]. The refractive index ellipsoid describes the refractive index in a crystal, experienced by a laser beam with a certain polarization traveling in a certain direction through the crystal. We describe here the situation for a <110> oriented ZnTe crystal. This means that the THz bean and the near-infrared probe travel in the (110) direction of the crystal. The z-axis of the coordinate system is along the (100) axis of the crystal, see Fig. 2.4. When no electric field is applied the refractive index ellipsoid in given by

$$(\frac{1}{n_x^2})x^2 + (\frac{1}{n_y^2})y^2 + (\frac{1}{n_z^2})z^2 = 1, \tag{2.9}$$

where x, y, and z are the principal dielectric axes and n_i, is the refractive index in the direction i. When an electric field is applied, this refractive index ellipsoid will be deformed. It will introduce the cross terms $(1/n^2)_4 yz$, $(1/n^2)_5 xz$ and $(1/n^2)_6 xy$. The first three terms $(1/n^2)_{1,2,3}$ are defined as $(1/n^2)_{x,y,z}$ respectively.

When a small electric field is applied, which is the case for the experiments described in this thesis, the refractive index in the crystal changes linearly by

$$\Delta(\frac{1}{n^2})_i = \sum_{j=1}^{3} r_{ij} E_j, \tag{2.10}$$

where r_{ij} is the electrooptic tensor which contains 18 terms, E_j is the electric field component in the j direction. The electrooptic tensor depends on internal symmetry of the crystal and for cubic crystals like ZnTe only three components of the electroopic tensor are nonzero: $r_{41} = r_{52} = r_{63} = 4$ pm/V. Because all three nonzero terms are equal, r_{41} is usually defined as the electrooptic coefficient. If we apply Eq. 2.10 and take for simplicity $n_x = n_y = n_z = n_0$ then the refractive index ellipsoid with applied electric field is given by

$$(\frac{1}{n_0^2})x^2 + (\frac{1}{n_0^2})y^2 + (\frac{1}{n_0^2})z^2 + 2E_x r_{41} yz + 2E_y r_{41} xz + 2E_z r_{41} xy = 1 \tag{2.11}$$

To calculate the change in the polarization of a probe beam traveling through the crystal, the new refractive index ellipsoid (Eq. 2.11) should be projected on the refractive index ellipsoid without an applied electric field (Eq. 2.9) so that the mixed terms are removed and instead the original refractive index components $n_{x,y,z}$ will depend on the applied electric field E_{THz}, the original refractive index n_0 and the electooptic coefficient r_{41}. The first transformation that is needed is a rotation of 45° around the z axes, so that the new x' axis is aligned in the (110) direction (Fig. 2.4). The new refractive index ellipsoid reads

$$x'^2(\frac{1}{n_0^2} + E_z r_{41}) + y'^2(\frac{1}{n_0^2} - E_z r_{41}) + \frac{z'^2}{n_0^2} + 2\sqrt{2} E_x r_{41} y' z' = 1. \tag{2.12}$$

When the THz beam propagating in the x' direction and is polarized along the z' direction so $E_z = E_{THz}$ (Fig. 2.4), the last term on the left hand side of Eq. 2.12 is zero and no second transformation is needed and the new refractive indices reads

$$n'_x = n_0,$$

$$\begin{aligned} n'_y &= n_0 + \frac{n_0^3}{2} E_{THz} r_{41}, \\ n'_z &= n_0 - \frac{n_0^3}{2} E_{THz} r_{41}. \end{aligned} \tag{2.13}$$

Eq. 2.13 shows that that due to the THz pulse, the refractive indices in the y' and z' direction are different, which means that the near-infrared probe traveling in the x' direction will experience birefringence and will get elliptically polarized. In this particular situation, the largest phase retardation and hence the largest signal is obtained when the probe beam is polarized at 45° from the z' axis and thus also at 45° from the THz polarization. However, the strongest signals are obtained at an angle of 0° or 90° [82]. In the above situation these angles between the THz and near-infrared probe polarization would not result in any signal. To obtain the largest signal the orientation of the crystal should be changed. So the THz electric field is no longer in the (001) direction of the ZnTe crystal.

After the detection crystal, a quarter waveplate is placed to change the polarization of the infrared probe into circular, see Figs. 2.5, 2.6. A wollaston prism or a polarizer beam splitter splits the beam depending on the polarization. If the light is circular polarized, the intensity after the wollaston prism is equally divided between the two beams. The intensity difference between the two beams is measured by balanced photodiodes. If a THz pulse is present in the crystal, the induced phase difference between the ordinary and extraordinary axes results in slightly elliptical polarized light after the quarter waveplate. Elliptically polarized light will be split unequally by the wollaston prism and hence a difference in intensity between the two beams is measured by the balanced photodetectors. The measured voltage difference between the photodiodes is linearly proportional to the electric field strength, providing that the electric field strength is in the linear electrooptic regime. The electric field strength of the THz pulse can be calculated according to

$$E_{THz} = \frac{2\Delta V}{V_{max}} \frac{c}{\omega n_0^3 r_{41} d}, \tag{2.14}$$

where ΔV is the voltage difference, V_{max} is the absolute voltage of each of the photodiode, which is proportional to the current generated by the probe beam, d the thickness of the electrooptic crystal.

2.4 Experimental setups

The laser output is first equally split, where half the intensity is used as input for the OPA. The other half is sent to the THz setup. If more power is needed this step can be skipped enabling to use all the power for the THz setup. Before entering the setup, at two positions a small portion of the light is split off with beam samplers to quadruple detectors for alignment purposes. By

aligning the beam onto the centers of the detectors, changes in the direction of the laser beam on day to day bases can easily be compensated. At the setup the beam is two times split to obtain three beams. First to split off the pump, used to excite carriers in the studied sample. The beam splitter that is used splits the beam unequally into approximately 70%/30%, where 70% is used as pump to excite carriers in the sample. A larger intensity in the pump is needed in case this beam has to be frequency doubled in a nonlinear crystal, see chapter 6. The other part, which is used for generating and detecting the THz beam is sent through an optical delayline. A retroreflector is used to reflect the beam without changing the alignment when the position is changed. By changing the position of the delayline the path length of the beams that are used for both generation and detection is changed equally. In this way it is possible to change the relative time between exciting carriers in the sample and the THz pulse traveling through the sample. The delayline can make steps of 1 μm, which means a change in pathlength of 2 μm, which correspond to 6.7 fs. Because the time resolution of the setup will mainly be determined by the pulse duration of the laser pulses, making longer steps is more efficient.

A small portion of this beam is split off with a beam sampler for probing the changes in refractive index of the detection crystal, induced by the THz electric field. The main part is used for generating the THz beam. This beam is again sent through an optical delay line with a retroreflector. By changing the optical path length of the generation beam relative to the detection beam, the moment when the THz pulse travels through the detection crystal relative to the detection beam can be changed. Hereby changing which part of the THz pulse is measured. All the three beams have a half-wave plate and polarizer combination for changing the intensity without changing the polarization of the beam. The detection of terahertz radiation depends strongly on the angle between the polarization of the THz beam and that of the near-infrared probe [82]. In these experiments the same polarization for the THz beam and the near-infrared probe is used.

Two different configurations of the actual THz spectrometer were used. The first one is shown in Fig. 2.5. This setup is used in the experiments described in chapters 5 and 6. In the generation beam path two lenses are used to decrease the spot size by a factor of 2. This is needed to get the spot size smaller than the crystal. A combination of a positive and a negative lens is used to avoid focussing of the beam. The high intensity of the laser beam can lead to nonlinear effects in air if the beam is focussed too tide. After the generation crystal, off-axis paraboloidal mirrors are used to change the beam size of the THz beam. The first mirror expands the THz beam enabling to focus tighter. The second mirror collimates the beam and the third mirror focusses the THz beam onto the sample. A forth and fifth mirror are used to collimate and focus again onto the detection crystal. The near-infrared probe used to detect the THz light is first reduced in size by two lenses and

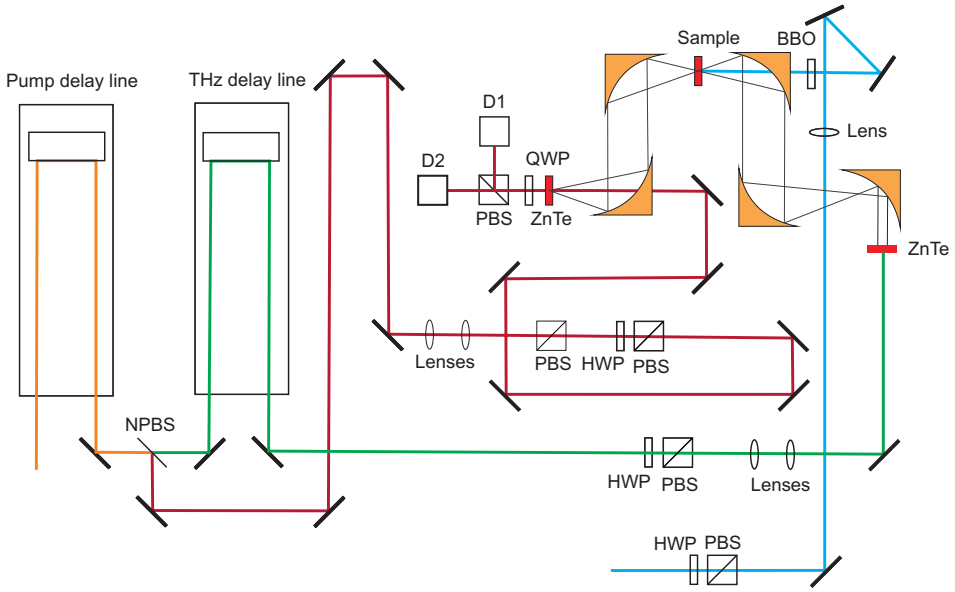

Figure 2.5: Schematic of the experimental setup used for the experiments described in chapters 5 and 6. The blue line is the pump beam, the green line is the THz generation beam and the red line is the THz detection beam. Black lines show the travel path of the THz beam, with foci at the sample and at the detection crystal. NPBS: non-polarizer beam splitter, PBS: polarizer beam splitter, HWP: half-wave plate, QWP: quarter-wave plate, D1 and D2: photodetectors.

finally focussed on the detection crystal. A small hole is drilled into the fifth paraboloidal mirror to let the near-infrared probe through. The changes in polarization of the transmitted near-infrared probe are then measured. The pump beam is sent to the sample through a hole in the third paraboloidal mirror. One lens is used to focus the beam, enabling it to travel through the small hole. After the focus the beam expands so that a larger spot size is obtained at the sample position. However, due to the short distance between the mirror and the sample position a maximum beam size of $\sim$ 2-3 times the THz beam size can be obtained, which means that a pinhole at the sample position is required to ensure uniform carrier excitation over the THz spot size. In this configuration the THz beam is focussed very tide on the sample position. The relative large wavelength of THz beam causes that the focus is still several hundreds of μm, depending on the wavelength. After the generation crystal and after the sample a thin black poly-ethylene foil is used to block the optical beams. Poly-ethylene is transparent at THz frequencies.

The second setup is shown in Fig. 2.6. The generation spot size is again reduced by a factor of two because of the limited size of the generation crys-

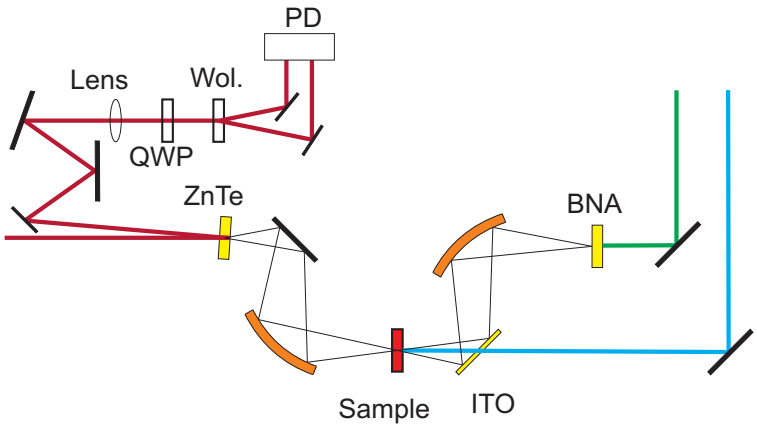

Figure 2.6: Schematic of the experimental setup used for the experiments described in chapter 7. The blue line is the pump beam, the green line is the THz generation beam and the red line is the THz detection beam. Black lines show the travel path of the THz beam. QWP: quarter-wave plate, Wol.: wollaston prism, ITO: indium-tin oxide coated quartz, PD: photodetectors.

tal. After the generation crystal an ellipsoidal mirror focusses the THz beam. The second mirror is a plane mirror made of indium-tin oxide coated quartz (ITO). ITO is a good reflector for THz light and is relatively transparent for visible and near-infrared light. In our case the transmissivity for the 800 nm pump was 61 %. A second ellipsoidal mirror and a plane silver mirror are used to focus onto the detection crystal. The benefit of this configuration is that the pump is sent through the ITO mirror instead of through a hole, which enables to obtain a larger pump spot size at the sample. For obtaining the larger spot size, a combination of a positive and a negative lens is used. By changing the position of the lenses so that the focal points of the lenses do not overlap, the beam will not be collimated but can be used to expand the beam. The reason for using two lenses where the spot size first gets smaller is that it enables to generate the second harmonic of the 800 nm beam more efficiently. The process of second harmonic generation depends quadratically on the intensity and is therefore more efficient if the spot size is reduced. The beam size of the detecting beam is reduced by a factor of 20/3 and collimated. In this configuration the back reflection from the rear side of the detection crystal is used as a probe [83]. The reflection from the front size of the crystal is blocked. This back-reflection configuration requires that a relative thick detection crystal is used to separate the front and rear reflection. This off-course limits the detected bandwidth.

The spot size of the pump is measured by sliding a knife-edge through the beam and measuring the power. A result of this measurement can be seen in Fig. 2.7(a). The actual beam profile is the derivative of this measurements

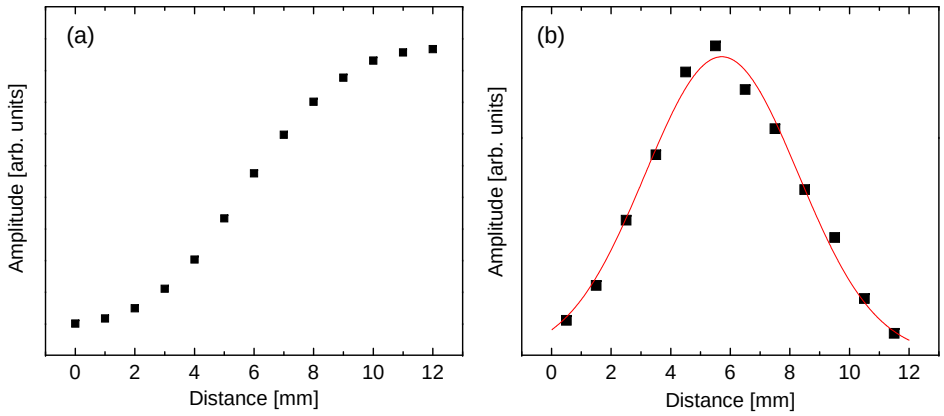

Figure 2.7: (a) Measured power of the laser beam while a knife edge is slight through the beam at the sample position. (b) Derivative of the data shown in (a) (dots), gaussian fit (red line, showing a beam waist of 2.6 mm.

which is shown in Fig. 2.7(b). From the fit with a gaussian pulse shape (red line) a beam waist of 2.6 mm is obtained. From the waist of the beam and the measured power the fluence could be calculated according to

$$F = \frac{2E_{pp}}{\pi w^2}, \tag{2.15}$$

where E_{pp} is the energy per pulse and w is the waist of the beam. The fluence, which is the intensity per pulse is an important parameter that can be changed to study the effect of the carrier concentration on the carrier dynamics in semiconductor materials.

To minimize the effect of fluctuations in the laser beam and environment, a lock-in amplifier is used. An optical chopper is placed in the setup to change the repetition rates of one or two of the beams. To measure a THz pulse, the chopper is placed in the generation beam. The chopper blade is designed that 1 out of 2 pulses is blocked, thereby changing the repetition rate to 500 Hz. If the lock-in amplifier is set to 1 kHz, it measures changes that occur at 1 kHz. Because the detection beam has a repetition rate of 1 kHz, the absolute intensity difference between the two detectors is measured. If the THz generation is blocked this should be 0. By rotating the quarter wave plate, see Fig. 2.6, the intensity difference measured by the balanced photodetectors is set as close to zero as possible. If the lock-in amplifier is set to 500 Hz, the changes due to the generation of the THz beam are measured. Intensity fluctuation of the laser beam which occur at 1 kHz are filtered out.

An example of a THz pulse measured in the setup described above is shown in Fig. 2.8(a). This THz pulse is generated in a BNA crystal, which was excited with 800 nm pulses with a pulse energy of 150 μJ. Since optical

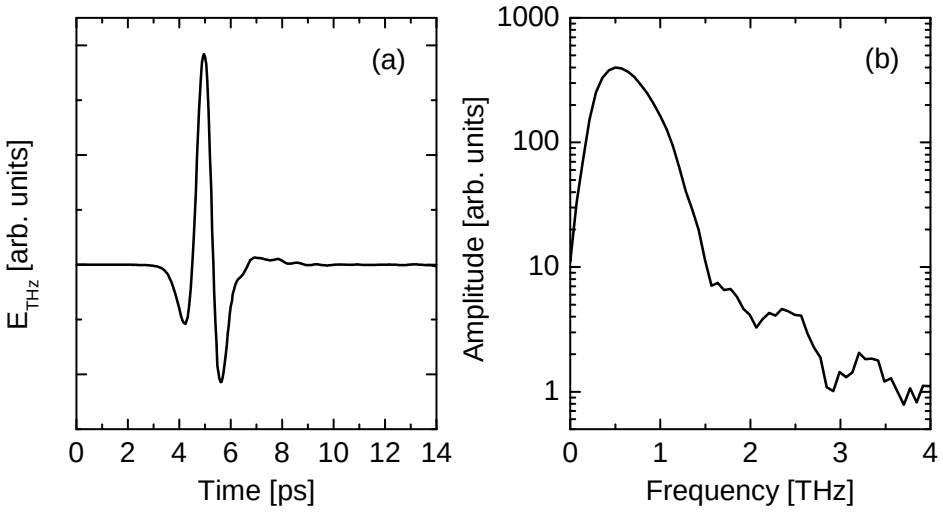

Figure 2.8: (a) Typical THz pulse measured with purging the setup with dry nitrogen. (b) Amplitude spectrum of the THz pulse shown in (a).

rectification is a second order nonlinear process, the THz power will depend quadratically on the power of the 800 nm beam. The value of 150 μJ is chosen because using even higher pulse energies has the risk of damaging the crystal. For measuring a THz pulse, the second delay line that changes only the path length of the generation beam is changed with steps of 12 μm, which correspond to 40 fs. Since the delay line is in the generation arm the retroreflector is moved toward the beams, thereby shorting the optical path length. This means that the THz pulses are generated earlier, which is the same as detecting later. As can be seen the ultrashort THz pulse is single cycle. One of the problems for free propagating THz waves is its absorption in water vapor. The THz photons excite the vibrational and rotational levels of the water molecules. At later times the molecules decay back to the ground state by re-emitting a THz photon, creating wiggles after the main pulse. Only certain specific frequencies are absorbed and re-emitted by the water. To decrease the effect of water vapor, the setup is purged with dry nitrogen. The absorption of THz light is decreased but not completely removed. This is because with our method, purging with dry nitrogen using a box with holes for the laser beams, it is not possible to completely remove the water vapor. There is also a limit in how hard the setup can be purged, because if the flow is too strong it will introduce noise. A single cycle THz wave translate in the frequency domain to a broadband pulse. To obtain the spectrum the THz pulse (Fig. 2.8(a)) is Fourier transformed (Fig. 2.8(b)). The THz wave span frequencies from about 0.3 until 2.5 THz. The main limiting factor in this experiment is the detector crystal, where there is a large phase mismatch for frequencies above 2.5 THz.

Chapter 3

Time-domain terahertz spectroscopy

If a sample is placed in the setup, the transmission of the THz pulse through the sample can be measured. Typically, in time-domain terahertz spectroscopy two measurements are performed, one with sample and one without sample. The advantage of THz spectroscopy is that both the amplitude and the phase information is obtained, from which different properties like thickness, refractive index and absorption of the sample can be deduced [10, 84, 85]. Furthermore, many resonances lay in the THz regime. Time-domain terahertz spectroscopy has been used to measure vibrational and rotational excitations in powders [12, 13], liquids [22, 24, 86], gasses [21, 27] and energy gaps in superconductors [87, 88]. In time-domain terahertz spectroscopy the sample is in equilibrium so there is no optical excitation by a pump beam. To understand how material properties can be obtained from the measured THz pulses, first the interaction between light and matter will be explained. Second, the transmission and reflection of an light beam through an interface are calculated to obtain the Fresnel equations. Then the transmission through a slab, which is measured in a time-domain THz spectroscopy experiment, is calculated. Finally an example of a time-domain terahertz spectroscopy experiment is shown. As example a slab of bulk GaAs is chosen.

3.1 Light-matter interaction

Light, which is an electromagnetic wave constitutes of an electric field $\vec{E}$ and a magnetic field $\vec{B}$. An electromagnetic wave in vacuum can be described with those two vectors. For the interaction with matter some additional vectors has to be introduced: $\vec{J}$ is the electric current density, $\vec{D}$ is the electric displacement field and $\vec{H}$ is the magnetizing field. The relations between these vectors are described by the Maxwell equations:

$$\nabla \times \overrightarrow{E} = -\frac{\partial \overrightarrow{B}}{\partial t}, \tag{3.1}$$

$$\nabla \times \overrightarrow{H} = \frac{\partial \overrightarrow{D}}{\partial t} + \overrightarrow{J}, \tag{3.2}$$

$$\nabla \cdot \overrightarrow{D} = \rho, \tag{3.3}$$

$$\nabla \cdot \overrightarrow{B} = 0. \tag{3.4}$$

ρ is here the electric charge density. For many materials in equilibrium there are no or a negligible amount of free charges. So Eq. 3.3 reduces to $\nabla \cdot \overrightarrow{D} = 0$. Eq. 3.4 states that there exist no free magnetic poles. Besides these four Maxwell equations, equations that describe the behavior of matter under influence of an electromagnetic field are needed. These equations are Ohms law and the equations for the electric displacement and magnetic induction. These equations can be rather complex. However for isotropic materials in equilibrium, these equations reduces to a much simpler form:

$$\overrightarrow{J} = \sigma \overrightarrow{E}, \tag{3.5}$$

$$\overrightarrow{D} = \varepsilon \overrightarrow{E}, \tag{3.6}$$

$$\overrightarrow{B} = \mu \overrightarrow{H}, \tag{3.7}$$

where σ is the conductivity, ε is the permittivity and μ is the permeability. By substituting the material equations 3.5-3.7 into the maxwell equations 3.1-3.4, the Maxwell equations can be reduced, so that it only contains only, $\overrightarrow{E}$ and $\overrightarrow{H}$, fields.

$$\nabla \times \overrightarrow{E} = -\mu \frac{\partial \overrightarrow{H}}{\partial t}, \tag{3.8}$$

$$\nabla \times \overrightarrow{H} = \varepsilon \frac{\partial \overrightarrow{E}}{\partial t} + \sigma \overrightarrow{E}, \tag{3.9}$$

$$\nabla \cdot \overrightarrow{E} = 0, \tag{3.10}$$

$$\nabla \cdot \overrightarrow{H} = 0. \tag{3.11}$$

If the curl of Eq. 3.8 and Eq. 3.9 is taken, these equations read respectively

$$\nabla \times \nabla \times \overrightarrow{E} = -\mu \frac{\partial}{\partial t} \nabla \times \overrightarrow{H}, \tag{3.12}$$

$$\nabla \times \nabla \times \overrightarrow{H} = \varepsilon \frac{\partial}{\partial t} \nabla \times \overrightarrow{E} + \sigma \nabla \times \overrightarrow{E}. \tag{3.13}$$

If for the left hand side of these equation the vector identity: $\nabla \times \nabla \times \overrightarrow{A} = \nabla \cdot (\nabla \cdot \overrightarrow{A}) - \nabla^2 \overrightarrow{A}$ together with Eqs. 3.10 and 3.11 are used and Eq. 3.8 and Eq. 3.9 are filled into the right hand side of Eq. 3.13 and Eq. 3.12 respectively. These equations read then:

$$\nabla^2 \overrightarrow{E} = \varepsilon\mu \frac{\partial^2 \overrightarrow{E}}{\partial t^2} + \mu\sigma \frac{\partial \overrightarrow{E}}{\partial t} \tag{3.14}$$

$$\nabla^2 \overrightarrow{H} = \varepsilon\mu \frac{\partial^2 \overrightarrow{H}}{\partial t^2} + \mu\sigma \frac{\partial \overrightarrow{H}}{\partial t} \tag{3.15}$$

These equation are called the wave-equations, because a solution of these differential equations are waves. If a wave in the form of

$$\overrightarrow{E} = E_0 e^{i(kx-\omega t)} \tag{3.16}$$

is tried as a solution for the wave equation 3.14, we obtain:

$$-k^2 E_0 = \varepsilon\mu(-\omega^2)E_0 - i\omega\mu\sigma E_0, \tag{3.17}$$

which reduces to the dispersion relation

$$k^2 = \omega^2 \varepsilon\mu + i\omega\mu\sigma. \tag{3.18}$$

The dispersion relation describes the relation between the wavevector k and the angular frequency ω of the electromagnetic wave in the material. For non-magnetic media $\mu = \mu_0$. If the relation $\varepsilon_0\mu_0 = 1/c^2$ is used, where c is the speed of light in vacuum, Eq. 3.18 can be written in the form

$$k^2 \frac{c^2}{\widetilde{n}^2} = \omega^2, \tag{3.19}$$

where $\widetilde{n}$ is the complex index of refraction. The complex index of refraction reads then

$$\widetilde{n} = n + i\kappa = \sqrt{\frac{\varepsilon}{\varepsilon_0} + i\frac{\mu_0\sigma}{\omega}c^2}, \tag{3.20}$$

where n is the real part of the refractive index and κ is the imaginary part of the refractive index or extinction coefficient. For $\overrightarrow{H}$ a similar calculation can be performed, which will lead to the same results. In an electromagnetic wave the magnetizing field is perpendicular to the electric field and is in non-magnetic media given by

$$\overrightarrow{H} = \sqrt{\varepsilon}\,\overrightarrow{s} \times \overrightarrow{E}, \tag{3.21}$$

where $\overrightarrow{s}$ is a unit vector.

As can be seen from Eq. 3.20 the complex material properties $\tilde{n}$, $\tilde{\varepsilon}$ and $\tilde{\sigma}$ are related, so it does not matter which one is used for describing the

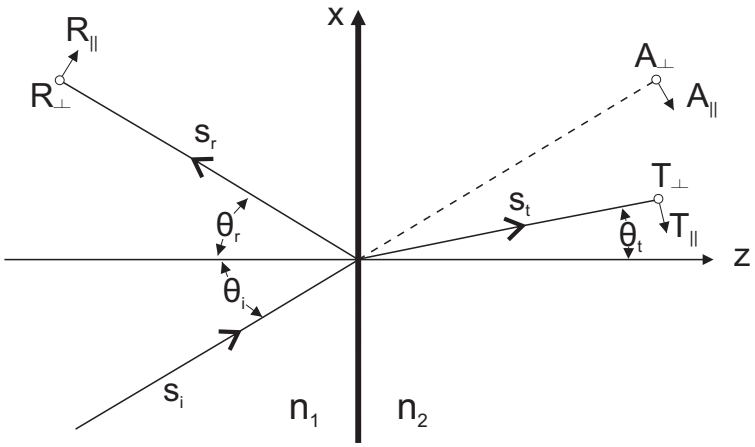

Figure 3.1: Reflection and refraction of a light wave at an interface.

material. The goal of time-domain and time-resolved THz spectroscopy is to measure the frequency dependent complex material properties. In this thesis the materials are described by the complex conductivity $\tilde{\sigma}(\omega)$.

3.2 Fresnel equations

When a light wave enters an interface between two homogeneous media with different refractive indices, the beam is split where part of the beam is refracted into the new material and part is reflected from the interface, see Fig. 3.1. The directions of the beams is described by the unit vectors $\overrightarrow{s}_{i,r,t}$, where the subscripts stands for incident, reflected and transmitted wave respectively. The time behavior of a point with a position vector $\overrightarrow{r}$ relative to an other point with time behavior F(t) is given by F$[t - (\overrightarrow{r} \cdot \overrightarrow{s})/v]$ [89]. At the interface between two homogeneous media the boundary condition states that the time behavior of the secondary wave is equal to the time behavior of the incident wave, so for $z = 0$:

$$t - \frac{\overrightarrow{r} \cdot \overrightarrow{s_i}}{v_1} = t - \frac{\overrightarrow{r} \cdot \overrightarrow{s_r}}{v_1} = t - \frac{\overrightarrow{r} \cdot \overrightarrow{s_t}}{v_2}. \tag{3.22}$$

At the boundary $z = 0$, $\overrightarrow{r}$ consist of two nonzero components: $r \equiv x, y, 0$. So Eq. 3.22 becomes

$$\frac{xs_{x,i} + ys_{y,i}}{v_1} = \frac{xs_{x,r} + ys_{y,r}}{v_1} = \frac{xs_{x,t} + ys_{y,t}}{v_2}. \tag{3.23}$$

We can further specify this equation by using $s_{x,(i,r,t)} = \sin\theta_{(i,r,t)}$, where $\theta_{(i,r,t)}$ are the angles between $\overrightarrow{s_{i,r,t}}$ and the z-axis (see Fig. 3.1) and $s_{y,(i,r,t)} = 0$. Substituting these expressions into Eq. 3.23 gives

$$\frac{\sin\theta_i}{v_1} = \frac{\sin\theta_r}{v_1} = \frac{\sin\theta_t}{v_2}. \tag{3.24}$$

This reveals the law of reflection $\theta_i = \theta_r$. If the law of refraction is written in terms of the refractive index $v_{1,2} = c/n_{1,2}$, Snell's law is obtained

$$\frac{\sin\theta_i}{\sin\theta_t} = \frac{n_2}{n_1} = n_{12}. \tag{3.25}$$

Now the amplitudes of the reflected and refractive waves will be calculated. Let A, R, T be the amplitude of the electric field of the incident, reflected and transmitted field respectively. The variable part of the wave is $\exp[-i\omega\tau_{i,r,t}]$, where $\tau_{i,r,t}$ is given by

$$\tau_{i,r,t} = t - \frac{\overrightarrow{r}\cdot\overrightarrow{s_{i,r,t}}}{v_{1,2}} = t - \frac{x\sin\theta_{i,r,t} + z\cos\theta_{i,r,t}}{v_{1,2}}, \tag{3.26}$$

where for the incident and reflected wave v_1 and for the transmitted wave v_2 should be used. The electric field vector is now resolved in a component parallel and perpendicular (denoted by the subscripts $\parallel$ and $\perp$) to the plane of incidence. The components of the incidents electric wave are then

$$E_{x,i} = -A_\parallel\cos\theta_i e^{-i\omega\tau_i}, E_{y,i} = A_\perp e^{-i\omega\tau_i}, E_{z,i} = A_\parallel\sin\theta_i e^{-i\omega\tau}. \tag{3.27}$$

The $\overrightarrow{H}$ field follows from Eq. 3.21.

$$H_{x,i} = -A_\perp\cos\theta_i\sqrt{\varepsilon_1}e^{-i\omega\tau_i}, H_{y,i} = -A_\parallel\sqrt{\varepsilon_1}e^{-i\omega\tau_i}, H_{z,i} = A_\perp\sin\theta_i\sqrt{\varepsilon_1}e^{-i\omega\tau}. \tag{3.28}$$

The expressions for the reflected and transmitted fields are similar, where only the subscripts has to be changed to r,1 and t,2 respectively. The boundary conditions at the interface state that the tangential components of $\overrightarrow{E}$ and $\overrightarrow{H}$ are continuous:

$$\begin{aligned} E_{x,i} + E_{x,r} &= E_{x,t}, \\ E_{y,i} + E_{y,r} &= E_{y,t}, \\ H_{x,i} + H_{x,r} &= H_{x,t}, \\ H_{y,i} + H_{y,r} &= H_{y,t}. \end{aligned} \tag{3.29}$$

Substituting Eq. 3.27, Eq. 3.28 and the expression for the y-component into Eq. 3.29, four relations between the electric field amplitudes are obtained

$$\cos\theta_i(A_\parallel - R_\parallel) = \cos\theta_t T_\parallel,$$

$$\begin{aligned} A_\perp + R_\perp &= T_\perp, \\ \sqrt{\varepsilon_1}\cos\theta_i(A_\perp - R_\perp) &= \sqrt{\varepsilon_2}\cos\theta_t T_\perp, \\ \sqrt{\varepsilon_1}(A_\parallel + R_\parallel) &= \sqrt{\varepsilon}T_\parallel. \end{aligned} \tag{3.30}$$

These equations can be solved for the reflected and transmitted wave, where the permittivity ε is changed to refractive index n: $\sqrt{\varepsilon} = n$.

$$R_\parallel = \frac{n_2\cos\theta_i - n_1\cos\theta_t}{n_2\cos\theta_i + n_1\cos\theta_t}A_\parallel, \tag{3.31}$$

$$R_\perp = \frac{n_1\cos\theta_i - n_2\cos\theta_t}{n_1\cos\theta_i + n_2\cos\theta_t}A_\perp, \tag{3.32}$$

$$T_\parallel = \frac{2n_1\cos\theta_i}{n_2\cos\theta_i + n_1\cos\theta_t}A_\parallel, \tag{3.33}$$

$$T_\perp = \frac{2n_1\cos\theta_i}{n_1\cos\theta_i + n_2\cos\theta_t}A_\perp. \tag{3.34}$$

The obtained equations are called the Fresnel equations and are used is any reflection or transmission experiment. In many experiments the incident wave will be at normal incidence. In that special case the Fresnel equations 3.31-3.34 reduce to

$$R_\parallel = \frac{n-1}{n+1}A_\parallel, \tag{3.35}$$

$$R_\perp = -\frac{n-1}{n+1}A_\perp, \tag{3.36}$$

$$T_\parallel = \frac{2}{n+1}A_\parallel, \tag{3.37}$$

$$T_\perp = \frac{2}{n+1}A_\perp, \tag{3.38}$$

where $n = n_2/n_1$

Real materials do not have just one interface, but in the simplest case of a slab at least two with a material with a certain refractive index in between. The propagation of a light wave in a material with refractive index $\tilde{n}$ is described by the propagation coefficient

$$P = \exp[i\frac{\omega}{c}\tilde{n}d], \tag{3.39}$$

where d is the propagation distance. If $\tilde{n}$ is split up in a real and imaginary part $\tilde{n} = n + i\kappa$, the real part describes a sinusoidal wave $\exp[i(\omega/c)d]$. For the imaginary part, Beers law is obtained, which describes the absorption in the material. Beers law is normally described in terms of intensity instead of electric field which means taking the square of Eq. 3.39.

$$I(d) = I_0 \exp[-\alpha d] \tag{3.40}$$

where I_0 is the intensity at $d = 0$ and the absorption coefficient α is given by

$$\alpha = \frac{2\omega\kappa}{c} \tag{3.41}$$

For calculating the transmission and reflection for layered structures, Fresnel equations for interfaces and propagation coefficients for propagation in the different layers should be combined. Here we will only consider the simplest case of a single layer containing a material with refractive index $\tilde{n_2} = \tilde{n}$ surrounded by a material with refractive index $\tilde{n_1}$. In many cases the surrounding material will be air, which means $\tilde{n_1} \approx 1$. We will also take the thickness d of the material thick enough that multiple reflections are well separated. In this case only the main pulse will be measured and the multiple reflection are not taking into account. Note that for the transmission, the polarization of the beam does not matter. The transmission coefficient of an electromagnetic wave through a thick slab at normal incidence is then given by

$$\tilde{T} = \frac{t_{12}P_2t_{21}}{P_1} = \frac{4\tilde{n}}{(1+\tilde{n})^2} \exp[i(\tilde{n}-1)\frac{\omega}{c}d] \tag{3.42}$$

where t_{ij} means the Fresnel coefficient (Eq. 3.37) for the transmission from material i to material j, P_i is the propagation coefficient (Eq. 3.39) of material i.

For this equation to be useful to describe an experiment it has to be split up into a real part and imaginary part or in amplitude and phase. We will choose the latter one. The amplitude and phase are then given by

$$|T(\omega)| = \frac{|E_s(\omega)|}{E_{ref}(\omega)|} = \frac{4\sqrt{n^2+\kappa^2}}{(n+1)^2+k^2} \exp[-\frac{\omega\kappa d}{c}], \tag{3.43}$$

$$\Phi(\omega) = \theta_s(\omega) - \theta_{ref}(\omega) = -(n-1)\frac{\omega d}{c} + \arctan[\frac{\kappa(n^2+\kappa^2-1)}{n(n+1)^2+\kappa^2(n+2)}], \tag{3.44}$$

where E_s and E_{ref} are the transmitted electric fields through the sample and a reference electric field without sample where the electromagnetic wave travels only in air, respectively. θ_s and θ_{ref} are the phases of the electric field of the transmitted wave through the sample and the reference wave, respectively.

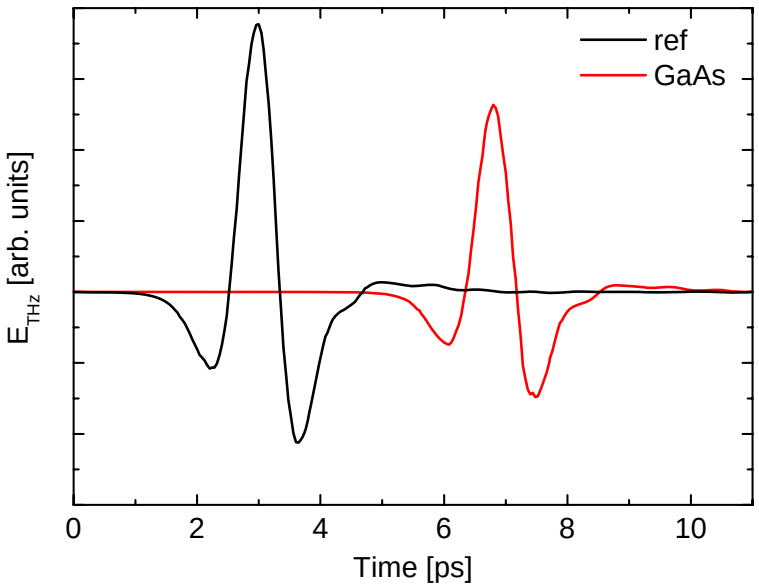

Figure 3.2: Electric field strength of the reference pulse traveling through air (black line) and the THz pulse traveling through a 0.44 mm thick GaAs sample (red line).

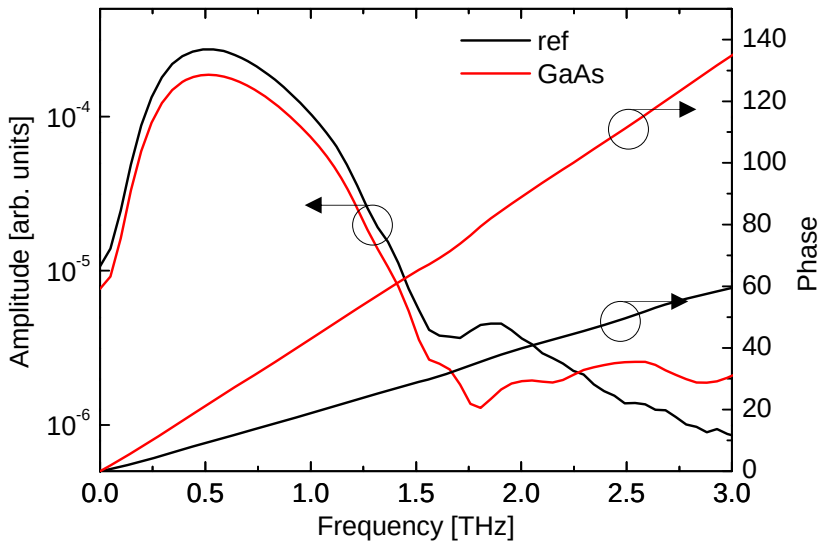

Figure 3.3: Amplitude and phase signal of the Fourier transforms of the THz transient shown in Fig. 3.2, where the black line is the reference and the red line the transmission through the GaAs sample.

3.3 Experiment

From Eqs. 3.43 and 3.44 it can be seen that for obtaining the refractive index of a material two measurements are needed. A measurement where the transmission through the investigated material is measured and a reference measurement without sample. The advantage of THz electromagnetic waves is that it is broadband, so information over a wide range of frequency is obtained. An other advantage is that the electric field is measured and not the intensity, which means that both the amplitude and phase are obtained. Both amplitude and phase information are needed to obtain the complex refractive index of the material. By measuring the intensity like is done for visible and near-infrared light, the phase information is lost. Although the phase can be calculated by using the Kramers-Kronig relation. However, this complicates the calculation and is not very accurate for small bandwidths.

As example of showing the method of time-domain terahertz spectroscopy, the transmission of a THz transient through a 0.44 ± 0.01 mm thick piece of GaAs is measured. The sample (red line) and reference (black line) signals are shown in Fig. 3.2. The higher refractive of GaAs causes the 3.8 ps delay of the THz pulse. From this delay an estimate of the refractive index can be obtained by $n = c\Delta t/d + 1$. For a thickness d of 0.44 mm this results in a index of refraction $n = 3.59$. To obtain a more accurate results Fourier analysis is applied. The frequency resolved amplitude and phase of the Fourier transforms for both signals are shown in Fig. 3.3. To obtain the refractive index Eqs. 3.43 and 3.44 should be inverted. This is rather complex, however if the absorption is weak which is the case for unexcited GaAs, the exponential decay in Eq. 3.43 and the arctan term in Eq. 3.44 can be neglected. This enables for decoupling the real and imaginary part of the refractive index.

$$n = -\frac{\Phi c}{\omega d} + 1, \tag{3.45}$$

$$|T(\omega)| = \frac{4\sqrt{n^2+\kappa^2}}{(n+1)^2+k^2} \tag{3.46}$$

Eq. 3.45 can be used to obtain the real part of the refractive index and this can be put into Eq. 3.46 to obtain the extinction coefficient. The extracted index of refraction for the 0.44 thick GaAs substrate is shown in Fig. 3.4. An average index of refraction over the bandwidth of the measured THz pulses of 3.61 is extracted. This shows that the time difference between the pulses is already a good estimate to obtain the index of refraction of a non-absorbing sample. The obtained average value of 3.61 is slightly higher then the average $n = 3.60$, measured by Grischkowsky et al. [10]. This is probably caused by the uncertainty in measuring the thickness of the sample. The extinction coefficient is negligible and therefore not shown here. The

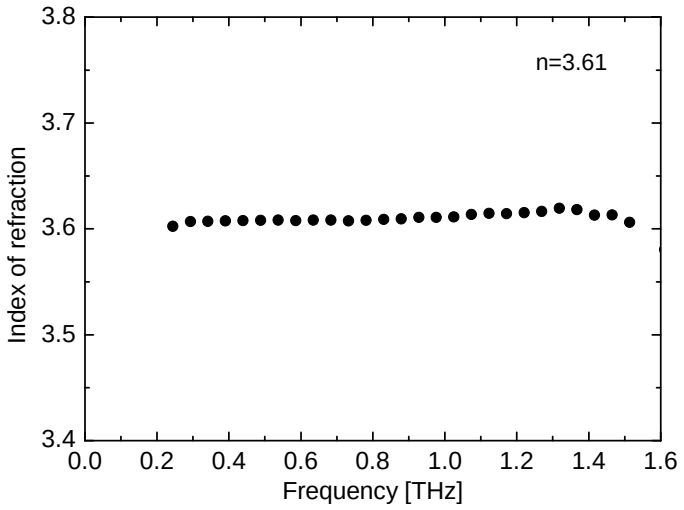

Figure 3.4: Index of refraction for a 0.44 mm thick GaAs substrate.

decrease of the electric field strength of the THz pulse that traveled through the GaAs substrate is thus only caused by the Fresnel reflections at the surfaces.

Chapter 4

Time-resolved terahertz spectroscopy

While in time-domain terahertz spectroscopy the static properties of a material are measured, in this chapter we describe time-resolved THz spectroscopy, which can be used to study the dynamical properties of a material. Typically, the transmission of a THz pulse is measured through an optically excited sample. Excited carriers, i.e. electrons in the conduction band and holes in the valence band of a bulk semiconductor are "free". This means that these carriers will be accelerated if an electric field is applied. The electric field that accelerates the carriers is supplied by the THz pulse. Energy conservation requires that the acceleration of carriers by the THz electric field causes a decrease of the THz electric field strength. Or in other words, free carriers will absorb THz radiation. Thus THz waves can probe the dynamics of free carriers in semiconductors [14, 90]. How strong the absorption is, depends not only on the carrier density n, but also on the mobility μ of the carriers. The change in THz transmission due to the optical excitation of charge carriers is a measure for the conductivity $\sigma = en\mu$ of the sample, where e is here the elementary charge. If one of the material properties, e.g. the conductivity of a sample is known then other properties like the refractive index or dielectric function can be calculated, see Eq. 3.20.

In this chapter we will derive the equations that relates the transmission of a THz pulse through an optically excited sample to the material properties in a similar way as shown in chapter 3. We distinguish between two methods, 2D- and 1D-spectroscopy, referring to the number of delay lines that are scanned during the experiment. Finally, both methods will be illustrated with an example, where again bulk GaAs is used.

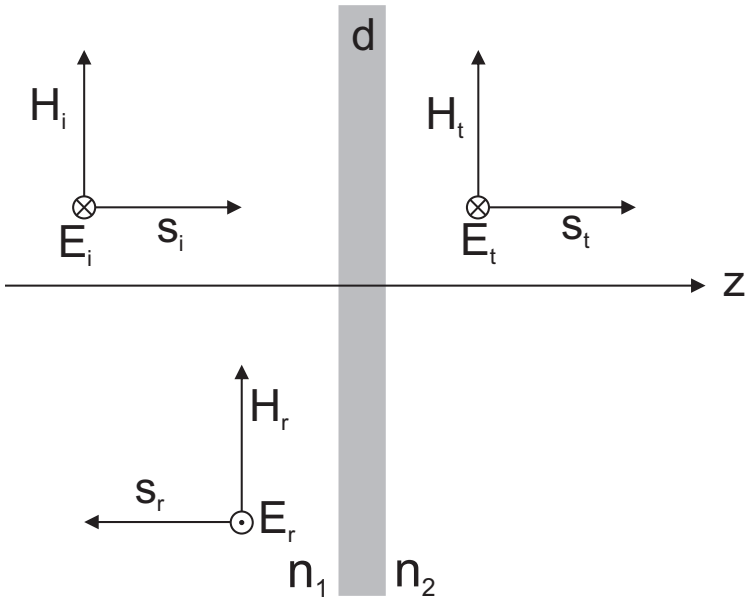

Figure 4.1: Transmission and reflection of an electromagnetic wave at a conducting layer with thickness d on an insulating substrate.

4.1 2D-spectroscopy

In 2D-spectroscopy both delay lines (Fig. 2.5) are used, which means that two time delays are involved. The first is the time delay between the THz pulse and the near-infrared probe used to measure the THz pulse, as described in Ch. 3. The second is the time delay between the THz pulse and the optical pump. So the transmission of a THz pulse through a photoexcited sample can be measured for different times after the optical excitation and in this way the behavior of the photoexcited carriers can be studied.

If an optical pulse is absorbed by a material, the intensity of the pulse will follow Beers law Eq. 3.40. Because the pulse gets weaker when it travels through an absorbing material, the excited carrier density will be the highest at the surface and decays exponentially further into the material. This makes the problem rather complex. However, if the penetration depth of the material is small (compare to the wavelength of the THz beam), it appears that using a thin homogeneous film of conductivity σ with a thickness d, where as d the penetration depth is taken, is a good approximation. By using this approximation, it is possible to extract material properties from the THz measurements [91].

In a similar way as in section 3.2, we will calculate the transmission of a THz pulse through a thin conductive layer on a nonconductive substrate with refractive index $n_2 = n$ (Fig. 4.1). Furthermore we will show how to obtain the complex conductivity $\tilde{\sigma}$ from the measured THz transmission.

Identical boundary equations as used to derive the Fresnel equations (Eq. 3.29) are applied, but now with a conductive layer in between. The boundary equations for the magnetic and electric fields at normal incidence reads then

$$H_i - H_r = H_t + \int_0^\infty \overrightarrow{J}\,\partial z = H_t + \overrightarrow{J}\,d, \tag{4.1}$$

$$E_i + E_r = E_t. \tag{4.2}$$

To obtain an expression for the electric field transmission E_t, the admittance is used, which is defined as $Y = H/E$. The admittance in the first material, which is air, is then $Y_1 = \frac{H_i+H_r}{E_i+E_r}$ and the admittance in the substrate is $Y_2 = \frac{H_t}{E_t}$. By combining Eq. 4.1 and Eq. 4.2 and solving for E_t, the electric field transmission is given by

$$E_t = \frac{1}{Y_1 + Y_2}(2Y_1 E_i - Jd). \tag{4.3}$$

Using Eq. 3.5, the transmission coefficient $\tilde{t}(\omega) = E_t/E_i$ reads

$$\tilde{t}(\omega) = \frac{2Y_1}{Y_1 + Y_2 + \tilde{\sigma}(\omega)d} \tag{4.4}$$

To describe the transmission through a thin conducting film in terms of the substrate material properties only, an other definition of the admittance can be used $Y_a = n_a/Z_0$, where n_a is the refractive index and $Z_0 = 377\Omega$ is the impedance of free space. This equation, also known as the Tinkham equation [92], reads

$$\tilde{t}(\omega) = \frac{2}{n + 1 + Z_0 d\tilde{\sigma}(\omega)}. \tag{4.5}$$

This equations is valid providing that the thickness is small compare to the wavelength $d \ll \lambda$. The wavelength of a THz pulse in air is relatively large (0.1-1 mm), so only if the refractive index or conductivity is very large, the wavelength in the material will be comparable with typical values of the thicknesses of the conducting layer. For the experiments described in this thesis this is sub-micrometer. These high values of conductivity can be reached within metals, but for the semiconductors described in this theses Eq. 4.5 is valid. The second limitation is that it is only valid in the quasi-steady state appoximation, which implies that the photoconductivity dynamics should be slower than the THz pulse duration.

In a typically time-resolved THz spectroscopy experiment the transmitted electric field with pump $\tilde{E}_{pump}(\omega)$ and a reference, the electric field without pump $\tilde{E}_{ref}(\omega)$ are measured. The transmission through the unexcited film t_{ref} in terms of material properties is given by Eq. 3.37. The transmission function is the ratio between the transmission through an excited and

an unexcited film $\tilde{T}(\omega) = \tilde{E}_{pump}(\omega)/\tilde{E}_{ref}(\omega) = t_{film}/t_{ref}$. Dividing Eq. 4.5 by t_{ref} gives

$$\tilde{T}(\omega) = \frac{n+1}{n+1+Z_0 d\tilde{\sigma}(\omega)}. \tag{4.6}$$

In practise the complex functions $\tilde{T}(\omega)$ and $\tilde{\sigma}(\omega)$ are split into an amplitude and phase or real and imaginary part. Solving Eq. 4.6 for the conductivity and splitting it into a real σ_1 and imaginary σ_2 part using polar coordinates gives

$$\sigma_1 = \frac{n+1}{Z_0 d}\left[\frac{1}{|T(\omega)|}\cos\Phi(\omega) - 1\right], \tag{4.7}$$

$$\sigma_2 = -\frac{n+1}{Z_0 d}\left[\frac{1}{|T(\omega)|}\sin\Phi(\omega)\right], \tag{4.8}$$

where $|T(\omega)| = |E_{pump}(\omega)|/|E_{ref}(\omega)|$ is the amplitude and $\Phi(\omega) = \theta_{pump}(\omega) - \theta_{ref}(\omega)$ is the phase of the transmission function. The obtained complex photoconductivity is the photoconductivity of the sample at the time the THz pulse travels through sample. By changing the delay between the optical pump and the THz pulse, the complex photoconductivity at different times after optical excitation can be measured, which can provide information about the involved dynamics.

4.2 Drude conductivity

To describe the photoconductivity in a semiconductor, several models have been developed depending on the interaction of the charge carriers with the lattice [93–97]. These models have been successfully used to describe the photoconductivity at THz frequencies [20, 25, 26, 47, 48, 77, 98–101] In the simplest case the system can be described classically by an electron gas in a positively charged ionic lattice. The electrons will respond to an applied electric field and the damping caused by collisions with the almost static ionic lattice is described by a single scattering time τ. The equation of motion of free electrons is described by

$$\frac{\partial \vec{p}(t)}{\partial t} = -e\vec{E}(t) - \frac{\vec{p}(t)}{\tau} \tag{4.9}$$

where $\vec{p}$ is the impulse of the electron. In the frequency domain according to Fourier theory Eq. 4.9 will read

$$(-i\omega)m\vec{v}(\omega) = -e\vec{E}(\omega) - \partial\vec{v}(\omega)\tau \tag{4.10}$$

where m is the electron effective mass and v the electron velocity. Using ohms law $\vec{E}(\omega) = \vec{J}/\tilde{\sigma}(\omega)$ and an equation for the current density $\vec{J} = -ne\vec{v}$, an expression for the conductivity is obtained

$$\widetilde{\sigma}(\omega) = \frac{ne^2\tau/m}{1 - i\omega\tau}. \tag{4.11}$$

The term in the numerator is the DC-conductivity. The DC-conductivity can also be written as $\sigma_{DC} = ne\mu$, so this defines the carrier mobility as

$$\mu = \frac{e\tau}{m} \tag{4.12}$$

An other expression for the DC-conductivity is $\sigma_{DC} = \omega_p^2 \varepsilon_0 \tau$, which defines the plasma frequency as

$$\omega_p = \sqrt{ne^2/\varepsilon m} \tag{4.13}$$

If the equation for the Drude conductivity Eq. 4.11 is split in a real and imaginary part and by using the expression for the plasma frequency Eq. 4.13, we obtain

$$\sigma_1(\omega) = \frac{\omega_p^2 \varepsilon \tau}{1 + (\omega\tau)^2} \tag{4.14}$$

$$\sigma_2(\omega) = \frac{\omega_p^2 \varepsilon \tau^2 \omega}{1 + (\omega\tau)^2} \tag{4.15}$$

4.3 1D-spectroscopy

The obtained photoconductivity spectrum in a semiconductor material depends on the excited carrier density and on the mobility of those carriers, which both can be time-dependent. So by measuring E_{pump} and E_{ref}, only the photoconductivity at a single point in time is obtained. In all the measurements presented in this thesis, we assume that the conductivity dynamics is slow enough compare to the pulse duration of the THz wave so that a THz measurements can be treated as taking a snapshot of the conductivity of the sample. The leading edge and rear edge of the pulse will observe the same conductivity. To obtain information about the dynamics involved, it is necessary to do several measurements, where the time-delay between the optical pump and the THz-probe is changed. This is referred to 2D-spectroscopy. This can be a very time consuming process. Luckily, there is a faster method referred as 1D-spectroscopy. In this method only a single point of the THz pulse is measured. Because of the highest signal to noise ratio this point will be the peak of the THz pulse. So only the pump delay line will be scanned. The drawback is off-course that any frequency and phase information is lost. However, there can still be valuable information about the carrier dynamics extracted from the measurements. Because the phase information is lost, a requirement for using 1D-spectroscopy is that the conductivity response is

mainly real ($\sigma_1 \gg \sigma_2$) [102, 103]. The relation for the negative differential transmission in terms of the change in conductivity reads then

$$-\frac{\Delta T(t)}{T_0} = \frac{T_0 - T_{pump}(t)}{T_0} = 1 - \frac{n+1}{n+1+Z_0 d\Delta\sigma(t)}, \tag{4.16}$$

where T_0 is the value of the peak of the THz pulse that traveled through the unexcited sample. Solving for $\Delta\sigma(t)$ gives

$$\Delta\sigma(t) = \frac{N+1}{Z_0 d}(-\frac{\Delta T(t)}{T_0})[\frac{1}{1+\frac{\Delta T(t)}{T_0}}]. \tag{4.17}$$

If the change in transmission is small ($|-\Delta T(t)/T_0| < 20\%$), the differential THz transmission is directly proportional to the change in photoconductivity

$$\Delta\sigma(t) \approx \frac{N+1}{Z_0 d}|-\frac{\Delta T(t)}{T_0}|. \tag{4.18}$$

4.4 Experiments

4.4.1 Terahertz conductivity of GaAs

It is possible to measure the two pulses, reference and signal that are needed to obtain the THz photoconductivity simultaneously. This is achieved by using a double chopping scheme [104]. The benefit is that this assures equal environmental conditions for both measurements. In this scheme both the THz generation and the optical pump are chopped but with a different frequency. For the THz generation a frequency of 500 Hz is used, so one out of two pulses is blocked. For the pump two out of three pulses are blocked to achieve a frequency of 333 Hz. Two lock-in amplifiers locked to those two frequencies are used in the measurements. In this method, the reference pulse is given by $E_{ref} = V_{THz} + sV_{pump}$ and the signal pulse by $E_{pump} = V_{THz} - sV_{pump}$, where V_{THz}, V_{pump} are the measured voltages by the lock-in amplifiers and s is a constant that depends on the detector that is used. To obtain the value of s for this setup, a 1D-scan is performed. For a 1D-scan, only the signal will show a drop of the THz amplitude upon optical excitation. The reference should be constant. This revealed that $s = 1.1$ for the detector used in the experiments described here.

As example we will take again GaAs. For inducing a conductivity in a semiconductor material, electrons should be excited to the conduction band. This means that the photon energy of the pump should be large enough to exceed the bandgap of the semiconductor. The bandgap of GaAs is shown in Fig. 4.2. This figure is taken from Ref. [105]. The bandgap, which is for a direct bandgap material like GaAs, the energy different between the bottom of the Γ-valley of the conduction band and the top of the valence band and is for GaAs 1.424 eV. For these experiments wavelengths of 400 nm (3.1 eV)

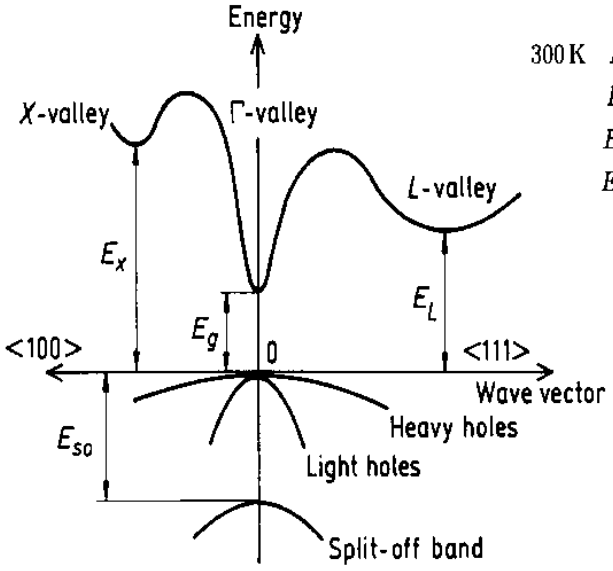

Figure 4.2: Schematic of the bandstructure of GaAs. Taken from Ref. [105].

and 800 nm (1.55 eV) were used. Note that for a photon energy of 3.1 eV also the L- and X-valleys can be reached. For the 2D-spectroscopy the carriers are excited with a 400 nm beam with a pump fluence of 5.1 μJ/cm^2. The reason for using 400 nm is that the penetration depth for 400 nm is much shorter (50 nm), then for 800 nm (1 μm) which means a better validity of Eq. 4.5. In a full 2D-scan the transmission of the whole THz pulse is measured at various pump-probe delay times. In this way the conductivity dynamics over the full THz bandwidth can be studied. Here, we will show only the THz pulses measured at one pump-probe delay time.

The pulses shown in Fig. 4.3 are recorded at 10 ps after optical excitation. The green line is the reference, where the pump was blocked and the red line is the pump signal travelling through the photoexcited sample. By waiting long enough after optical excitation, we can assume that the carriers have already decayed to the bottom of the Γ-valley, see Fig. 4.2 when the THz pulse travels through the excited film [26]. An other reason for waiting 10 ps is that measurements shortly after optical excitation are influenced by the detector response. However, it is possible to correct for that and obtain information about the photoconductivity directly after optical excitation. The two pulses shown in Fig. 4.3 are Fourier transformed and by using Eqs. 4.7 and 4.8 the THz photoconductivity is calculated. The refractive index n of GaAs at THz frequencies is 3.6, $Z_0 = 377\Omega$ and as thickness d, the penetration depth (50 nm) is taken.

Fig. 4.4 shows the THz photoconductivity of GaAs measured 10 ps after optical excitation, where the squares are the real part σ_1 and the triangles

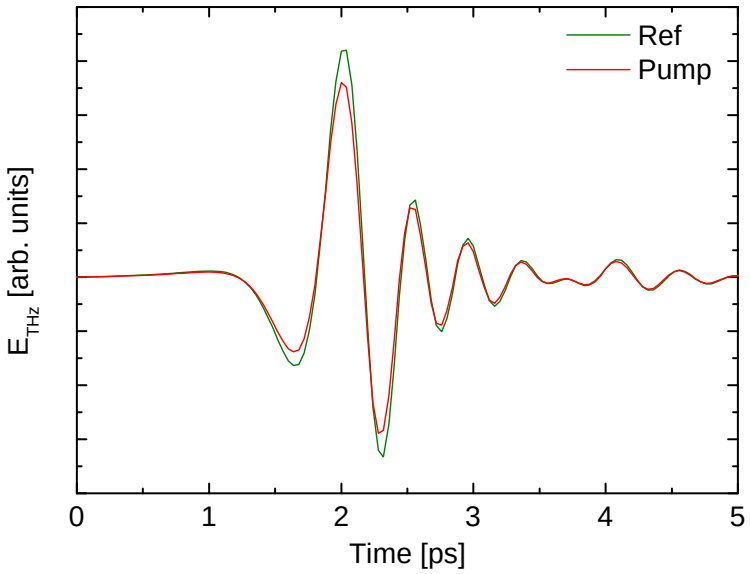

Figure 4.3: Electric field of the THz transients traveling through an unexcited GaAs sample (green line) and traveling through an optically excited GaAs sample (red line). The sample was excited with a wavelength of 400 nm and with a pump fluence of 5.1 μJ/cm^2. The peak of the THz pulses traveled through the excited film 10 ps after optical excitation.

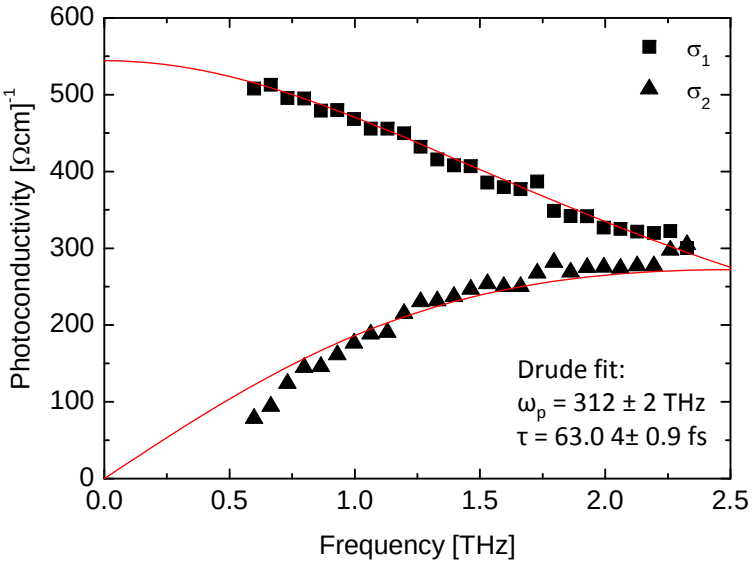

Figure 4.4: Photoconductivity of GaAs, measured 10 ps after optical excitation with a pump fluence of 5.1 μJ/cm^2. The squares, σ_1 represent the real part of the conductivity and the triangles, σ_2 the imaginary part of the conductivity. The red lines is a fit with the Drude model.

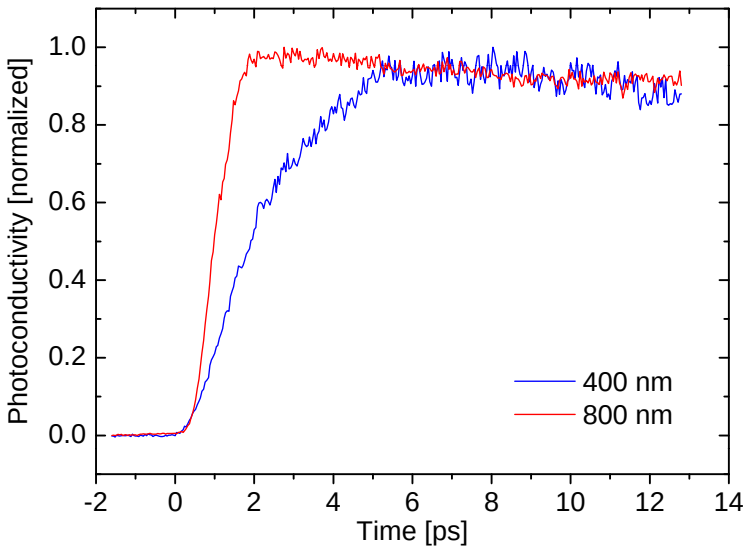

Figure 4.5: Normalized photoconductivity dynamics of bulk GaAs with pump excitation wavelength of 400 nm (blue line) and 800 nm (red line).

are the imaginary part σ_2 of the photoconductivity. The red lines is a fit with the Drude-model (Eqs. 4.14 and 4.15), where the real and imaginary part of the photoconductivity are fitted simultaneously. The fit reveals a plasma frequency of $\omega_p = 312 \pm 2$ THz, and a scattering time of $\tau = 63.0 \pm 0.9$ fs. From the plasma frequency the carrier density can be obtained according to Eq. 4.13: $N = 1.93 \pm 0.02 \cdot 10^{18}\text{cm}^{-3}$ and from the scattering time the mobility according to Eq. 4.12: $\mu = 1.76 \pm 3 + 0.02 \cdot 10^3$ cm^2/Vs. The carrier density can also be estimated from the excitation fluence. A pump fluence of 5.1 μJ/cm^2 at 400 nm, which is absorbed in a 50 nm layer results in a carrier density of $1.2 \cdot 10^{18}\text{cm}^{-3}$, where we take into account that an wavelength of 400 nm results in a Fresnel reflection coefficient of 0.4 in GaAs. The estimated carrier density of $1.2 \cdot 10^{18}\text{cm}^{-3}$ is in good agreement with the carrier density of $1.93 + 0.02 \cdot 10^{18}\text{cm}^{-3}$ obtained from the measured plasma frequency.

Measuring a Drude conductivity in optically excited GaAs is a method for testing the setup, before taking a sample with an unknown photoconductivity response. An example why testing is important is for instance if the pump spot size is too small [106]. In that case the measurement will lead to misinformation because the lower frequencies which have a larger defraction limit and hence a larger spot size, observe a lower carrier density. This will lead to a deviation from the Drude conductivity.

4.4.2 Photoconductivity dynamics of GaAs

Also 1D-scans are performed to show the frequency integrated conductivity dynamics and will show that although the frequency information is lost, still valuable information can be extracted from these 1D-scans. For the 1D-scans the lowest noise is obtained by chopping the pump beam only. By chopping the pump beam and locking the lock-in amplifier to that frequency, only the changes due to the pump are measured, which is $T_0 - T_{pump}(t) = -\Delta T(t)$. For calculating the conductivity dynamics according to Eq. 4.17, also T_0 should be measured. Since T_0 is constant in a 1D-scan, the average of a few data points is sufficient. The carriers are excited with two different wavelength, with 800 nm where the carriers are generated close to the bottom of the Γ-valley and with 400 nm where the carriers obtain higher energies and can reach the L-valley, see Fig. 4.2. The results are shown in Fig. 4.5, where the red line is for 800 nm excitation and the blue line is for 400 nm excitation. The obtained photoconductivity is normalized for comparison between the two different excitation wavelengths. As can be seen, the rise in the photoconductivity due to optical excitation is slower in the case of excitation with 400 nm. This is because carriers are excited into the L-valley, where their mobility is lower. In the Drude model, the mobility of a carrier in the bottom of a valley depends on the effective mass which is determined by the curvature of the valley. The lower mobility in the L-valley will lead to a lower photoconductivity and it takes a while before the carriers decay to the high mobility Γ-valley. For the same reason, only the electrons are considered. Although upon optical excitation an electron-hole pair is created, the holes are neglected because of their relatively large effective mass. The hole mobility is usually much less then the electron mobility and therefore the holes will not have a significant contribution to the photoconductivity.

Part II

Experiments

Chapter 5

Capture and release of carriers in InGaAs/GaAs quantum dots

5.1 Introduction

In this first experimental chapter, we describe time-resolved THz spectroscopy experiments on InGaAs/GaAs quantum dots. A quantum dot is a structure that is smaller in all three dimensions then the electron wavelength in bulk materials. The reduced size leads to the confinement of the electron and hole wavefunctions and hence to quantization of the electron and hole states. The energy levels of the states will depend on the size of the quantum dot. In our case where on an assemble of quantum dots is measured, a distribution of sizes and hence energy states is observed. This quantization of the electron and hole states have an other important consequence. The density of states is very small compare to bulk material, which means that the optical properties will change when charge carriers occupy the quantum dot states due to state filling. [33, 107, 108]. Furthermore, the small density of states in the InGaAs quantum dots compare to the bulk GaAs barrier states will have consequences for the carrier exchange between the two materials. This process as well as the ultrafast carrier dynamics in the quantum dot itself has been widely studied for better understanding of quantum dot based optical devices, such as quantum dot lasers [32, 33], quantum dot infrared photodetectors [39, 40, 109] and quantum dot semiconductor saturable absorber mirrors (SESAM) [33, 107, 108, 110]. Several ultrafast optical techniques, like time-resolved photoluminescence [111–113], optical pump-probe spectroscopy [114–116] and time-resolved THz spectroscopy in both colloidal [44, 49, 51, 117] and self-assembled [46, 116, 118, 119] quantum dots have been used.

An important parameter in quantum dots based electrooptic devices is the carrier life-time. It e.g. influences the speed of an optical switch, the speed of a fast photodetector, the working of a laser i.e. the trapping of

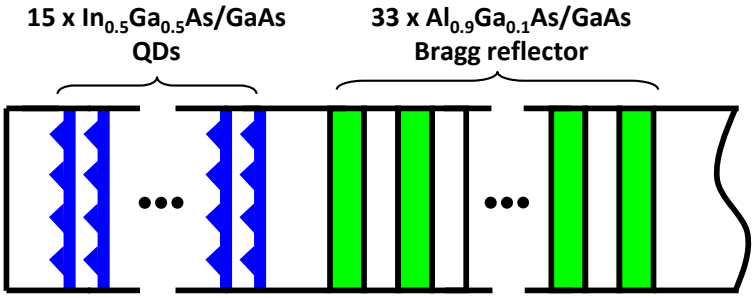

Figure 5.1: Schematic of the structure of the $In_{0.5}Ga_{0.5}As/GaAs$ quantum dot SESAM.

carriers into the quantum dot should be much faster than the electron-hole recombination to create population inversion. For the proper working of a SESAM, the electron-hole recombination time should be significantly longer than the pulse duration of the laser. THz spectroscopy is an excellent technique to measure the carrier lifetime in semiconductor materials due to its sensitivity to free carriers. Specifically for quantum dot systems it can measure the trapping time of charge carriers into the quantum dots due to the zero mobility in the quantum dots. This has been measured in various studies [46, 116, 119, 120]. For measuring the electron-hole recombination in the quantum dots different spectroscopy techniques are needed like e.g. time-resolved photoluminescence or optical pump-probe spectroscopy. In this work we studied not only the trapping of carriers into the quantum dot but also the reverse process, the release of carriers from the quantum dots into the wetting layers and barrier states with an optical pump - terahertz probe technique [121]. The latter process has to the best of our knowledge not been measured before. One of the reasons is that the signal from the release process is much weaker. Even at room-temperature the energy difference between the quantum dot ground state and the barrier state is larger than kT. To solve this problem we used a quantum dot SESAM, which has a Bragg reflector after the quantum dot layers, which prevents absorption in the thick substrate. Besides enabling to measure the release of charge carriers from the quantum dots into the barrier states, using a quantum dot SESAM has the extra benefit, that we directly study the carrier dynamics in an electooptic device.

5.2 Sample

The capture and release of carriers is measured in a quantum dot semiconductor saturable absorber mirror (SESAM) structure. A SESAM can be used for passive mode-locking [107]. At higher intensities the quantum dot states get filled, which will decrease the absorption coefficient. This saturation of

the absorption leads to a higher reflectivity of the mirror.

The sample is grown by molecular beam epitaxy. A schematic of the sample structure is shown in Fig. 5.1. It consists of 15 layers of $In_{0.5}Ga_{0.5}As/GaAs$ quantum dots, separated by GaAs barrier layers. The quantum dots density is estimated at 10^{10} cm^{-2}. The total thickness of the quantum dots and barriers is 611 nm. On top of the quantum dots structure is a 33-layer $Al_{0.9}Ga_{0.1}As$ Bragg reflector. The Bragg reflector has a 100-nm-wide stopband centered around 1060 nm (Fig. 5.2).

Besides the small signal reflectivity of the quantum dot SESAM, the room-temperature photoemission spectra of the quantum dot ground state (GS) is shown in Fig. 5.2. For the photoemission experiment carriers are excited with a 800 nm beam into the barrier layers. Part of the carriers will be trapped into the quantum dots. The emission caused by the recombination of electrons and holes from the quantum dot ground state is measured with a standard optical spectrometer. The emission spectrum has a central wavelength around 1017 nm and a full-width half maximum (FWHM) of 14 nm. As can be seen the quantum dot ground state luminescence lays within the stopband of the Bragg reflector. Emission from a large amount of quantum dots will be inhomogeneously broadened, due to a distribution in the quantum dot size. Different sizes lead to a difference in the quantum confinement effect and hence to differences in the energy level of the quantum dot ground state. Inhomogeneously broadening will lead to a Gaussian lineshape, however a Lorentzian lineshape is observed. A possible explanation for the observed Lorentzian lineshape is that stimulated emission takes place.

The Bragg reflector is important in our experiment in the case of resonantly excitation into the quantum dot ground state. The optical pump beam is reflected at the Bragg grating, preventing carrier excitation in the thick GaAs substrate by two-photon absorption, which could easily obscure the signal from the release of carriers from the quantum dots.

The ultrafast processes relevant for our experiments after optical excitation in the quantum dot ground state and in the barrier state are shown in Fig. 5.3. Only carriers in the barrier state and wetting layer, here referred as the conducting state (marked in blue in Fig. 5.3), will contribute to the conductivity. Carriers in the quantum dot states are confined in all dimension and will therefore have zero mobility. As described in chapter 4, the terahertz pulse will only be absorbed by "free" carriers. So the trapping of carriers into the quantum dots can be observed by an increase in the terahertz transmission and the release of carriers from the quantum dots into the conducting states leads to a decrease in the transmission of the THz pulse. Exchange of carriers between the barrier states and the wetting layer should also change the conductivity, because the mobility of carriers in the wetting layers is lower than in the barrier states. For simplicity only the conduction band with electron capture into the quantum dots, the release

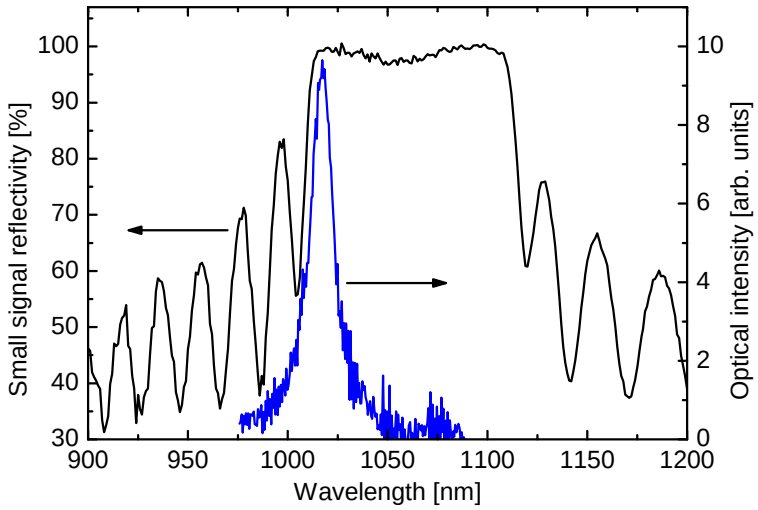

Figure 5.2: Small signal reflectivity of the $Al_{0.9}Ga_{0.1}As$ Bragg reflector (black line). Photoluminescence spectrum from the the quantum dot ground state (blue line).

of electrons into the conducting state and carrier recombination in both the quantum dots and conducting state are shown. These are also the most important mechanisms in the observed dynamics. Although upon optical excitation electron-hole pairs are created, the main contribution to the photoconductivity comes from the electrons, due to their smaller effective mass and hence higher mobility than the holes. Also important for the ultrafast carrier dynamics in quantum dots are intradot carrier relaxation, carrier-carrier and carrier-phonon scattering. All these process are temperature and carrier density dependent [115, 122].

5.3 Experiments

5.3.1 Setup

The setup for these experiments is in detail described in section 2.4 and shown in Fig. 2.5. For these experiments two different pump wavelength were used. The original 800 nm output of the Ti:sapphire amplifier is used to excite carriers into the GaAs barrier states. For pumping carriers directly into the quantum dot ground state, the 800 nm beam is sent trough an optical parametric amplifier to generate pulses with a central wavelength of 1024 nm and a FWHM 45 nm. The spectrum of these pulses are shown in Fig. 5.4, together with the emission from the quantum dot ground state. The overlap shows that the pulses from the optical parametric amplifier are able to excite carriers directly into the quantum dot ground state.

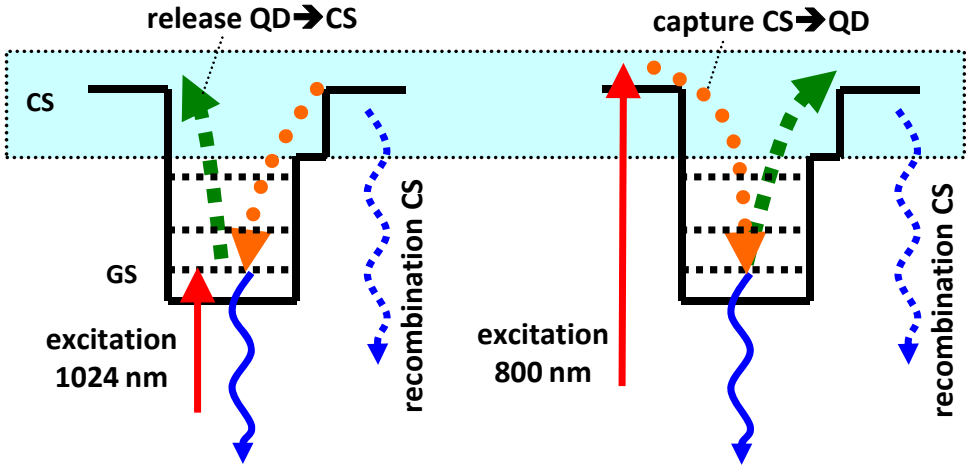

Figure 5.3: Capture and release processes of electrons in a quantum dot. QD: quantum dot, GS: quantum dot ground state, CS: conducting state.

5.3.2 Barrier pumping

As described in chapter 4, the fastest way of measuring carrier dynamics with time-resolved terahertz spectroscopy is to measure only the peak of the terahertz pulse as function of pump-probe delay time. To measure the carrier capture dynamics into the quantum dots, carriers were excited into the barrier state with a pump excitation wavelength of 800 nm. We calculate the relative change in transmission of the THz pulse into a sheet conductivity according Eq. 4.17 and $\Delta\sigma_{\square} = \Delta\sigma \cdot d$, where σ is the normal conductivity and d is the thickness of excited layer. The reason for using a sheet conductivity instead of the normal photoconductivity (Eq. 4.17) is that in the case carriers are excited into the quantum dot ground state (described in next section) and then released from the quantum dots into the conducting states, it is not so clear what the thickness of the conducting layer is. The sheet conductivity describes the conductivity independent of the thickness. The time dependence of the frequency integrated change in sheet conductivity $\Delta\sigma_{\square}$, for pump fluences in the range 0.04-1.18 μJ/cm^2 are shown in Fig. 5.5. A near instantaneous rise of the photoinduced conductivity is observed, followed by a fast decay and a long-lived contribution. For getting the photoconductivity at zero before optical excitation, a small contribution from some very long-lived carriers that survive the optical cycle of 1 ms is subtracted. The fast decay is attributed to carrier capture into the nonconducting quantum dot states. To support this interpretation, the change in the photoinduced conductivity of bulk GaAs is measured (black curve in Fig. 5.5), which shows a much slower initial decay. The long-lived component is most likely caused by carriers excited in the Bragg reflector,

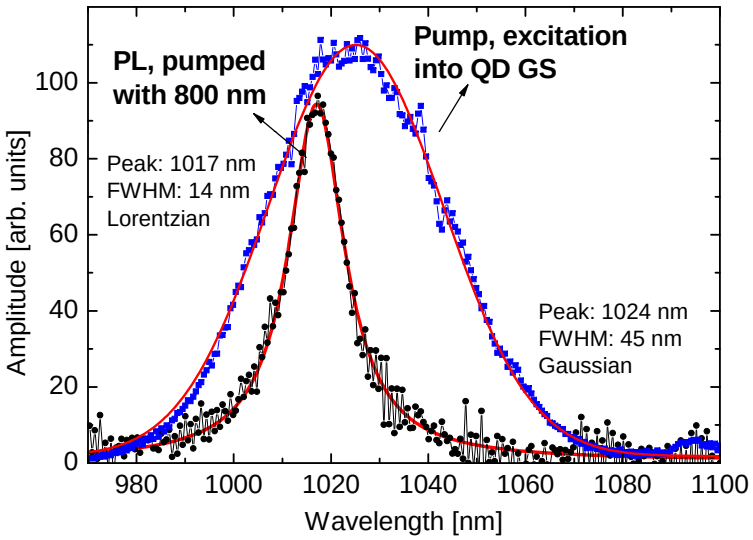

Figure 5.4: Photoluminescence spectrum from the the quantum dot ground state (black dots), the red line is a fit with a Lorentzian lineshape. Spectrum of the pulses coming from the optical parametric amplifier (blue dots), the red line is a fit with a Gaussian lineshape.

which is accessible for 800 nm light (Fig. 5.2). The Bragg reflector is a type-II $Al_{0.9}Ga_{0.1}As$ semiconductor, causing separation in space of electrons and holes, via Γ-X transfer [123]. This means that the lowest energy level of a X-valley bandstate of the barrier is lower than the lowest energy level of the Γ-valley bandstate in the quantum well. This means that electrons can be transferred to the barrier layer, where the energy is lower, while the holes remain in the quantum well. The electron-hole recombination rate depends on the overlap of the electron and hole wavefunctions. A more detailed description of this mechanism will be explained in chapter 6. The little bump at around 22 ps (Fig. 5.5) is an experimental artifact due to double reflection in a 2-mm thick beam attenuator.

Fig. 5.6 shows the peak conductivity as function of pump fluence. The red line is a linear fit to the data. The initial rise in conductivity depends linearly on excitation fluence, as expected for single-photon absorption. From the fast decay of the photoconductivity, the trapping time into the quantum dots can be estimated. In Fig. 5.7, the time required for the conductivity to drop by 10% from its maximum, as function of pump fluence is plotted. This 10% is chosen because the total fast decay is only about 20%, due to the long-lived carriers in the Bragg-reflector. A near-linear growth of the 10% decay time from 1.2 to 5.7 ps is observed, with increasing pump fluence. This growth in trapping time with increasing pump fluence is in agreement with observation made in Refs. [46, 102, 119, 120] and is attributed to

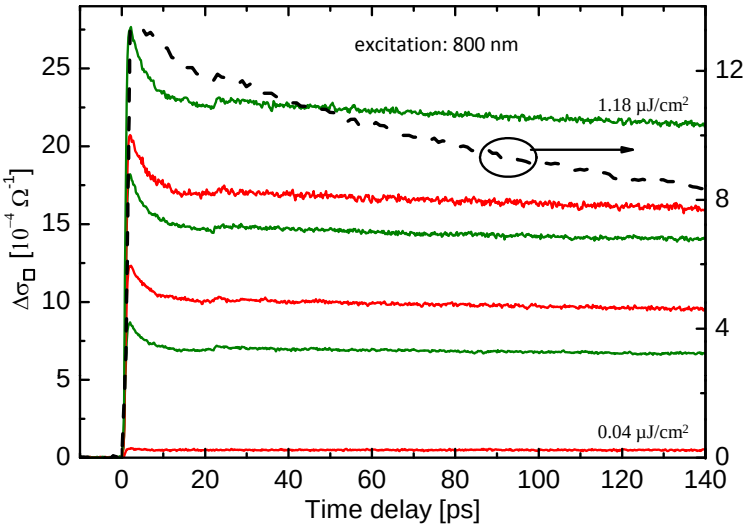

Figure 5.5: Solid lines: Dynamics of the photoinduced sheet conductivity of a quantum dot SESAM, $\Delta\sigma_{\square}$ at optical excitation with 800 nm into the barriers with pump fluences in the range of 0.04-1.18 μJ/cm^2. Dashed line: Dynamics of $\Delta\sigma_{\square}$ for bulk GaAs pumped at 800 nm with a pump fluence of 3.6 μJ/cm^2.

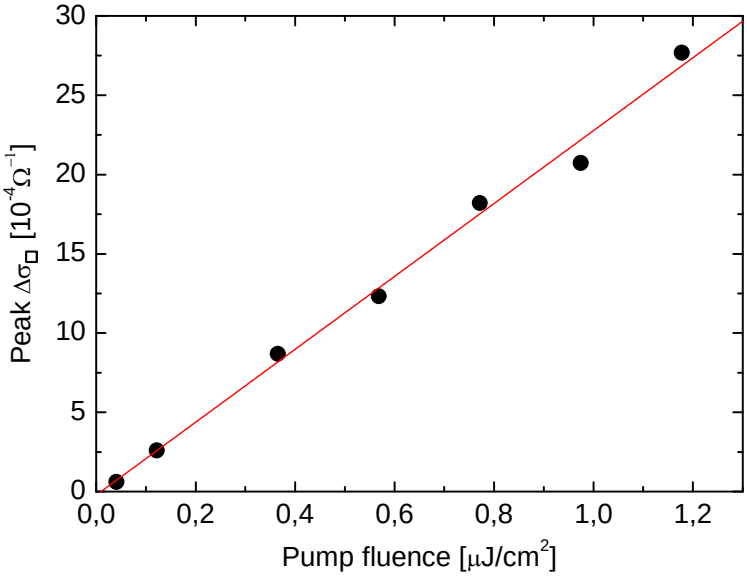

Figure 5.6: Peak of the $\Delta\sigma_{\square}$ dynamics traces shown in Fig. 5.5 as function of pump fluence. The red line is a linear fit to the data.

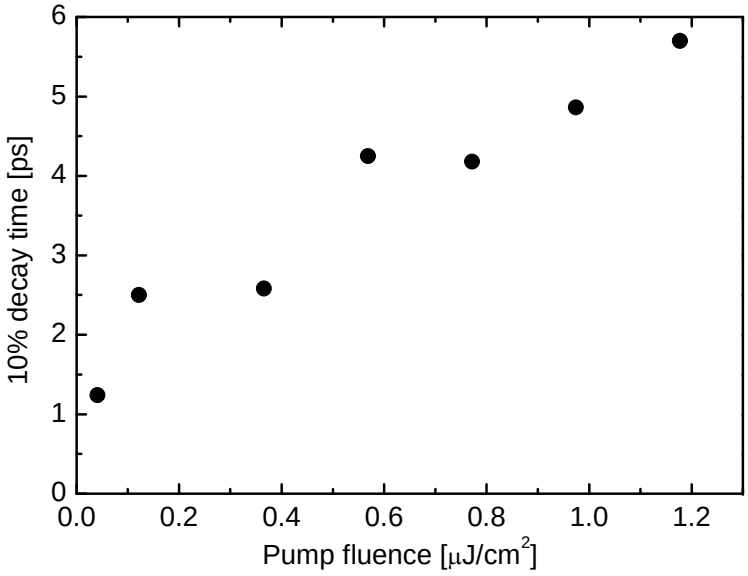

Figure 5.7: Time it takes for the photoconductivity to drop by 10% as function of pump fluence.

filling of the quantum dot trap states at higher excitation fluences, which decreases the trap efficiency. However, these observation are in contrast to the observed decrease in trapping time in Refs. [115, 116]. The different technique used in Ref. [115], where only the population of the quantum dot ground state is measured may explain the different observation. The suggested trapping mechanism electron-electron scattering may also provide carriers back into the conducting states from the higher-lying quantum dot states, thereby slowing down the decay dynamics of the conductivity. It is not clear what causes the difference between Ref. [116] and our observations.

5.3.3 Ground-state pumping

To observe the release of carriers from the quantum dots into the conducting states, carriers are resonantly excited into the quantum dot ground state at a wavelength of 1024 nm, with pump fluences in the range 2.1-22.8 μJ/cm^2. The sheet conductivity dynamics is shown in Fig. 5.8. A non-instantaneous rise of the photoconductivity, which peaks after approximately 35 ps after photoexcitation, followed by a slow decay is observed. We interpret the slow rise time of the photoconductivity as release of carriers into the conducting state. After 35 ps the recombination in the barrier states and wetting layers becomes the dominant process, causing the decay of the photoconductivity.

To illustrate the dynamics a simple rate-equation model is applied that only include the creation of carriers in a nonconducting state (the quantum

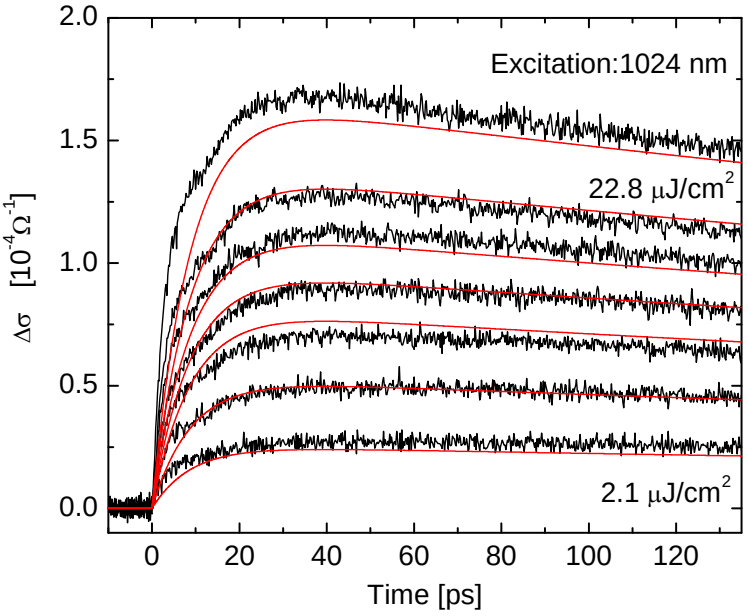

Figure 5.8: Dynamics of the photoinduced sheet conductivity of a quantum dot SESAM, $\Delta\sigma_{\square}$ at optical excitation with 1024 nm into the quantum dot ground state with pump fluences in the range 2.1-22.8 μJ/cm^2 (black curves). Carrier density in the barrier layer when excited to the quantum dot ground state based on a simple rate equation model (red curves), a scaling factor is used to fit the photoconductivity dynamic traces.

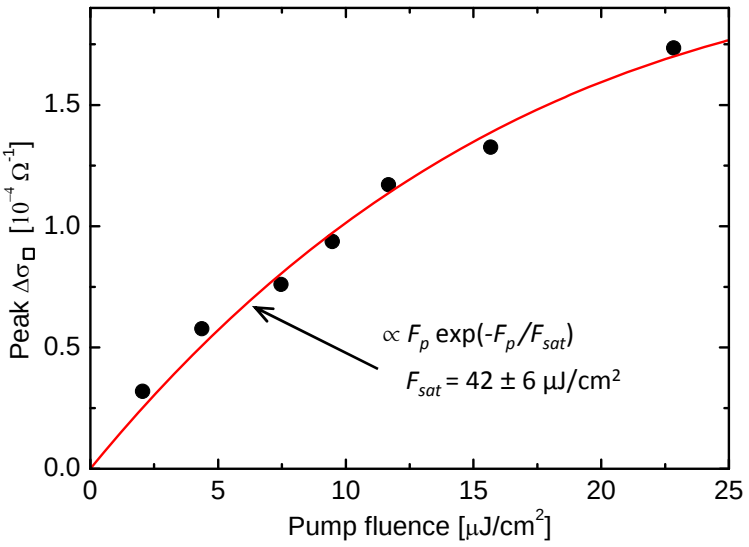

Figure 5.9: Peak of the $\Delta\sigma_{\square}$ dynamics traces shown in Fig. 5.8 as function of pump fluence. The red line is a fit with a saturable absorption function, with a saturation fluence of 42 ± 6 μJ/cm^2.

dot) at $t = 0$ by a short optical pulse, the release of carriers from the quantum dot to a conducting state, the trapping of carriers from the barrier state to a nonconducting state and the electron-hole recombination in both the quantum dots and the conducting barrier layers. The rate equations read:

$$\begin{aligned} \frac{\partial N_{QD}}{\partial t} &= f_{QD} N_{gen}(t) + f_{QD} \frac{N_{barrier}}{t_{trap}} - \frac{N_{QD}}{t_{recqd}} - \frac{N_{QD}}{t_{rel}}, \\ \frac{\partial N_{barrier}}{\partial t} &= \frac{N_{QD}}{t_{rel}} - (1 - f_{QD}) \frac{N_{barrier}}{t_{recbar}} - f_{QD} \frac{N_{barrier}}{t_{trap}}, \end{aligned}$$

where N_{QD}, $N_{barrier}$ are respectively the carrier density in the quantum dots and in the conducting barrier layer, $N_{gen}(t)$ is the generation term which is time dependent and the amplitude is different for the different pump fluences, t_{trap}, t_{rel}, t_{recqd}, t_{recbar} are respectively the trapping time into the quantum dots, the release time from the quantum dots into the barrier layer, the recombination time in the quantum dots and the recombination time in the barrier layer, f_{QD} is a constant factor taking into account that the quantum dots occupy only a small volume of the sample.

Fig. 5.8 shows the carrier density in the barrier layer as function of time for the different pump fluences (red curves). A scaling factor is used to compare it with the measured photoconductivity (black curves). In this model we used $t_{rel} = 10$ ps, $t_{recqd} = 120$ ps and $t_{recbar} = 950$ ps. The trapping time is defined as $t_{trap} = t0_{trap}/(1 - N_{QD}/N_{max})$ with $t0_{trap} = 1.2$ ps. This equation describes that for a weak pump fluence the trapping time is 1.2 ps, but if the pump fluence increases the trapping time increases due to state filling as described in Sec. 5.3.2. This model shows that the observed slow increase of photoconductivity which peaked at 35 ps and then decreases can be well explained by the net release of carriers from the quantum dots to the barrier state with a release time of 10 ps and an electron-hole recombination time of 950 ps.

Fig. 5.8 also shows the shortcoming of this simple rate-equation model. A deviation between the model and the measurements is observed in the first 10 ps after optical excitation. The observed increase shows a kink, with first a fast increase and then a slower increase, which is not shown in the model. We do not know what causes the kink, but a possible explanation of the deviation between the model and the measurement is that the model does not include the wetting layer which has a lower mobility than the barrier layer. So an exchange of carriers between the wetting layer and the barrier state will also lead to a change of the photoconductivity. Also not included is that there are several quantum dots states. Although exchange between the different quantum dot states will not change the photoconductivity, the probability of release to the conducting state is different for the different quantum dot states. A smaller energy difference between the quantum dot state and the barrier state will give a higher probability.

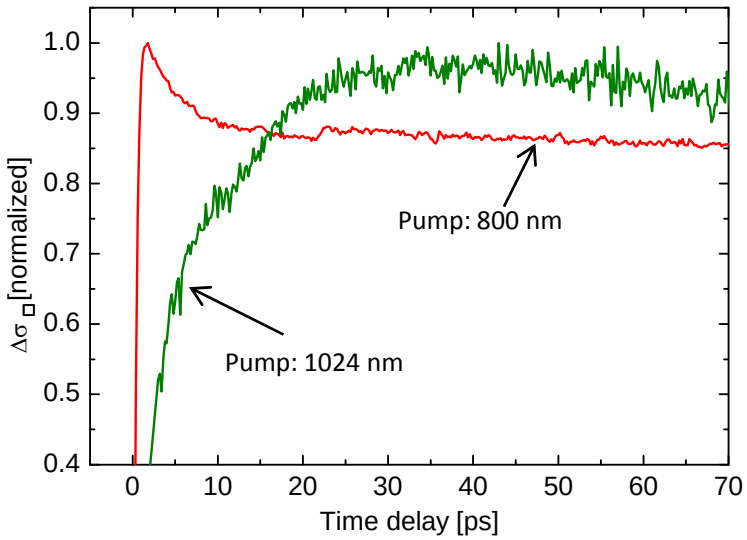

Figure 5.10: Normalized dynamics of the photoinduced sheet conductivity of a quantum dot SESAM, $\Delta\sigma_{\square}$ at optical excitation with 800 nm into the barriers (red line) and with 1024 nm into the quantum dot ground state (green line).

The peak photoconductivity has a sub-linear dependence on the pump fluence (Fig. 5.9), suggesting that the rise in conductivity is caused by a saturated one-photon process, expected for resonantly excitation into the quantum dot ground state. For higher pump fluences the quantum dot ground states get more occupied causing a decrease in the absorption coefficient. From the fits to the saturable absorption [124] function, $\propto F_p \exp[-F_p/F_s]$, where F_p is the pump fluence and F_s is the saturation fluence, a saturation fluence of 42 ± 6 μJ/cm^2 is obtained. This is in reasonable agreement with a value of $F_s = 25$ μJ/cm^2, observed in a similar quantum dot-based structure [110].

The energy gap between the quantum dot ground state and the wetting layer was measured in a similar structure to be 252 meV, shared approximately 60%/40% between the electron and hole states [115]. This is significantly larger than $k_B T = 26$ meV at room-temperature for the quantum dot ground state - wetting layer transition for both electrons and holes. However, the release of carriers observed after optical excitation into the wetting layer can be explained by the large density of states in the wetting layer compared to the quantum dot states, which should increase the probability of carrier release.

5.4 Conclusion

We have demonstrated the difference in photoconductivity dynamics of an InGaAs/GaAs SESAM (Fig. 5.10), depending on whether carriers were optically excited resonantly into the quantum dot ground state (green line) or into the barrier state (red line). When carriers are excited into the barrier layers with a single photon absorption process, the photoconductivity increases near-instantaneous. A fast decay of a few picosecond is caused by carriers that are trapped into the quantum dot. The decay time depends on the carrier density, where a higher carrier density leads to state filling of the quantum dot states and hence to a longer decay time of the photoconductivity. Carriers excited into the AlAs/GaAs Bragg reflector caused a large very slow decaying part of the photoconductivity.

When carriers are excited to the quantum dot ground state, a maximum photoconductivity is measured 35 ps after optical excitation due to the release of carriers from the quantum dots into the conducting barrier layers. A simple rate equation model revealed a release time of about 10 ps. The observed slow decay after 35 ps is caused by electron-hole recombination in the barrier states, which after 35 ps dominates the carrier dynamics. The working of the SESAM is shown in the maximum photoconductivity at 35 ps as function of pump fluence, which saturates. This saturation in the absorption is caused by filling up the quantum dots states for higher pump fluences. The observed saturation fluence of 42 ± 6 μJ/cm^2 is comparable with other quantum dot based SESAMs.

The experiments described in this chapter showed that the trapping of carriers into the quantum dots, the release of carrier from the quantum dots into the barriers and electron-hole recombination in the barrier layer are the main contributors to the photoconductivity dynamics. However the simple rate-equation model showed that it is not the complete story. An important feature is the kink around 10 ps, which can not be explained by the processes described above. For explaining the early dynamics a more detailed model is needed, which include the wetting laying and several quantum dot states. An extra step to make the model more accurate is to include a temperature and carrier density dependence on all the processes. While in the simple model described above only the change in trapping time due to state filling is taken into account.

An other important question about the carrier dynamics which the experiments described in this chapter does not answer is which physical process causes the release of carriers from the quantum dot ground state into the barrier layers (e.g. thermal excitation or carrier-carrier scattering). To answer this question a temperature dependent study could be done. Thermal excitation is strongly temperature dependent and should complete disappear at liquid helium temperatures. If thermal excitation is important for the release of carrier from the quantum dots into the barrier states. The pho-

toconductivity dynamics would look completely different at liquid helium temperatures. Carrier-carrier scattering on contrary does not depend much on temperature, so even at liquid helium temperatures this process would still take place and a strong release of carriers from the quantum dots into the barriers would be observed.

Furthermore, the carrier dynamics in the quantum dots are not discussed because this is invisible with the experiments described here. To observe the exchange of carriers between the different quantum dot state one could tune the THz pulse to the energy difference between two states. This means that higher frequencies than generated in the experiment described here are needed. For example if a broadband THz pulse is generated that includes the energy difference between the quantum dot ground state and the first excited state, a dip at this frequency would be observed when carriers are excited to the quantum dot ground state (i.e. the THz pulse excite the carriers to the first excited state). However this absorption will go down if the first excited state gets occupied due to state filling. So the THz pulse can be used as a measure for the population in the first excited state in the quantum dot.

Chapter 6

Ultrafast carrier dynamics in InGaN/GaN multiple quantum wells

6.1 Introduction

The understanding of the ultrafast dynamics in group-III nitride based quantum wells is important for the development of wide bandgap semiconductor devices, such as LEDs and lasers in the blue-green spectral region [125, 126]. The development of LEDs and lasers in blue-green spectral region is important for e.g. white light LEDs and due to the smaller wavelength, blue lasers can be used to write and store more data on a disk. Group-III nitride based quantum wells can have large built-in piezoelectric fields. These piezoelectric fields are caused by the lattice mismatch between GaN and InN or AlN. This lattice mismatch causes strain in the material and this results due to the large piezoelectricity of GaN in a large built-in piezoelectric field. This strain-induced built-in piezoelectric field has significant influence on the optical and electronic properties, described by the quantum confined Stark effect [127]. When an electric field is applied on a semiconductor material the bandstructure will tilt. This tilt will result in a change of the valence-conduction band transition energy, which is called the Stark shift. This Stark shift is larger in a quantum confined system, because the confinement prevents the annihilation of the electron-hole pair by complete separation of the electrons and holes. The quantum confined Stark effect will manifest itself by a strong dependence of the transition energy, absorption coefficient and recombination rate on the carrier density in the quantum well, due to screening of a build-in piezoelectric field. This screening leads to the emission of THz transients [120, 128] and high-amplitude acoustic waves [129–131]. The dependency of the transition energy on the carrier density is well studied by photoluminescence experiments [132–135]. The dependency

of the absorption coefficient on the carrier density has been studied in a previous terahertz investigation [120]. In this work we concentrate on the last carrier density dependent phenomena: the recombination rate, by using time-resolved terahertz spectroscopy.

InGaN/GaN multiple quantum wells are due to their large built-in piezoelectric field (much larger then can be applied externally) a good sample to study the behavior of carriers in a biased system. This is valuable information for like e.g. electrically controlled saturable absorber mirrors [136], where instead of a built-in piezoelectric field an externally applied electric field is used to control the modulation depth of the SESAM.

6.2 Samples

The samples consist of a 10-layer $In_{0.2}Ga_{0.8}N$/GaN multiple quantum well with well thicknesses of 1.8, 2.7 and 3.6 nm. The barrier width is 7 nm for all samples. The quantum well structure is sandwiched between a 180 nm thick capping layer and a 2 μm buffer layer. The sample is grown on a sapphire substrate by metalorganic vapor-phase epitaxy (Fig 6.1). The lattice mismatch between InGaN and GaN causes strain in the material, which results in large built-in piezoelectric fields of 3.1 MV/cm in the quantum wells and 0.5 MV/cm (with opposite polarity) in the barriers [120, 137].

The optical properties of a biased system are well described by the quantum confined Stark effect [127]. The tilt of the bandstructure (Fig. 6.2(a)) results in a smaller transition energy and the reduction of the spatial overlap between the electron and hole wavefunctions leads to a smaller transition probability. Upon excitation with an ultrashort laser pulse, a dipole moment is created due to the shifted position of the electron and hole wavefunctions. This dipole moment has a polarity opposite to that of the built-in piezoelectric field and thus it will partly screen this field. With strong excitation fluences complete screening of the built-in piezoelectric field can be achieved (Fig. 6.2(b)). The screening results in flattening of the bandstructure and hence in an increase of the optical transition energy and transition probability. Since every photoexcited carrier contributes to the screening, this process is highly dynamical. As the carriers recombine the reverse process will take place. Recombination of electron-hole pairs decreases the dipole field and thus causes the restoration of the built-in piezoelectric field. This implies that during the recombination process the recombination rate will slow down due to the increased spatial separation of the wavefunctions.

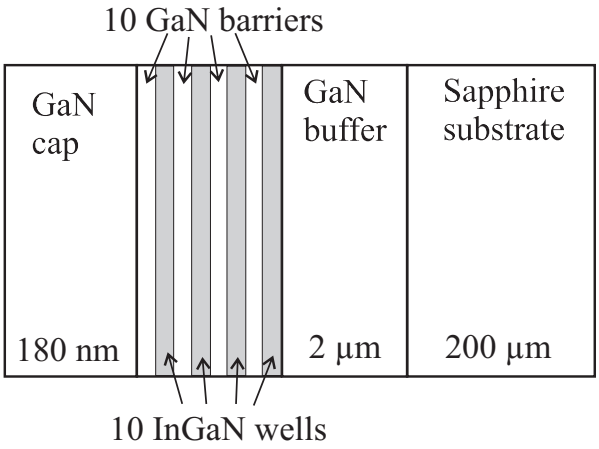

Figure 6.1: Schematic of the structure of the InGaN/GaN multiple quantum well sample.

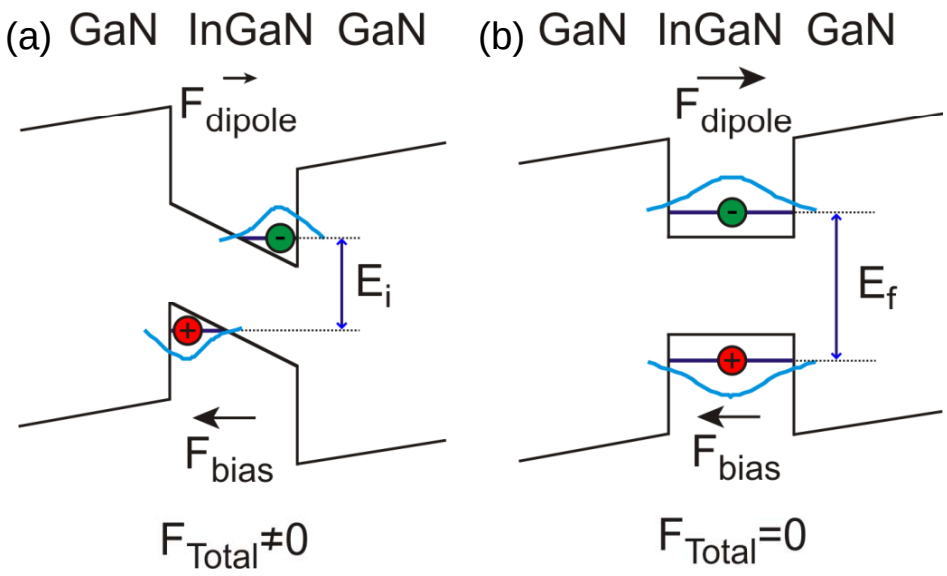

Figure 6.2: (a) Schematic of the bandstructure of an InGaN/GaN quantum well, with a built-in piezoelectric field. E_i - initial transition energy, F_{dipole} - dipole field from an excited electron-hole pair, F_{bias} - bias electric field from the build-in piezoelectric field, F_{total} - total electric field (F_{dipole}+F_{bias}). (b) Schematic of the bandstructure of an InGaN/GaN quantum well, where the build-in piezoelectric field is completely screened. E_f - final transition energy.

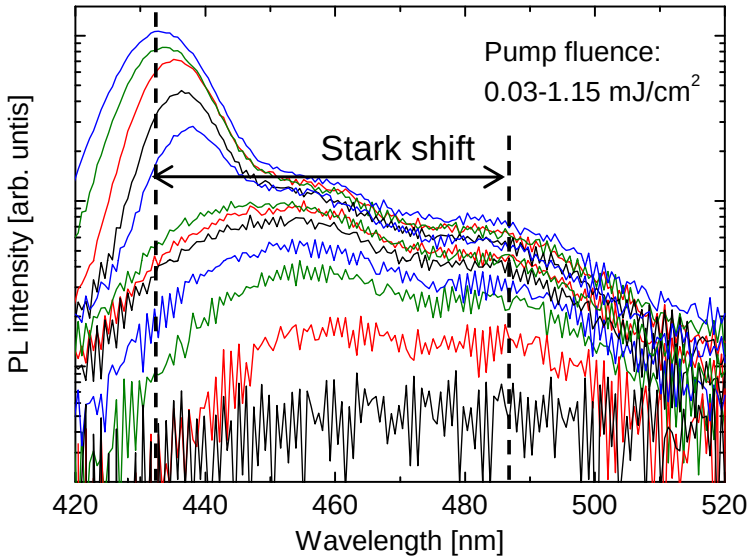

Figure 6.3: Time-integrated photoluminescence from the multiple quantum well with a well thickness of 1.8 nm. Pump fluence in the range 0.03-1.15 mJ/cm^2 were used. The lines indicate the observed Stark shift.

6.3 Experiments

6.3.1 Time-integrated photoluminescence

To show the screening of the built-in piezoelectric field, time-integrated photoluminescence measurements were performed with excitation fluences in the range of 0.03-1.15 mJ/cm^2 on the multiple quantum well with a well thickness of 1.8 nm (Fig. 6.3). We used 400 nm as pump wavelength by frequency doubling the Ti:sapphire amplifier output in a beta-barium borate (BBO) crystal to assure that electron-hole pairs are only generated in the InGaN quantum wells and not in the GaN barriers. The time-integrated photoluminescence from the samples with a quantum well thickness of 2.7 nm and 3.6 nm show similar behavior as shown in Fig. 6.3 and therefore are not shown here. A strong Stark shift is observed between low and high excitation fluences. The saturation of the blue shift for the highest excitation fluences at 432 nm indicates that complete screening of the built-in piezoelectric field takes place. The large shoulder at longer wavelength for the highest excitation fluences is a result of using a time-integrated technique. As carriers recombine the piezoelectric field is restored, which results in a decrease of the transition energy and thus in a red-shift of the photoluminescence spectra.

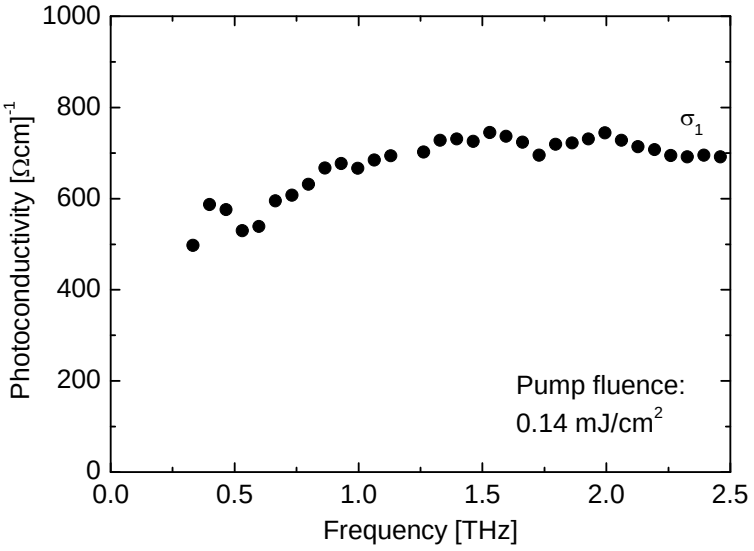

Figure 6.4: Real part of the complex photoconductivity spectrum for the multiple quantum well with a well thickness of 1.8 nm, 5 ps after photoexcitation. The pump fluence was 0.14 mJ/cm^2.

6.3.2 Time-resolved terahertz spectroscopy

The setup for these experiments is in detail described in section 2.4 and shown in Fig. 2.5. Again 400 nm is used as pump wavelength, so with one-photon absorption only electron-hole pairs are generated in the quantum wells. We did not observe any significant influence of two-photon absorption in GaN on our experimental results.

The photoconductivity spectrum measured 5 ps after photoexcitation for the 1.8 nm thick multiple quantum well is shown in Fig. 6.4. A relatively low pump fluence of 0.14 mJ/cm^2 is used, so the built-in piezoelectric field is not completely screened. For the calculation of the photoconductivity from the THz pulses a thickness of the conductive layer of 18 nm was used, which is the combined thickness of the 10 quantum wells. Only the real part of the complex photoconductivity σ_1 is shown. The imaginary part is close to zero, below the noise level, over the whole measured THz bandwidth. An other indication of the very small imaginary part of the photoconductivity is that the phase shift or time difference between the reference and the signal THz pulse is much smaller than the time resolution of the setup. This made it impossible to obtain a reliable measure for the imaginary part of the photoconductivity. The observed increased real part of the conductivity for higher frequencies together with a very small imaginary part differs from the simple Drude conductivity measured in bulk GaAs [26], bulk n-GaN [138], n-GaN films [139]. For n-GaN films also deviations from the Drude conductivity

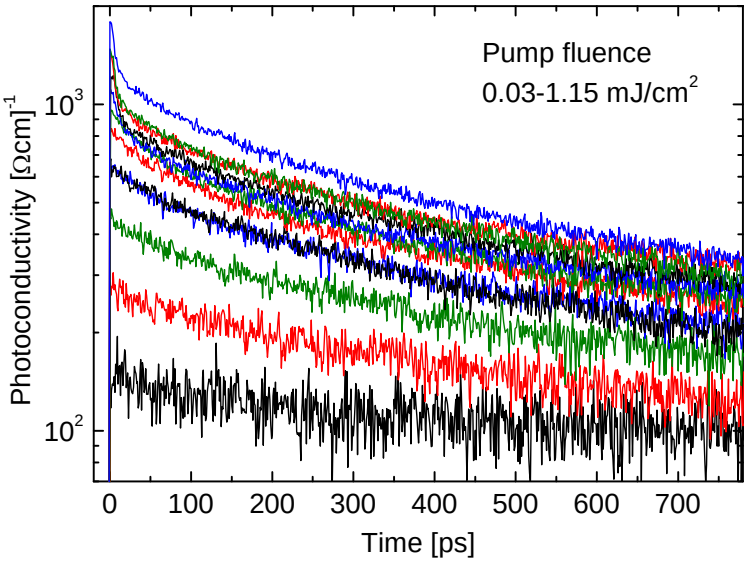

Figure 6.5: Photoconductivity dynamics for the 1.8 nm thick multiple quantum well. Pump fluences in the range 0.03-1.15 mJ/cm^2 were used.

have been reported [140]. We did not observe any significant changes in the shape of the real part of the photoconductivity for longer pump-probe delay times neither if a larger pump fluence was used to completely screen the piezoelectric field.

To measure the photoconductivity decay dynamics only the peak of the THz pulse as function of pump-probe delay time is measured. Again charge carriers are generated by photexcitation with a 400 nm pump. Fig. 6.5 shows the transient photoconductivity in the 1.8 nm thick InGaN/GaN multiple quantum well for the same pump fluences as used in the photoluminescence measurements (Fig. 6.3). For the lowest pump fluence, only a small difference in decay rate between directly after photoexcitation and a few hundreds ps after photoexcitation is observed. For higher pump fluences this differences gets larger and a nonexponential decay of the photoconductivity is observed. An important decay mechanism in InGaN/GaN multiple quantum wells is electron-hole recombination, thereby emitting a photon with an energy equal to the effective transition energy (Fig. 6.2), which depends on the screening of the built-in piezoelectric field. This leads to the strong photoluminescence (Fig. 6.3). The electron-hole recombination rate and hence the photoconductivity decay-rate depends on the overlap of the electron and hole wavefunctions. At early pump-probe delay times and high pump fluences, the complete screening of the built-in piezoelectric field results in a large overlap of the electron and hole wavefunction and hence a large decay rate. At later pump-probe delay times, the carrier density decreases due to electron-hole recombination. This results in the restoration of the

built-in piezoelectric field, which separates the electron and hole wavefunctions in space. This decreases the recombination probability and hence the recombination rate. Because this process is highly dynamical, it result in a nonexponential carrier density decay and hence a nonexponential photoconductivity decay is observed. The 2.7 nm thick and 3.6 nm thick multiple quantum wells show a similar nonexponential decay of the photoconductivity and are therefore not shown here. The same nonexponential decay dynamics are also observed by time-resolved photoluminescence experiments in AlGaN/GaN quantum wells, where the quantum confined Stark effect is also present [135]. The difference in the two techniques is that time-resolved photoluminescence measures how much carrier recombine radiatively while time-resolved THz spectroscopy measures the photoconductivity and thereby is a measure for how much carriers are still left in the conduction band. That these two different techniques give similar result is an indication that the the luminescence intensity and the amount of carriers in the conduction band are strongly related. So radiative recombination is a important decay mechanism for the photoconductivity.

An other important photoconductivity decay mechanism in many semiconductor materials is trapping of charge carriers into a local trap. This process is usually much faster than electron-hole recombination, see e.g. chapter 5. During the growth of InGaN/GaN quantum well small fluctuation in quantum well thickness and composition are inevitable. The variations in quantum well thickness can act as local quantum dots, which can trap charge carriers. The shape of these traps which has an influence on the trapping depends on the local band structure. The local band structure depends on the electric field and thus on the screening. Although we do not have a clear proof that trapping plays a role in the observed photoconductivity dynamics it could be a possible explanation for the very fast decay at earlier times for the highest pump fluences. These decay rates which lay in the 0.1 ps^{-1} range are more typical for trapping in a local trap than for electron hole recombination, see e.g. chapter 5.

The peak photoconductivity as function of pump fluence for all three quantum well thicknesses are shown in Fig. 6.6. A saturation of the peak conductivity for higher fluences is observed. This saturated one-photon absorption is typical for semiconductor nanostructures with a limited density of states [121, 124]. For the highest pump fluences the absorption decreases due to state filling. This effect is stronger than the carrier density dependent absorption coefficient. For high fluences the piezoelectric field is screened, causing a larger overlap in space between the electron and hole wavefunctions, which lead to a larger absorption coefficient. Since this screening is an instantaneous effect it can occur within the duration of the ultrashort pump pulse [120, 128], so that part of the pulse observes a higher absorption coefficient. Although the thickest quantum well had the strongest THz absorption, the absorption occurs in a thicker (36 nm) conducting layer,

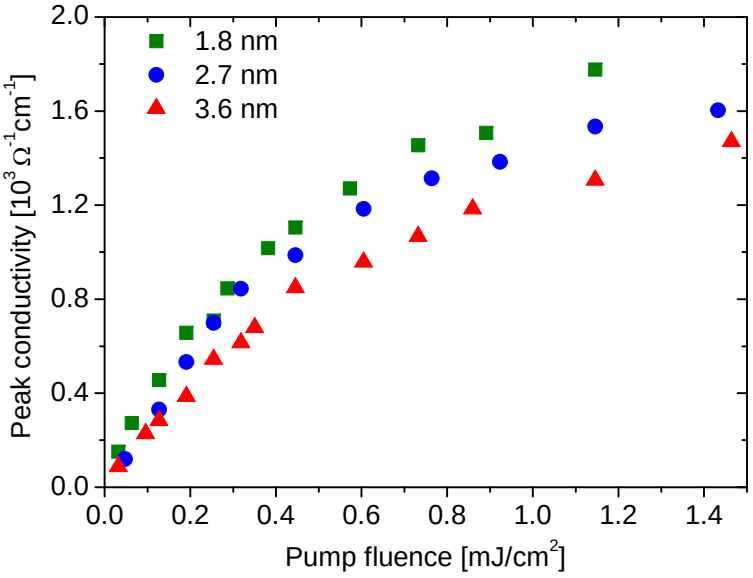

Figure 6.6: Peak of the photoconductivity as function of pump fluence for quantum well thicknesses of 1.8 nm (green squares), 2.7 nm (blue dots) and 3.6 nm (red triangles).

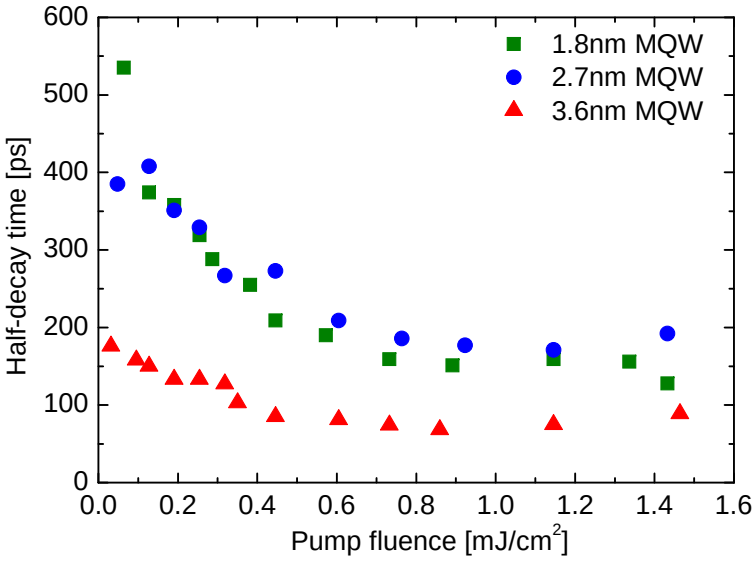

Figure 6.7: Time it takes for the photoconductivity to decay to half the peak value as function of pump fluences for quantum well thicknesses of 1.8 nm (green squares), 2.7 nm (blue dots) and 3.6 nm (red triangles).

resulting in a lower photoconductivity than observed in the 1.8 nm thick multiple quantum well.

To show the dependence of the decay rate on the carrier density, resulting in a nonexponential decay of the photoconductivity, the time it takes for the photoconductivity to decay to half of the peak value as function of pump fluence is shown in Fig. 6.7. For higher pump fluences the half-decay time gets shorter due to the initial faster decay in the screened quantum well. Two saturation effects can play a role in the observed saturation of the decreasing half-decay times for higher pump fluences. First, the increase in the initial photoconductivity saturates due to a lower absorption at higher pump fluences (Fig. 6.6). The second is the saturation in the screening of the piezoelectric field as complete screening is reached. It is not clear why the decay time of the sample with a quantum well thickness of 3.6 nm is significantly faster for all pump fluences.

6.4 Conclusion

A nonexponential carrier density decay is observed in InGaN/GaN multiple quantum wells as a result of the quantum confined Stark effect, caused by the restoration of the built-in piezoelectric field as carriers recombine. The restoration of the built-in piezoelectric field will separate the electron and hole wavefunction and thereby dynamically decrease the recombination probability. This will result in the observed slowing-down decay dynamics. The carrier density dependency of the decay rate is also shown by the decrease in the half-decay time for higher pump fluences. A saturation of this decrease is observed due to a saturation of peak photoconductivity and a saturation of the screening of the piezoelectric field when complete screening is reached. Time-integrated photoluminescence spectra have shown the initial screening of the built-in piezoelectric field. The saturation in the Stark shift shows that complete screening of the piezoelectric field can be reached. The THz pulses are time-resolved to obtain the THz conductivity spectrum, which clearly differs from Drude conductivity.

The quantum confined Stark effect plays an important role in the description of the carrier dynamics in InGaN/GaN quantum wells. However, for a complete understanding of photoconductivity decay dynamics described in this chapter a few questions need to be answered. For understanding the role of carrier trapping on the carrier dynamics, knowhow about the interface morphology is important. This can be obtained which electron microscopy. For obtaining the morphology of the interface of a quantum well a transmission electron microscopy picture of a thin ($\sim$10 nm) slice of the sample is needed. If the average size and density of these fluctuations is known, one can argue if trapping is a reasonable decay path for InGaN/GaN quantum wells. Trapping mechanisms in a InGaN/GaN quantum well gets extra complicated

due to the built-in piezoelectric field. The energy levels in a semiconductor material will change if an electric field is applied. This causes the strong Stark shift observed in the photoluminescence. But this will off-course also change the trapping states and hence the trapping rate.

Chapter 7

Ultrafast conductivity dynamics in black silicon

7.1 Introduction

Black silicon is micro- or nanostructured silicon that better absorbs visible and infrared light than bulk crystalline silicon. The absorption of bulk crystalline silicon is relatively low due to the indirect bandgap of crystalline silicon. This limits the efficiency of silicon based optoelectronic devices [141]. Different solutions to this problem have been developed, like antireflection coatings [142], surface texturing [143], localized surface plasmons on silicon nanoparticles [144], silicon nanowires [36, 145]. Surface texturing will decrease reflection losses and it can trap the light in the material due to total internal reflection. Black silicon belongs to the category of surface texturing. Black silicon was discovered by Jansen *et al.* [146], where they use dry plasma etching to create the textured surface. Later Her *et al.* discovered a different method in producing black silicon [147]. Sharp spikes were created on the silicon surface after irradiation with femtosecond laser pulses. The difference in the black silicon described here is that is produced by using nanosecond laser pulses to change the surface morphology of hydrogenated amorphous silicon (a-Si:H) thin films [148–153]. The advantage of using a-Si:H is that it can be grown on almost any substrate.

The important advantages of black silicon are the decreased Fresnel reflection and the light trapping in the material, which both lead to a higher absorption. A lot of studies concentrated on investigating the fabrication process [146, 147, 153–156] and the optical properties of black silicon [157–162]. However, a study to the dynamical properties of charge carriers in black silicon has to the best of our knowledge not been performed. Knowledge about ultrafast carrier dynamics is important for the fabrication of electrooptic devices out of black silicon like e.g. photodetectors, switches and solar cells [157, 159, 162]. An important question is if after laser anneal-

ing the electronic properties are suitable for devices. For fast optical switches and fast photodetectors a short carrier decay time is required, while for solar cells, the carriers need to be collected to generate a large current, so a short decay time is not an advantage. Instead a large conductivity is important. For all these devices a large material absorption is an advantage which makes black silicon an interesting material to investigate. In this chapter we will describe the ultrafast photoconductivity dynamics of black silicon, produced by laser annealing of a-Si:H films, by time-resolved THz spectroscopy.

Special attention is taken to the influence of copper in black silicon on the ultrafast photoconductivity dynamics. It is known that copper in doped and undoped crystalline silicon will decrease the decay time of photoexcited carriers [163]. So by adding copper to the black silicon we will try to control the carrier lifetime in black silicon and make it shorter, which is an advantage for e.g. optical switches, fast photodiodes, THz generation. An other reason why copper is chosen is its high diffusivity in silicon [164]. The reason why an high diffusivity is needed is because prior to laser annealing the copper and a-Si:H are separate films. A high diffusivity means that the two layers will diffuse into each other faster during the laser annealing.

Earlier, the THz emission from black silicon has been studied by Hoyer *et al.* [165]. We did test our samples for THz emission. The observed THz pulses were very weak and could not compete with any conventual method of THz generation. We decided to not give it further attention and therefore the results are not shown here. However, it could be an interesting spectroscopy technique to learn new properties of black silicon. Depending on which mechanism causes the generation of THz pulses, THz emission spectroscopy can provide information about e.g. surface fields, carrier mobility.

7.2 Samples

An undoped 500 nm a-Si:H film was deposited on a fused silica substrate at 220°C by plasma-enhanced chemical vapour deposition (PECVD) in pure silane gas at a pressure of 100 mTorr, and a flow rate of 75 standard cubic centimeters per minute (sccm) (Fig 7.1(d)). A standard RF source was used at a frequency of 13.56 MHz and at a power of 10 W. Multiple-pulse, spot size 8 mm by 4 mm, 20 ns KrF (248 nm) excimer laser with fluences in the range of 140-436 mJ/cm^2, near to the silicon ablation threshold, was used for irradiation of the amorphous silicon film. The laser beam repetition rate applied in the annealing was 25 or 50 Hz, and the a-Si:H samples were scanned during laser annealing at a speed of 0.5 and 1 mm/s [150]. The output laser beam passed through a specially designed optical system to produce a so-called asymmetrical slope beam profile as illustrated in Fig. 7.1(a). Along the long axis Y of the laser beam pattern, the laser fluence is uniform and has a flat-top beam profile (Fig. 7.1(b)). Along the short axis

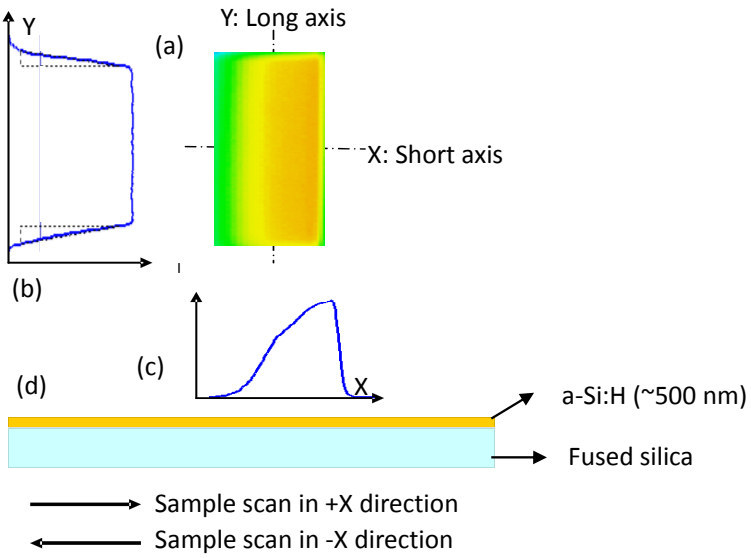

Figure 7.1: (a) Intensity profile of the spatially shaped laser pulses used for the annealing. Where green means low intensity and yellow means high intensity. (b) Cut along the y-axis of (a), showing the flat-top beam profile. (c) Cut along the x-axis of (a), showing the asymmetrical-slope beam profile. (d) Structure of the sample prior to laser annealing.

X, the laser fluence has an asymmetrical-slope beam profile (Fig. 7.1(d)) [151].

During laser annealing part of the amorphous silicon melts due to the irradiation of the laser beam. When it cools down, part of the silicon will crystalize and form microstructures on the surface. A scanning electron microsope (SEM) was used to observe the produced surface morphology. Figure 7.2(a) shows the a-Si:H film prior to the laser annealing. No special features are visible. When the sample was scanned in the positive X direction i.e., with low energy part of the pulse as the leading edge, pillar shaped features are formed on the surface (Fig 7.2(b). These features tend to be blunt and are usually with a round cap on the tip. This method will be referred as method low. The size and density of these features depends on the annealing fluence. Increasing the annealing fluence leads to the growth of larger and more structures. When the samples were scanned in the negative X direction i.e, the high energy part of the pulse as the leading edge, sharp conical features are formed. Fig 7.2(c) shows the typical surface morphology of the a-Si:H films irradiated under the condition that the high energy part of the pulse is leading. This method will be referred as method high. Thermal modeling of the laser processing has also been used to examine the effect of varying the laser fluence and film geometry on the heating, melting and re-solidification of a-Si:H films on glass [152].

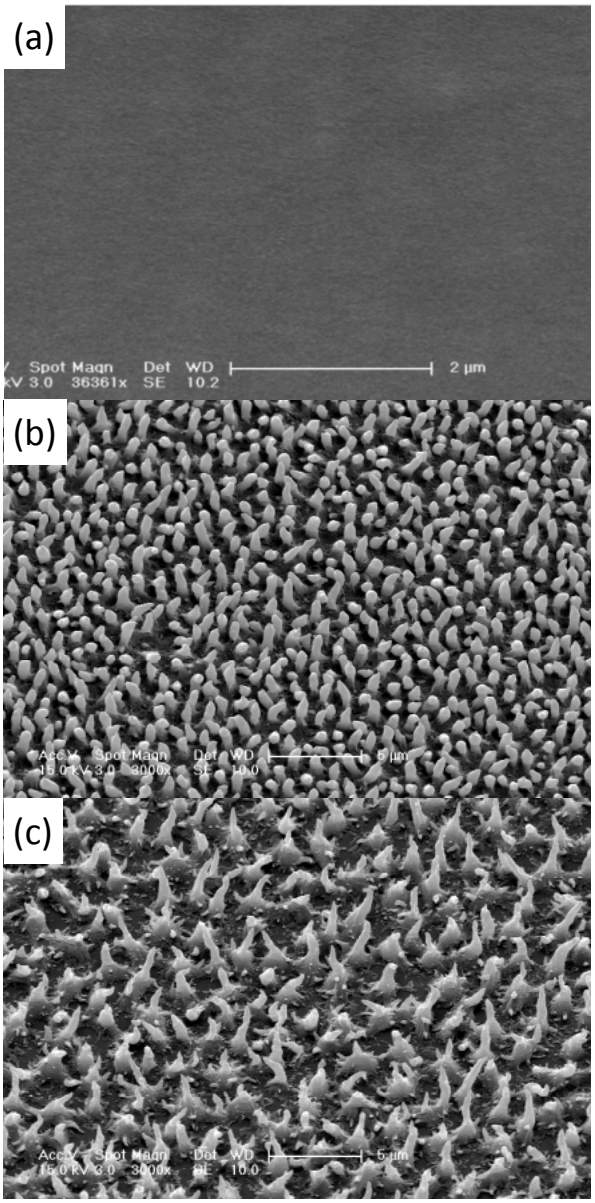

Figure 7.2: (a) Scanning electron microscope (SEM) image of an a-Si:H film. (b) SEM image of black silicon produced by laser annealing of an a-Si:H film, where the sample is scanned through the laser beam so that the low intensity edge of the laser pulse came first (method low). (c) SEM image of black silicon produced by laser annealing of an a-Si:H film, where the sample is scanned through the laser beam so that the high intensity edge of the laser pulse came first (method high).

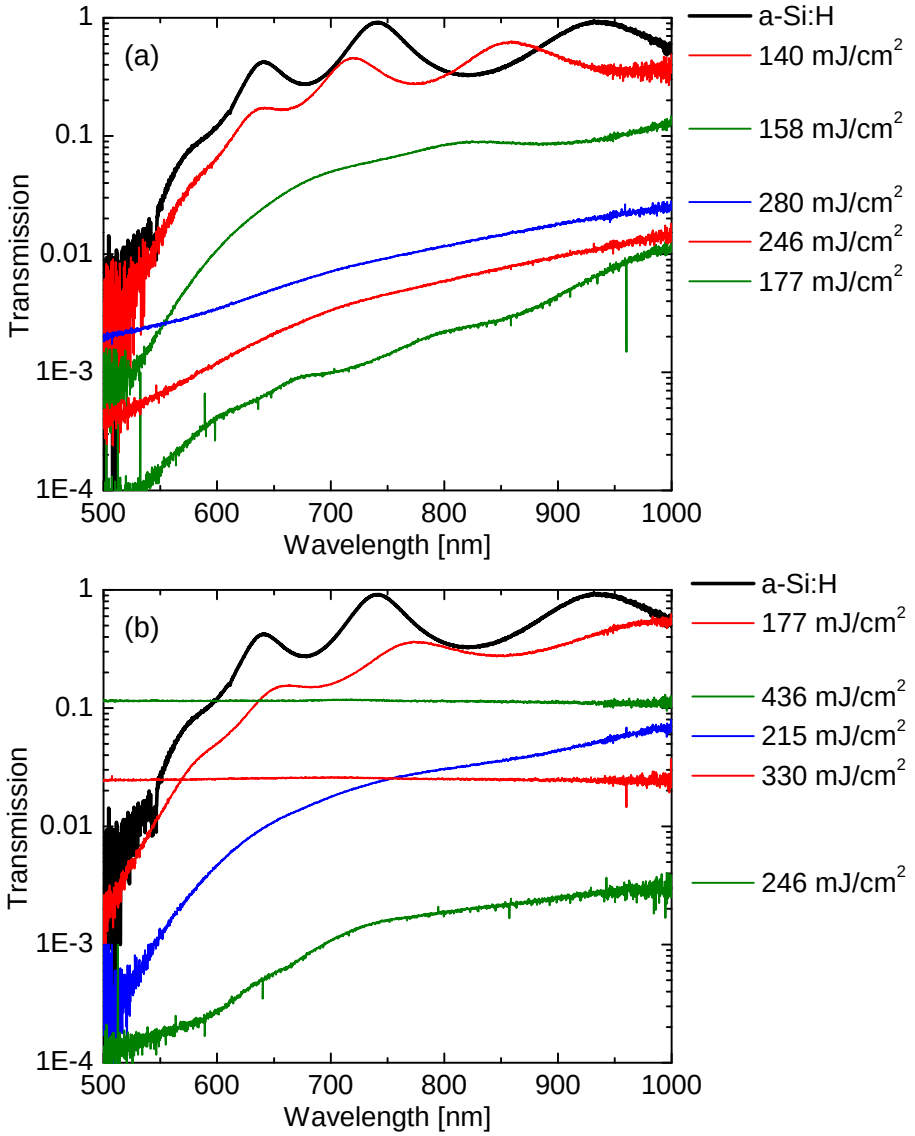

Figure 7.3: (a) Broadband transmission through black silicon, produced with method low with different annealing fluences, for visible and infrared wavelengths. (b) Broadband transmission through black silicon, produced with method high with different annealing fluences, for visible and infrared wavelengths. The black line in both (a) and (b) is the transmission through the untreated a-Si:H film.

After the a-Si:H sample is subjected to laser irradiation under the conditions described above, the surface becomes black. That the samples after annealing appear black indicate that the microstructured surface can effectively trap incident visible light. This is confirmed by measuring the optical transmission at visible and near-infrared wavelength through these black silicon samples. The results are shown in Fig. 7.3(a) and Fig. 7.3(b), where (a) shows the results for the samples produced with method low and (b) for the samples produced with method high. For clarity not all measured transmission spectra are shown. The black line in both Fig. 7.3(a) and Fig. 7.3(b) shows the transmission of the untreated a-Si:H film. The transmission is very high for visible and infrared wavelength (600-1100 nm). The bandgap for amorphous silicon which is hydrogenated increases into the visible range [166]. The oscillations come from the interference between the multiple reflection in the a-Si:H film. Analysis of the positions of the peaks in the interference spectrum confirms the assumed film thickness of ∼500 nm. If the samples are annealed with a low fluence the transmission decreases. For low fluences the interference in the a-Si:H film is still visible. By increasing the annealing fluence, the light transmission through the sample is substantially reduced to less than 1%. The interference also disappears because the transmitted intensity gets too weak to observe multiple reflections. If the annealing fluence is increased even further the transmission increases again. This increase in transmission is attributed to the creation of holes in the material. This also explains the observed constant transmission over all measured wavelengths for high annealing fluences (Fig. 7.3(b)). SEM images confirm the creation of holes. Due to the incorporation of high density impurities during laser annealing, optical absorption below the crystalline silicon bandgap is observed. This phenomena has also been observed for femtosecond laser annealing of crystalline silicon [167].

To get an estimate of the absorption coefficient at 800 nm, which is used as excitation wavelength in the THz spectoscopy experiments, we use a setup shown in Fig. 7.4. The pulses travel through the hole in a paraboloidal mirror like the one used in one of the terahertz spectrometers (Fig. 2.5), before reaching the sample. By placing a power meter in different positions, the transmission through the sample (PM_{trans}), the reflection back through the hole in the mirror (PM_{ref}) and the scattering collected by the paraboloidal mirrors (PM_{scat}) could be measured. For the estimation of the absorption coefficient, uniform scattering is assumed. The absorption coefficient as function of annealing fluence is shown in Fig. 7.5, where the green dots represent the samples produced with method low and the red squares the samples produced with method high. For increasing annealing fluence the absorption increases. For the highest annealing fluences the increase in the absorption coefficient saturates and an absorption coefficient of 80% is estimated. The high scattering coefficient due to the microstructured surface makes an accurate determination of the absorption coefficient by this approach impossible.

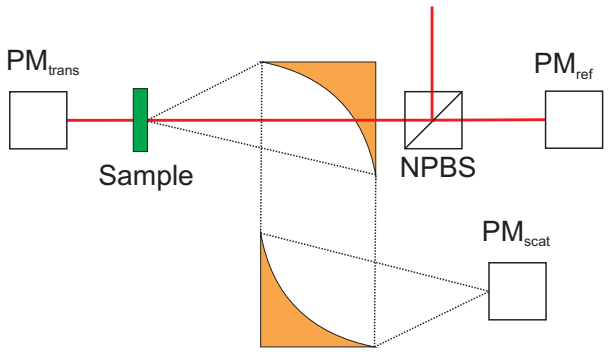

Figure 7.4: Schematic of the setup used to measure the absorption coefficient. NPBS: non-polarizer beam splitter, PM_{trans}: power meter to measure the transmission through the sample, PM_{ref}: power meter to measure the direct reflection from the sample, PM_{scat}: power meter to measure the scattered light.

Other methods like e.g. photothermal deflection spectroscopy could be used to get a more accurate value of the absorption coefficient [168–170].

7.3 Raman spectroscopy

When the a-Si:H film is annealed with ultraviolet laser pulses, part of the material melts and crystallizes during the cooling process. To obtain a measure for the crystalline fraction of the different black silicon samples, Raman spectroscopy is performed. Raman spectroscopy is a tool to study the optical phonon modes in a system [171, 172]. An incident light beam with photon energy $\hbar\omega_{photon}$ will be scattered from a system. Besides the elastic Rayleigh scattering which does not change the frequency of the scattered light, the light can also be inelastically scattered by interactions with molecular vibrations. The system will be in a different vibrational state after scattering, thereby giving (Anti-Stokes: $E_{scattered} = \hbar\omega_{photon} + \hbar\omega_{phonon}$) or taking (Stokes $E_{scattered} = \hbar\omega_{photon} - \hbar\omega_{phonon}$) energy from the photon. Thus the frequency of the scattered photon is shifted. This Raman-shift can be measured and is sensitive to which molecular bond is vibrating. The Si-Si vibrations in crystalline silicon will give rise to a sharp peak in the measured Raman spectra, while the Si-Si bond in amorphous silicon will give a broad peak in the Raman spectra due to the large variations in bond lengths and orientations. This means that Raman spectroscopy is able to distinguish between crystalline and amorphous silicon. The relative strength of the measured Raman shifts is a measure for the crystallinity of the sample [173–176].

For the Raman measurements a Renishaw 2000 Raman microscope was

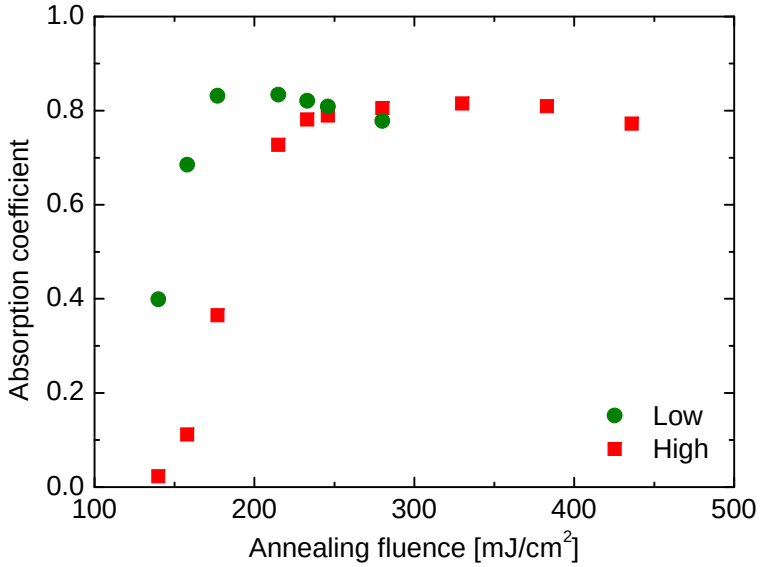

Figure 7.5: Absorption coefficient of black silicon at 800 nm for different annealing fluence. The green dots and red squares represent the samples produces with method low and method high respectively.

used. The excitation wavelength was 782 nm. Fig. 7.6(a) and Fig. 7.6(b) show the normalized Raman spectra for the samples produced with method low and method high respectively. Annealing fluences between 140 and 280 mJ/cm^2 were used to produce the samples. The broad peak around 480 cm^{-1} is caused by the vibrations of the Si-Si bonds in amorphous silicon. The sharp peak around 518 cm^{-1} is caused by the vibrations of the Si-Si bonds in crystalline silicon. By deconvoluting the two peaks and determine their relative strength including the relative Raman cross sections, the crystallinity of the samples can be obtained (Fig. 7.7). As can be seen, the crystallinity increases for higher annealing fluences for both production methods. When higher annealing fluences are used more of the material will melt and crystallize. For the samples produced with method low a higher crystallinity is measured. It is necessary to be cautious in making conclusions about the absolute value of the crystallinity. Firstly, when higher annealing fluences are used, the absorption increases (Fig. 7.5) which means that the penetration depth d of the 782 nm excitation beam decreases and possibly gets shorter than the sample thickness. In this case the measured crystallinity will not represent the crystallinity of the whole sample but only of the top layer of thickness d. An other uncertainty is in the Raman cross sections. This value depends on the average crystalline grain size [177, 178], which is not taking into account in the presented crystallinity.

It can be seen from Fig. 7.6, that the Raman shift of the crystalline

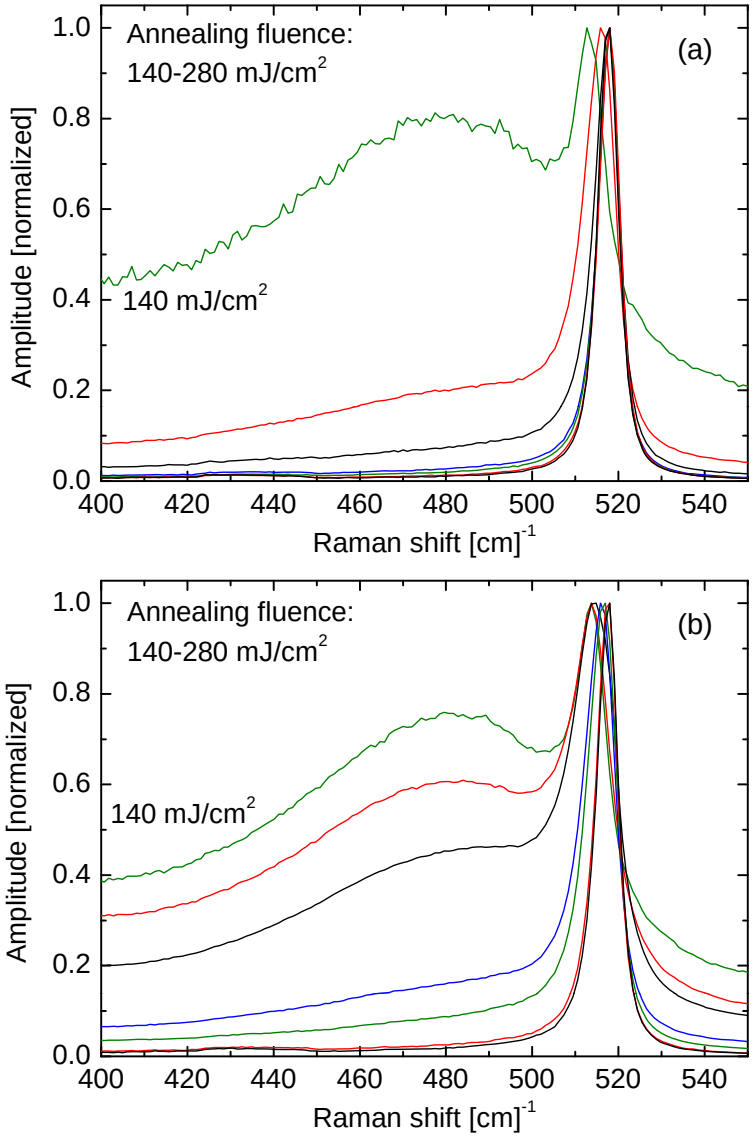

Figure 7.6: (a) Raman-spectra for the samples produced with method low with an annealing fluence in the range 140-280 mJ/cm^2. (b) Raman-spectra for the samples produced with method high with an annealing fluence in the range 140-280 mJ/cm^2.

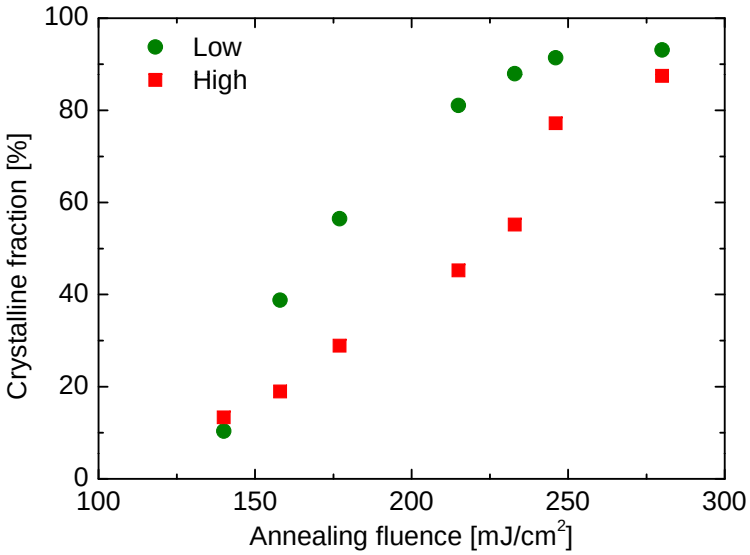

Figure 7.7: Crystalline fraction of black silicon as function of annealing fluence obtained from the Raman spectra (Fig. 7.6). The green dots represent the samples produced with method low and the red squares the samples produced with method high.

peak changes when a different annealing fluence is used. Fig. 7.8 shows the Raman shift of crystalline silicon as function of the annealing fluence for both production methods, where the green dots represent method low and the red squares method high. A larger Raman shift for crystalline silicon at higher annealing fluences is observed for both methods. Usually a change in the Raman shift is explained by a different nature and level of stress in laser processed films [173, 179, 180]. An increase in wave number is observed with compressive stress and a decrease with tensile stress. Stress in a material will have an effect on the electron mobility [102, 181]. However, other explanations for the change in the Raman shift are possible. A change in the crystalline grain size will also change the Raman shift due a phonon confinement effect [182, 183].

7.4 Time-resolved terahertz spectroscopy

For the time-resolved terahertz spectroscopy measurements, the setup shown in Fig. 2.6 is used. The transmission of the teraherz pulses through optically excited black silicon were measured to obtain the photoconductivity spectra as described in chapter 4. As excitation wavelength 800 nm was used, which is absorbed in the annealed samples but not in an untreated a-Si:H film and neither in the fused silica substrate. The photoconductivity spectra for the

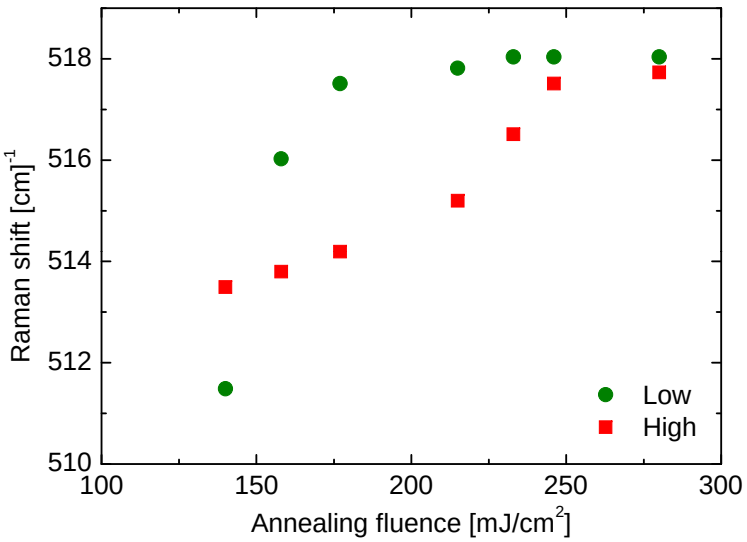

Figure 7.8: Raman shift of the crystalline silicon in the black silicon samples as function of annealing fluence. The green dots represent the samples produced with method low and the red squares the samples produced with method high.

sample prepared with method low with an annealing fluence of 215 mJ/cm^2 are shown in Fig. 7.9(a) and for the sample prepared with method high with an annealing fluence of 280 mJ/cm^2 in Fig. 7.9(b). Different pump-probe delay times of 5, 10, 20, 50 and 150 ps were used to observe the effects of various dynamical processes on the photoconductivity. The pump fluence was 0.88 mJ/cm^2. The real part of the photoconductivity has a non-zero DC-conductivity and increases slowly with frequency, a similar conductivity spectrum has been observed in a-SiGe:H [184], nano crystalline silicon [47], and micro crystalline silicon [176]. The imaginary part of the photoconductivity is negative and decreases with frequency. This conductivity spectrum shows a clearly distinguished behavior from Drude conductivity observed in e.g. GaAs [26] and shown in Fig. 4.4. The shape of the conductivity spectra does not change significantly as function of pump-probe delay time. Only the amplitude decreases for larger pump-probe delay times, which is an indication that the main contribution to the photoconductivity dynamics is the change in the carrier density. Also the production method does not have a significantly influence on the shape of the photoconductivity spectra. The change in amplitude between the two samples cannot completely be described by a difference in absorption and hence in carrier density, see Fig. 7.5. This means that there are differences in the mobility of the carriers between the different samples. The smaller imaginary part compare to the

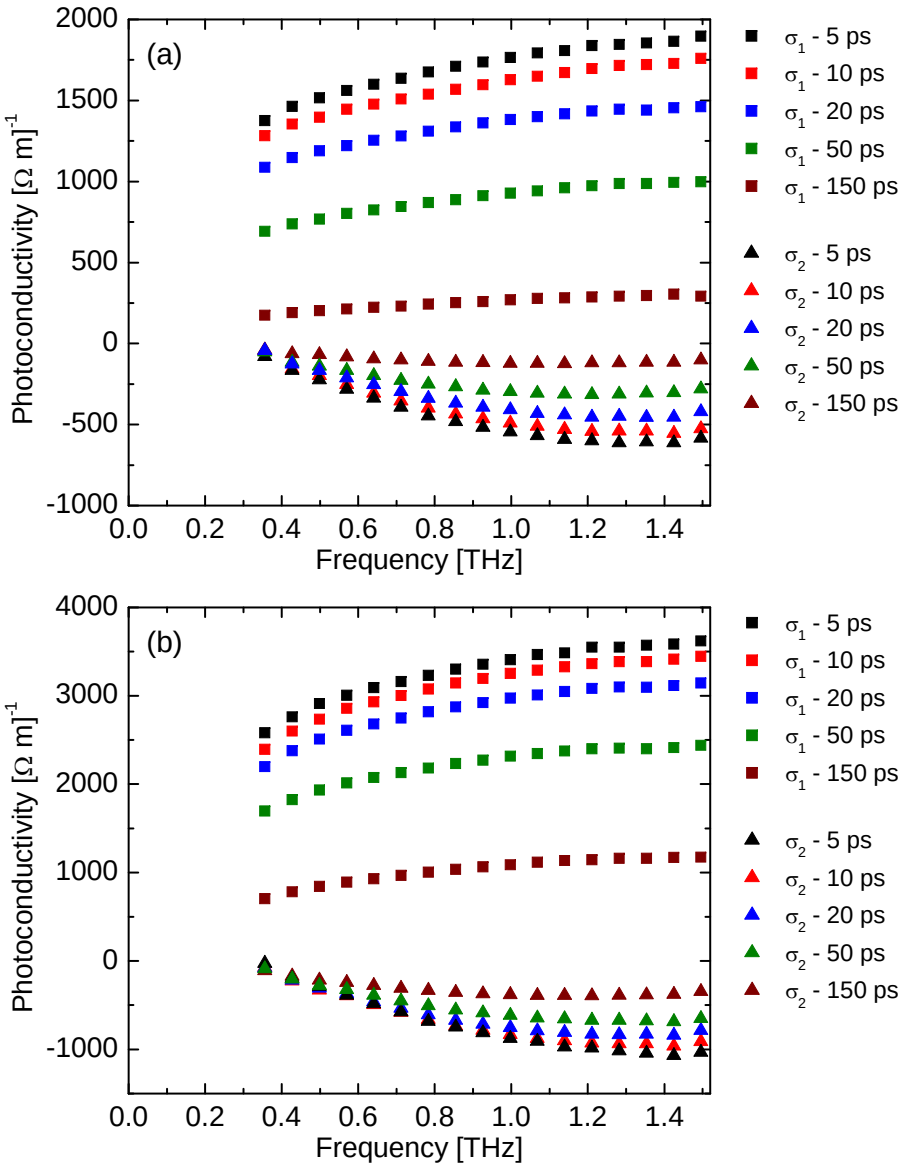

Figure 7.9: (a) Photoconductivity spectra of black silicon at various pump-probe delay-times, produced with method low with an annealing fluence of 215 mJ/cm^2. (b) Photoconductivity spectra of black silicon at various pump-probe delay-times, produced with method high with an annealing fluence of 280 mJ/cm^2. A pump fluence of 0.88 mJ/cm^2 was used for both samples.

real part of the conductivity validates the use of 1D-spectroscopy, which will be described in the rest of this chapter.

Firstly, we will investigate the influence of the pump intensity and hence the carrier density on the photoconductivity dynamics in black silicon. The same two samples as for measuring the photoconductivity spectra were used, i.e. method low with an annealing fluence of 215 mJ/cm^2 and method high with an annealing fluence of 280 mJ/cm^2. Only the peak of the THz pulse as function of pump-probe delay time was measured and the results are shown in Fig. 7.10. For the sample produced with method low with an annealing fluence of 215 mJ/cm^2, pump fluences in the range of 0.0092-1.4 mJ/cm^2 were used (Fig. 7.10(a)) and for the sample produced with method high with an annealing fluence of 280 mJ/cm^2, pump fluences in the range of 0.0046-1.3 mJ/cm^2 were used (Fig. 7.10(b)). When the samples were excited with a low pump fluence the near-instantaneous rise of the photoconductivity is followed by first a fast decay and then a slower decay. The rise time is limited by the time resolution of the setup. The initial fast decay component of the photoconductivity disappears when the pump fluence is increased and a near-single exponential decay of the photoconductivity is observed for the highest pump fluences.

The peak conductivity obtained from the traces shown in Fig 7.10 as function of pump fluences are shown in Fig. 7.11, where the green dots are for the traces from Fig. 7.10(a) (method low) and the red squares for the traces from Fig. 7.10(b) (method high). The dependence of the peak photoconductivity on the pump fluence is linear, indicating non-saturable single photon absorption. The difference in slope between the two samples is like for the photoconductivity spectra caused by a different absorption and mobility.

To describe the change in photoconductivity dynamics as function of pump fluence, the traces shown in Fig. 7.10 are fitted with a bi-exponential decay function. The fast decay time constant as function of pump fluence is shown in Fig. 7.12(a). The green dots represent sample low - 215 mJ/cm^2 and the red squares sample high - 280 mJ/cm^2. In the regime of low fluences, left of the dotted lines in the Fig. 7.12(a), the fast component of the decay time increases with pump fluence, indicating the saturation of a trap state. The color of the lines is used to distinguish between the two samples. Trapping of charge carriers lead to a decrease of the photoconductivity, because carriers in a local trap are not mobile and therefore will not longer contribute to the conductivity. Trapping is usually much faster than electron-hole recombination. When more and more traps get occupied the probability that an electron will be trapped will go down, which results in a slower decay of the photoconductivity. The dotted line in Fig. 7.12(a) indicates the point where the photoconductivity traces could no longer be fitted with a bi-exponential function. This point depends on the method and annealing fluence used in the production process. The decay time constants

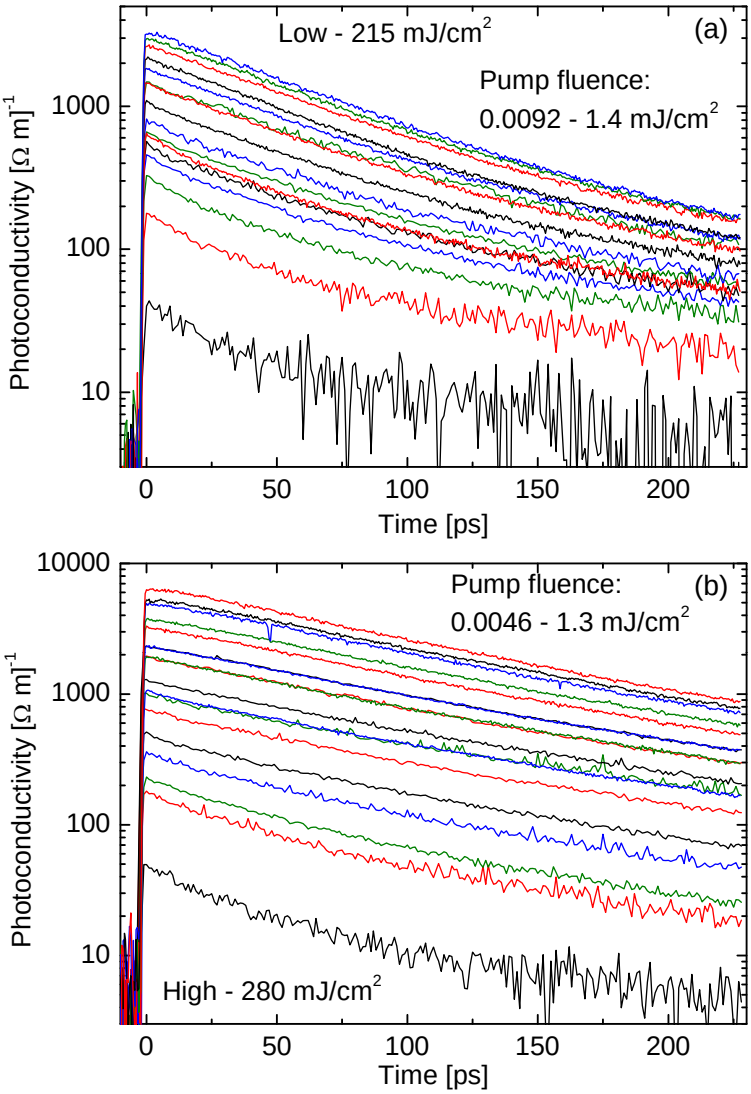

Figure 7.10: (a) Photoconductivity dynamics for the sample produced with method low with an annealing fluence of 215 mJ/cm^2. Pump fluences in the range of 0.0092-1.4 mJ/cm^2 were used. (b) Photoconductivity dynamics for the sample produced with method high with an annealing fluence of 280 mJ/cm^2. Pump fluences in the range of 0.0046-1.3 mJ/cm^2 were used.

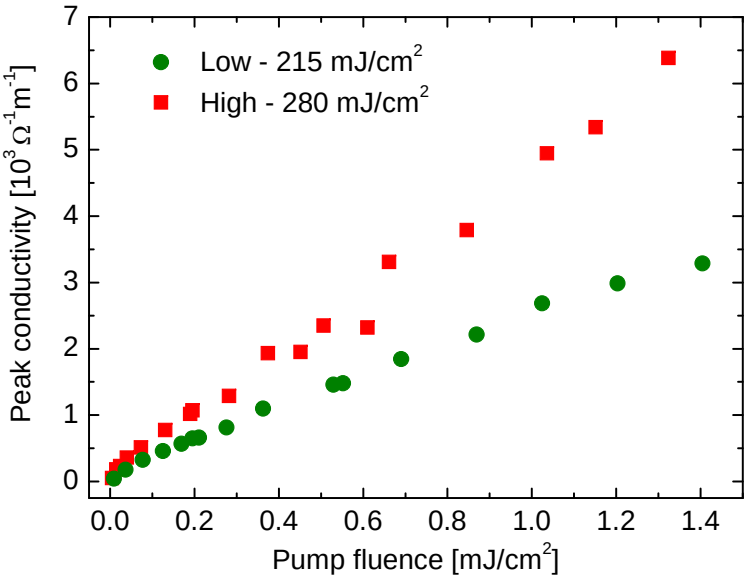

Figure 7.11: Peak photoconductivity as function of pump fluence, where the green dots are for the sample produced with method low - 215 mJ/cm^2 and the red squares for method high - 280 mJ/cm^2.

shown on the right of these lines are the single exponential decay time constants. This time does not significantly change as function of pump fluence. However, the observed decay times of ∼60 ps for sample low - 215 mJ/cm^2 and ∼110 ps for sample high - 280 mJ/cm^2 cannot be the electron-hole combination in crystalline silicon, which takes due to the indirect bandgap much longer.

The slow decay component of the photoconductivity dynamics is shown in Fig. 7.12(b). The slow decay component is only plotted for the traces that could be fitted with a bi-exponential function, i.e. left of the dotted lines in Fig. 7.12(a). The slow decay time constant does not change significantly as function of pump fluence. The reason for the large uncertainty in the slow decay time at higher pump fluences is because the decay approaches a single exponential decay, which will give a larger error in one of the decay time constants of the bi-exponential decay.

For the measurements on the different samples produced with different annealing fluences, a relatively high pump fluence of 1.3 mJ/cm^2 is used. This means that the traps causing fast decay component are saturated for most samples. The result are shown in Fig. 7.13, where in Fig. 7.13(a) the result for the samples produced with method low and in Fig. 7.13(b), the samples produced with method high are shown. After the fast rise a slower near single exponential decay is observed. There are slight deviations from the single exponential decay behavior for the lowest annealing fluences,

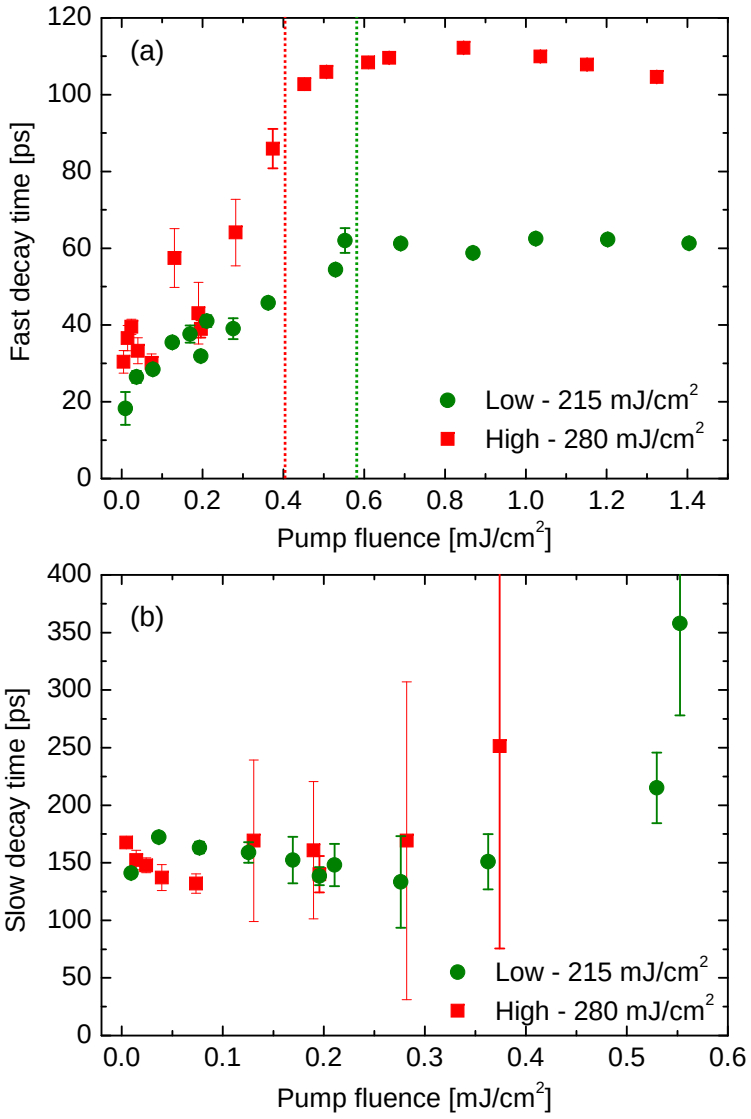

Figure 7.12: (a) Fast decay time constant as function of pump fluence obtained from bi-exponential fits of the traces shown in Fig. 7.10. The green dots are for the sample produced with method low - 215 mJ/cm^2 and the red squares for method high - 280 mJ/cm^2. The dashed vertical lines indicate the point where the decay dynamics changes from bi-exponential to single exponential decay. (b) Slow decay time constant as function of pump fluence.

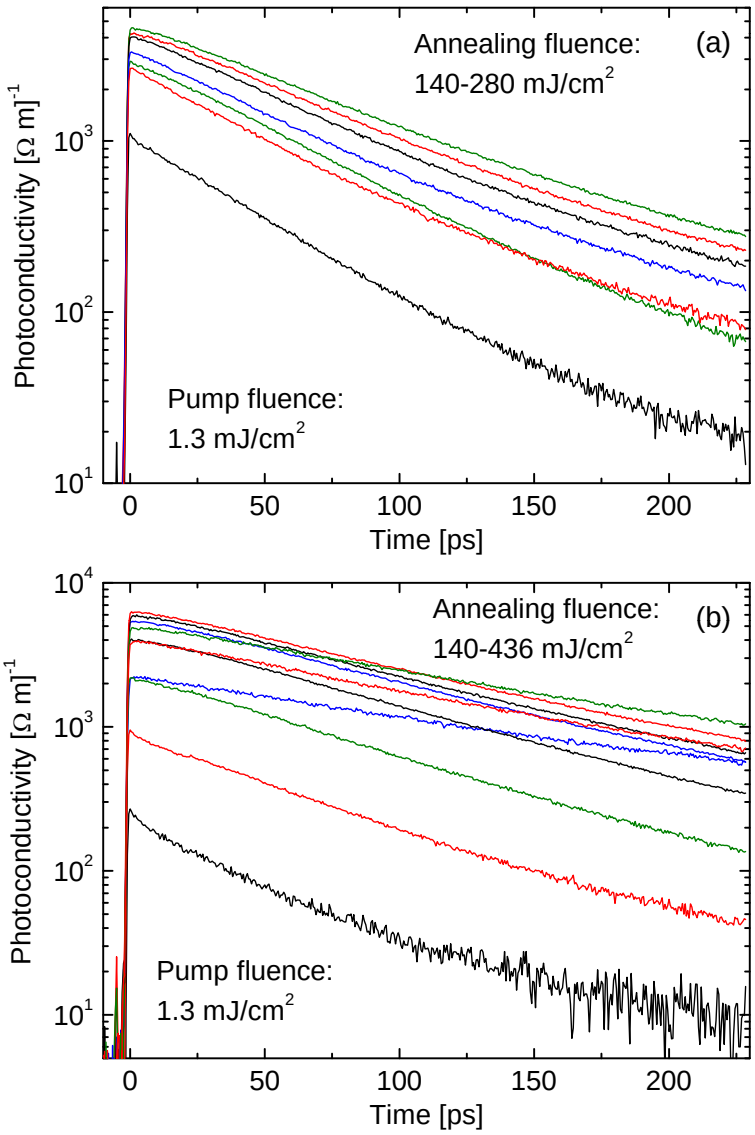

Figure 7.13: (a) Photoconductivity dynamics of black silicon produced with method low with annealing fluences in the range 140-280 mJ/cm^2. (b) Photoconductivity dynamics of black silicon produced with method high with annealing fluences in the range 140-436 mJ/cm^2. The carriers were excited with a pump fluence of 1.3 mJ/cm^2.

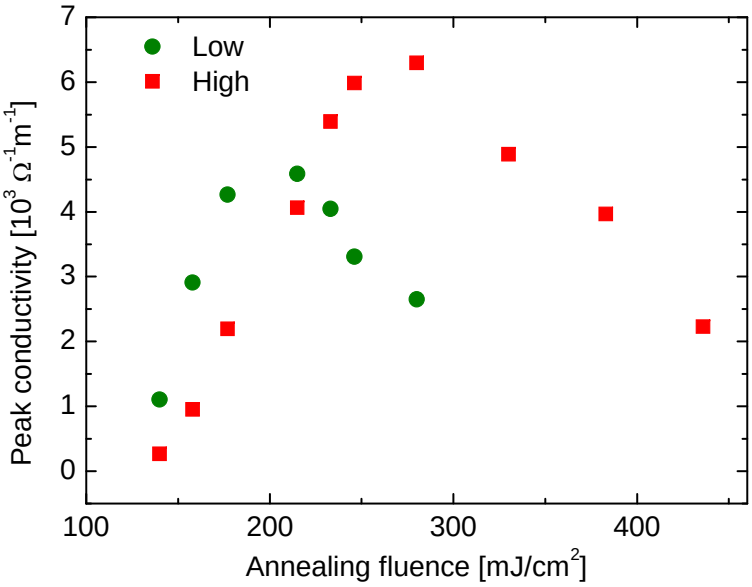

Figure 7.14: Peak photoconductivity as function of annealing fluence, where the green dots represent the samples produced with method low and the red squares the samples produced with method high.

where still a fast decay component is visible at a pump fluence of 1.3 mJ/cm^2. What directly can be observed is that the amplitude and decay time of the photoconductivity depends strongly on the sample structure. The amplitude of the obtained photoconductivity traces is relatively low compared with e.g. the photoconductivity in bulk crystalline silicon. This usually means that the carrier mobility is relatively low. Smaller carrier mobilities are also observed in microcrystalline silicon 70 cm^2/Vs) [176]. Furthermore, the non-Drude conductivity behavior can also lead to a lower frequency average photoconductivity.

To have a closer look at the influence of the laser annealing on the photoconductivity, we plotted the peak photoconductivity for the different samples (Fig. 7.14), where the green dots represent method low and the red squares method high. First an increase in the peak photoconductivity for increasing annealing fluence is observed. For method low the maximum is reach for the sample produced with an annealing fluence of 215 mJ/cm^2. For even higher annealing fluences the peak conductivity decreases. For method high, the sample produced with an annealing fluence of 280 mJ/cm^2 has the highest peak photoconductivity. If higher annealing fluence were used also for method high the peak photoconductivity drops. This behavior can partly be explained by the change in absorption of the 800 nm pump (Fig. 7.5). For low annealing fluences the absorption coefficient follows the same trend as the peak photoconductivity. However, for the highest annealing fluences the

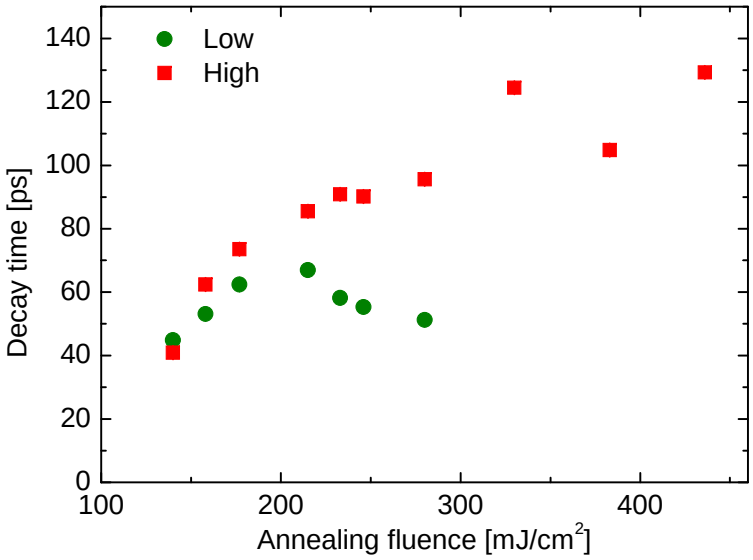

Figure 7.15: Decay time of the photoconductivity obtained from single exponential fits to the traces shown in Fig. 7.13 as function of annealing fluence. The green dots represent the samples produced with method low and the red squares the samples produced with method high.

absorption does not drop as much as the photoconductivity. This means that not only the absorption but also the mobility of the charge carriers depends on the used annealing fluences. The drop in the peak photoconductivity goes coincide with the fluence where the annealing starts to damage the material and makes holes in the a-Si:H film.

The traces of Fig. 7.13 are fitted with a single exponential decay function. For obtaining good fits it was necessary to add a constant to the exponential function. This indicates that part of the photoconductivity does not decay or decays at timescale much longer than the measuring time window of 230 ps. This is typical for electron-hole recombination in crystalline silicon. The decay time obtained from the fits are shown in Fig. 7.15, where the green dots represent method low and the red squares method high. For the samples produced with method low, first an increase of the decay time for increasing annealing fluence is observed. The slowest decay is observed for the sample with an annealing fluence of 215 mJ/cm^2. For higher annealing fluences the decay time decreases again. Photoconductivity decay times between 45 and 67 ps can be achieved with method low. For the samples produced with method high, the decay time keeps increasing for increasing annealing fluence. However, the increase in decay time saturates for the highest annealing fluences. Photoconductivity decay times between 41 and 129 ps can be achieved with method high.

A possible explanation for the increase in decay time is the crystallization

of the a-Si:H during laser annealing (Fig. 7.7). In an amorphous structure more traps are present, which leads to a faster decay [103, 185, 186]. For method low the crystallization saturates at high annealing fluences (Fig. 7.7) and using high annealing fluence causes also the creation of more traps in the form of dangling bonds and oxygen incorporations [153]. For method high the crystallization does not saturate (Fig. 7.7). Here, the creation of more traps which will decrease the decay time is not able to completely compensate the effect that increases the decay time.

An other effect that can influence the decay time is stress in the film, which can be observed by the change in the Raman shift (Fig. 7.8) [173, 179, 180]. However, this change in the Raman shift can also be caused by a change in the size of the crystalline grains, due to a phonon confinement effect [182, 183, 187]. Since the shift in the Raman peak saturates for higher annealing fluence, stress cannot explain the decrease in decay time for higher fluence in the samples produced with method low. For lower fluences, the shift in the Raman peak is larger, which could mean a large change in the stress of the material and hence could result in a decrease of the decay time. Since no decrease in decay time for increasing annealing fluences is observed at low annealing fluences, we speculate that the stress in the material does not have a significant influence on the decay time.

7.5 Effects of copper

Decay times in the range of 40-130 ps is a lot shorter than the electron-hole recombination time in bulk crystalline silicon. However, for many application like optical switches, fast photodiodes, THz generation even shorter decay times are required. Short decay times have been observed in radiation damage silicon [102, 103] microcrystalline silicon [188] and nanocrystalline silicon [176]. A common method for decreasing the decay time is introducing extra traps. To achieve that, copper is included in the black silicon material. An advantage of using copper is the high diffusivity of copper in silicon. The samples are produced in a similar way as described in section 7.2. The difference is that on top of the a-Si:H film (Fig. 7.1) a 10 nm copper layer is deposited. The samples are annealed with the same pulse shapes as described in section 7.2, with both method low and method high.

To investigate what happens with the copper layer during laser annealing, scanning electron microscopy (SEM) in combination with energy-dispersive X-ray spectroscopy (EDS) is used [189]. The electron beam is generated by a thermionic emission from a tungsten filament. The electrons are accelerated with a relatively low acceleration voltage of 5 kV to avoid a large penetration of the electrons into the fused silica substrate. The backscattered electrons from the sample were detected by a solid state backscattered electron, large field, CCD camera. In addition an "Oxford Instruments" 50 mm^2 X-max

silicon drift detector was used for the EDS measurements. When an electron collide with an atom it can, providing that the electron has enough energy to overcome the binding energy of the electrons in the atom, ionize the atom. The binding energy of the electrons in an atom depends on the Z-number, which is the number of particles in the nucleus and on the electron shell. For a lighter atom, which means a lower Z-number the binding energy of the electrons is lower. The lowest shell, the K-shell has the highest binding energy, followed by the L-shell, M-shell etc. When a electron is removed from one of the shells, a vacancy is created. This vacancy will be filled by the decay of one of the other electrons from a higher shell, thereby emitting a photon. The most likely transition and thereby the strongest photon signal is the Kα-line. This is the electron transition from L(2p) to K(1s), where the L, K stands for the shell and the 2p, 1s stands for a subshell defining the azimuthal quantum number l: s means l=0 and p means l=1. Quantum mechanical transition rules forbids the transition between L(2s) and K(1s). The emitted photons from the Kα transitions lay in the X-ray regime of the electromagnetic spectrum, except for hydrogen and helium, where the binding energy is much lower. For hydrogen and helium the Kα lines lay in the ultra-violet and can therefore not be detected with EDS. Because every atom has a different transition energy, it is possible to measure which elements are present in a material by analyzing the energy of the emitted X-ray photons. By using an acceleration voltage of 5 kV, only electrons with a binding energy of 5 keV and lower can be removed from the atom. The binding energy of the K-shell electrons in silicon is 1839 eV and in copper 8979 eV [190]. This means that for copper the strong Kα cannot be measured. However, it is still possible to detect the weaker Lα line, which is the transition from M(3p) to L(2s). The binding energy for L-shell electrons in copper is 1096.7 eV [190].

A SEM picture of the sample produced with method low with an annealing fluence of 233 mJ/cm^2 is shown in Fig. 7.16(a). Most of the features on the surface have a nice rounded shape like in the case of black silicon without copper (Fig. 7.2(b)). Also one large irregular shaped feature is visible. By using EDS, the different elements present in the material are detected (Fig 7.16(b)). Except silicon and copper also oxygen and carbon were detected. The hydrogen present in the amorphous silicon cannot be detected with EDS. For every element the concentration was measured and mapped over the same area as Fig. 7.16(a). Fig. 7.16(c) shows the map of the silicon concentration. A higher silicon concentration, almost pure silicon, outside the structures was measured. This does not mean that there is more silicon present outside the structures. The concentration in the structure is lower because there are other elements present. Note that this method cannot distinguish between amorphous and crystalline silicon. Fig. 7.16(d) shows the map of the copper concentration. After annealing, the copper does not longer form a uniform film but is mainly present at the structures. A higher copper

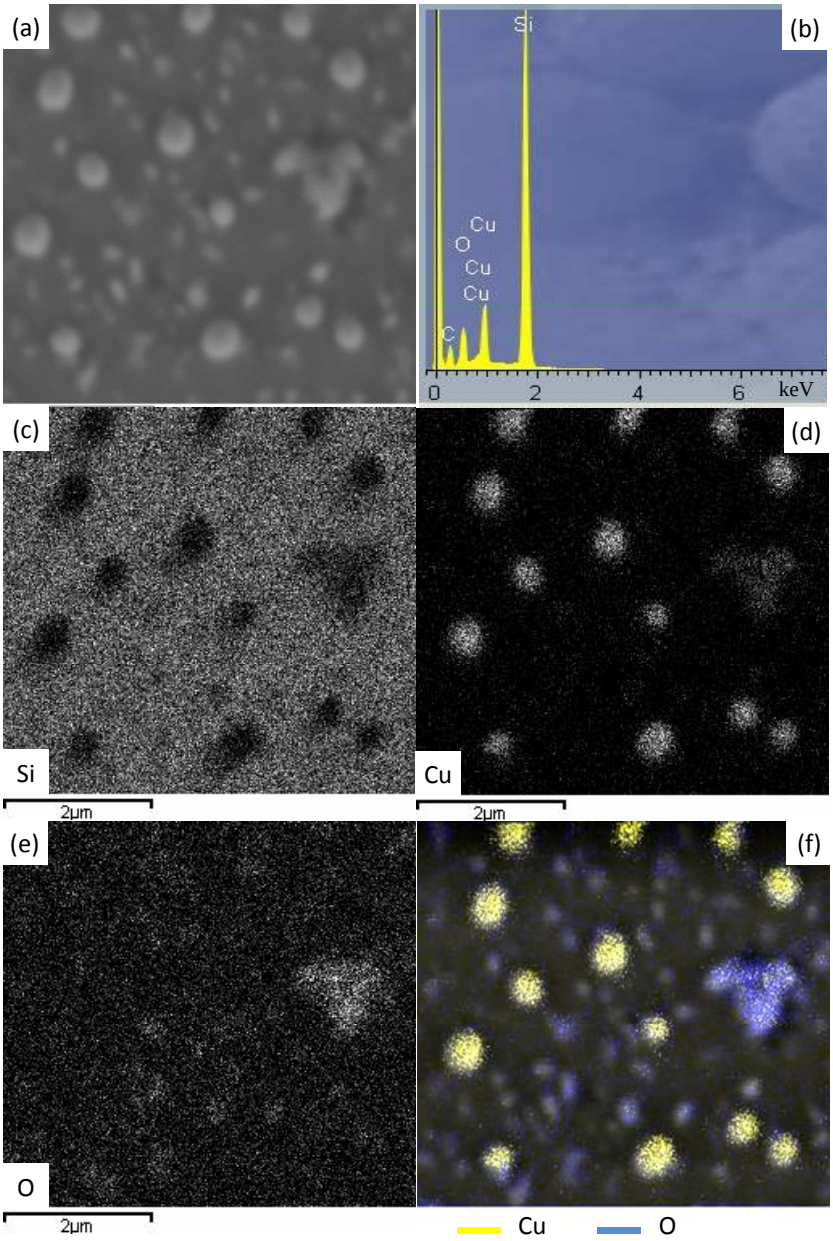

Figure 7.16: Scanning electron microscope (SEM) picture of black silicon including copper produced with method low with a annealing fluence of 233 mJ/cm^2. (b) Sum spectra over the whole area visible in (a), obtained with energy-dispersive x-ray spectroscopy (EDS). (c) Map of the silicon concentration of the same area as shown in (a). (d) Map of the copper concentration. (e) Map of the oxygen concentration. (f) Combination of (d) and (e) where the copper concentration is shown in yellow and the oxygen concentration is shown in blue.

concentration in the nice rounded shaped structures is observed compare to the irregular shaped structure. It is not possible from these measurement to see in what form the copper is present at the microstructures (e.g. thin film on the surface of the structure, nanoclusters inside the structure, uniform distribution). Fig. 7.16(e) shows the map for the oxygen concentration. A higher oxygen concentration is observed in the irregular shaped structure. One can speculate that the present of oxygen during the growth has an important influence on the shape of the structures. The map for carbon was uniform and not shown here. Fig. 7.16(f) is a combination of Fig. 7.16(d) and Fig. 7.16(e), where a color code is used to distinguish between copper (yellow) and oxygen (blue).

Optical pump-terahertz probe measurements are performed on the black silicon samples containing copper produced with different annealing fluences. The carriers were excited with a pump wavelength of 800 nm and a fluence of 1.9 mJ/cm^2. The samples produced with method low with annealing fluences in the range 140-383 mJ/cm^2 are shown in Fig. 7.17(a) and the samples produced with method high with annealing fluences in the range 140-383 mJ/cm^2 are shown in Fig. 7.17(b). The peak at 22 ps is caused by a reflection of the pump beam. Immediately two differences from the photoconductivity dynamics of black silicon without copper (Fig. 7.13) are visible. Firstly, the decay is no longer near-single exponential. A relatively high annealing fluence of 1.9 mJ/cm^2 is used, so it cannot come from the same trap which caused the observed fast component in the photoconductivity dynamics in black silicon without copper when a low pump fluence was used. This means that the copper introduces extra traps, which creates an alternative decay path for the charge carriers. The second difference is that the decay is much faster than for black silicon without copper.

The peak photoconductivity for the black silicon samples with copper is shown in Fig. 7.18. The copper does not seem to have a noticeable effect on the peak conductivity. The values are of the same order as for the samples without copper (Fig. 7.14). Differences in the absorption coefficient between the different samples can again explain for a large part the observed differences in the peak photoconductivity. Although not completely, so the mobility of the electrons in not the same for all the samples. It is not clear why the sample produced with method high - 246 mJ/cm^2 has a much higher peak photoconductivity than the other samples.

The decay of the photoconductivity traces (Fig. 7.17) are fitted with bi-exponential decay functions. The obtained decay time constants are plotted in Fig. 7.19, where (a) shows the fast decay time constant as function of annealing fluence and (b) shows the slow decay time constant as function of annealing fluence. In both figures the green dots represent the samples produced with method low and the red squares the samples produced with method high. For the fast component of the photoconductivity decay dynamics (Fig. 7.17), decay times between 1.8 and 7.5 ps have been observed.

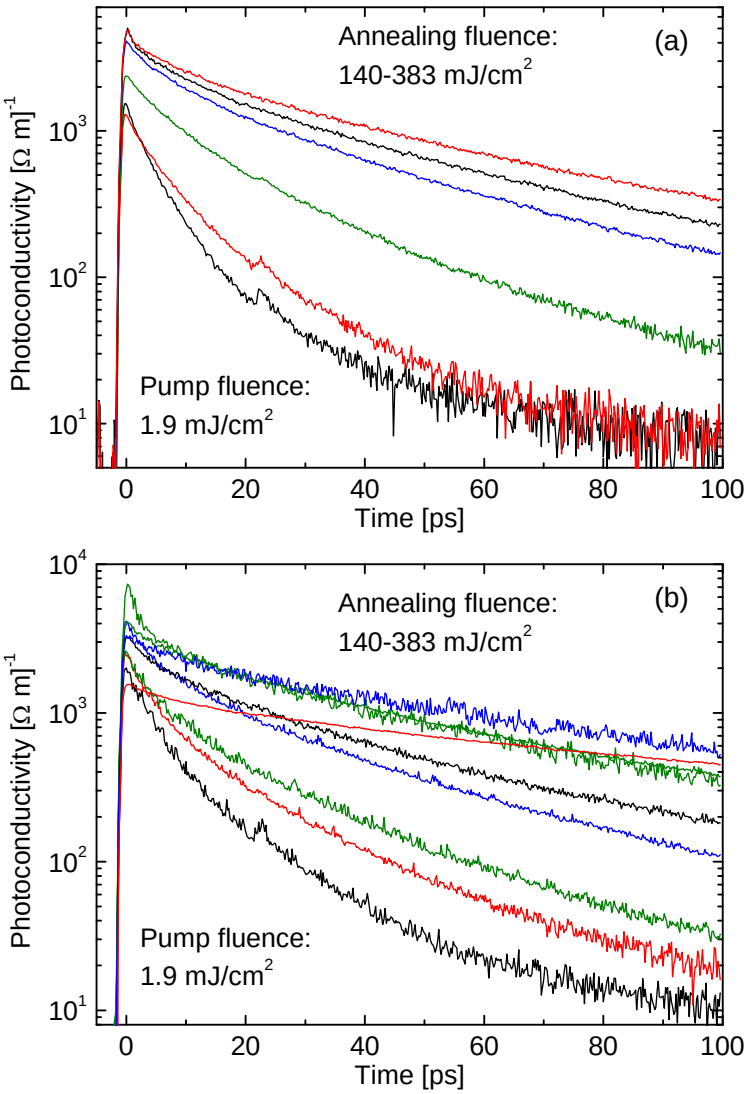

Figure 7.17: (a) Photoconductivity dynamics of black silicon containing copper produced with method low with annealing fluences in the range 140-383 mJ/cm^2. (b) Photoconductivity dynamics of black silicon containing copper produced with method high with annealing fluences in the range 140-436 mJ/cm^2. The carriers were excited with a pump fluence of 1.9 mJ/cm^2.

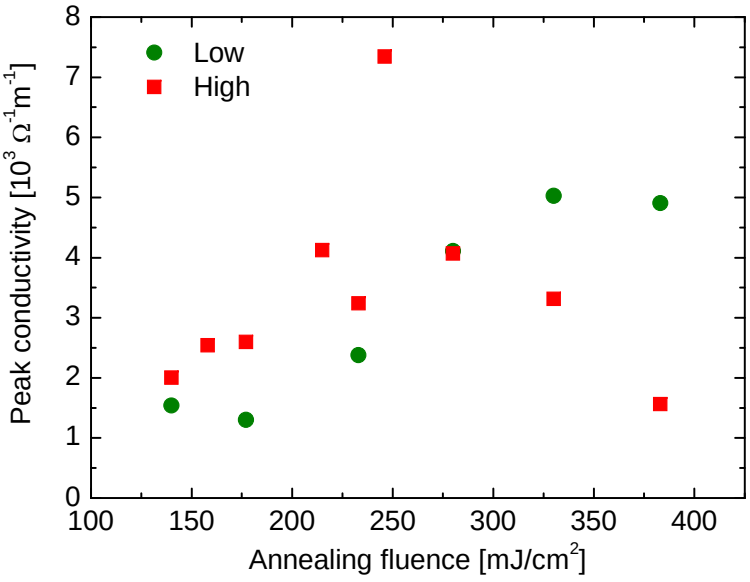

Figure 7.18: Peak photoconductivity as function of annealing for black silicon including copper, where the green dots represent the samples produced with method low and the red squares the samples produced with method high.

If we compare that with the 41-129 ps decay times of the black silicon samples without copper, it is evident that including copper will lead to fast trapping of photoexcited carriers. The photoconductivity decay time is decreased by at least an order of magnitude.

It is known that copper doping of silicon will create deep impurity levels inside the bandgap which can act as recombination centers [191]. A decrease in recombination time has been observed for copper doped silicon [192]. Although from the times observed here 1.8-7.5 ps it is clear that this is not electron-hole recombination. These fast decay times observed in time-resolved THz spectroscopy measurements are usually caused by trapping of electrons into a nonconductive state [121]. Since copper in silicon act as an acceptor [193], it is more likely it will trap holes, which has a lower contribution to the photoconductivity due to their higher effective mass. Besides it is not certain that we may describe the copper incorporations as doping. The original samples before annealing, contains a 10 nm copper layer on a 500 nm a-Si:H layer. This means that the thickness of the copper layer is 2 % of the thickness of the a-Si:H layer. Although annealing can remove some of the material, the total copper concentration after annealing is much higher then regular doping concentrations ($\sim$ 0.01 ppm) [194].

The slow component of the photoconductivity (Fig. 7.19) increases for higher annealing fluences for both production methods. For the samples produced with method low, decay times between 11 and 33 ps are observed.

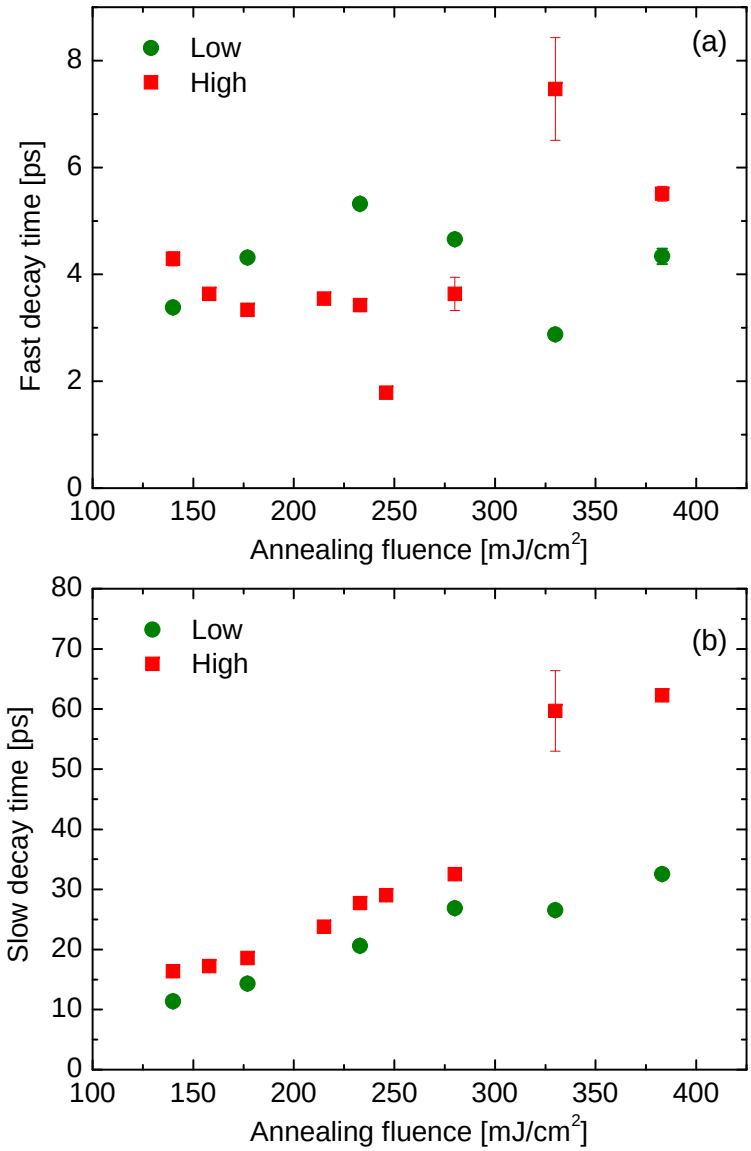

Figure 7.19: (a) Fast decay time of the photoconductivity obtained from double exponential fits to the traces shown in Fig. 7.17 as function of annealing fluence. (b) Slow decay time of the photoconductivity obtained from double exponential fits to the traces shown in Fig. 7.17 as function of annealing fluence. The green dots represent the samples produced with method low and the red squares for the samples produced with method high.

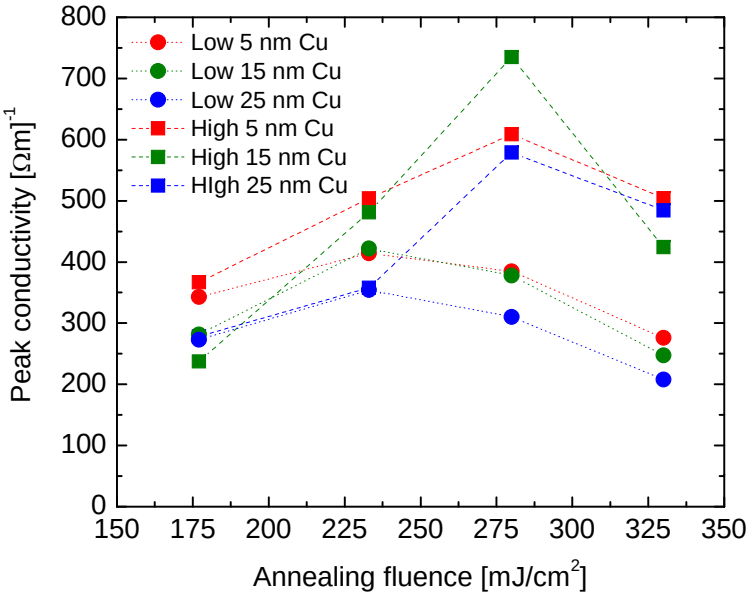

Figure 7.20: Peak conductivity of black silicon with copper as function of annealing fluence. A pump fluence of 0.18 mJ/cm^2 was used. The dotted lines are guides to the eye.

For the samples produced with method high the photoconductivity decay times are a little longer (16-62 ps). Also the slow decay is still faster than the decay for black silicon without copper (41-129 ps). So it is too simple to say that the copper only introduces extra traps, because the copper has apparently also an influence on the slow component of the photoconductivity decay. A possible explanation for the observed double exponential decay dynamics is the trapping of both electrons and holes is observed, where the fast decay corresponds to the trapping of electrons and the slow decay corresponds to the trapping of holes. Copper creates deep traps in silicon, which makes it more likely that both carriers can be trapped than in the case of regular p- or n-doping. One of the effects that can be responsible for the increase in decay time for higher annealing fluences is the higher crystallinity. Although no direct measurement on the crystallinity of the black silicon with copper samples were performed, it can be assumed that here the a-Si:H layer will also crystallize during annealing. However, this does not have to occur with the same rate. We do not know what the influence of the copper is on the crystallization of the amorphous silicon layer.

To further investigate the influence of copper on the ultrafast conductivity dynamics, copper films with different thicknesses were deposited on the a-Si:H film prior to laser annealing. Copper film thicknesses of 5, 15 and 25 nm were used. The production of black silicon by laser annealing was done as described in Sec. 7.2. All samples were pumped with a fluence of 0.18

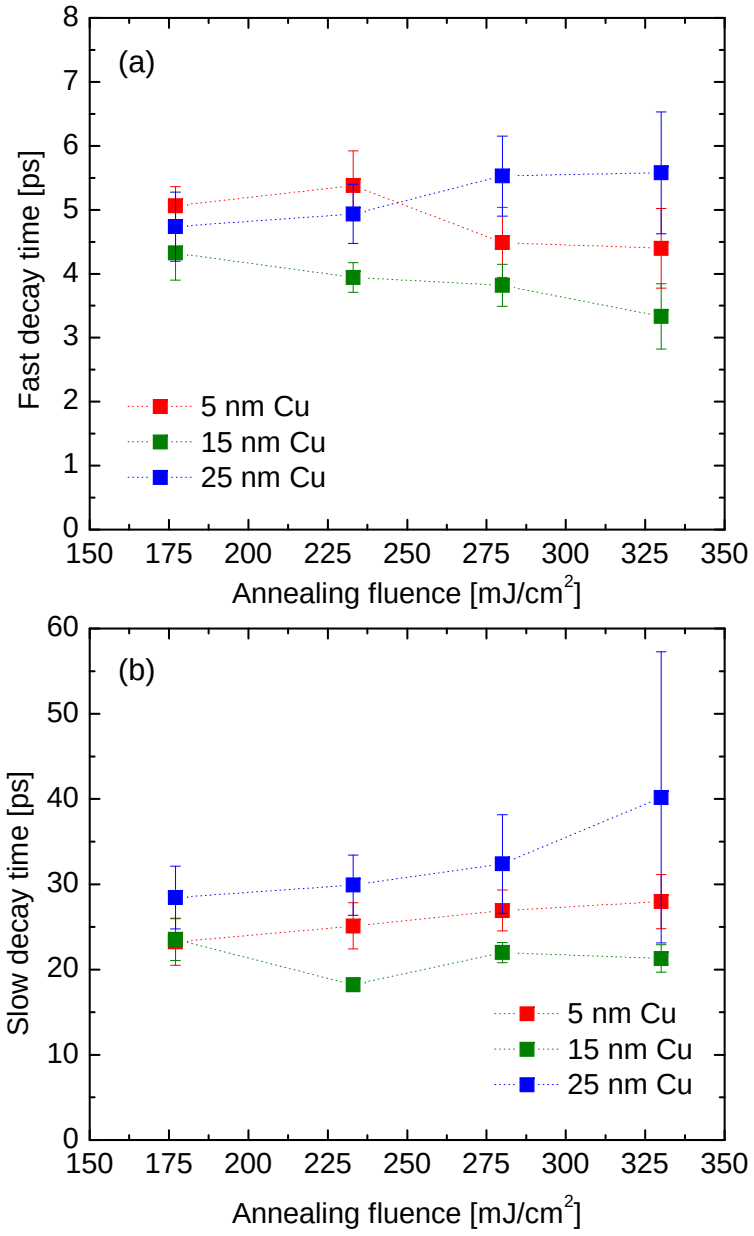

Figure 7.21: (a) Fast decay time as function of annealing fluence for the samples produced with method low with copper layer thicknesses of 5, 15 and 25 nm. (b) Slow decay time as function of annealing fluence for the samples produced with method low with copper layer thicknesses of 5, 15 and 25 nm.

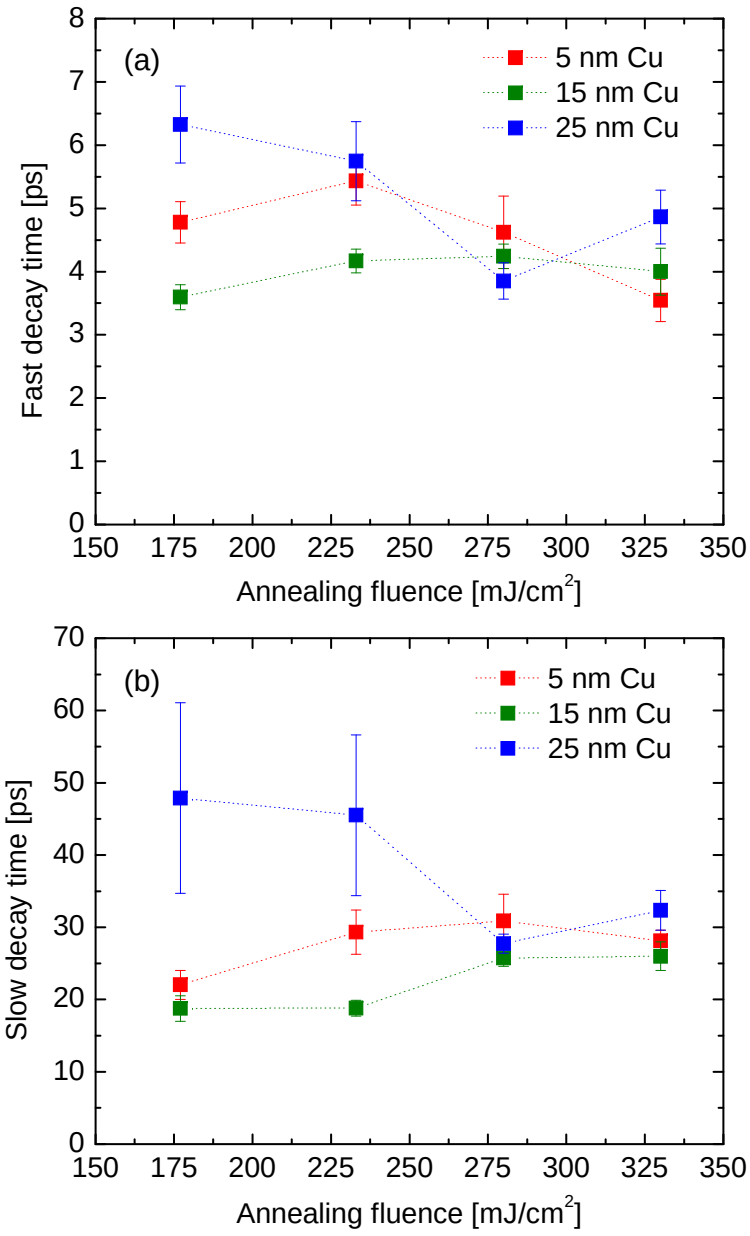

Figure 7.22: Fast decay time as function of annealing fluence for the samples produced with method high with copper layer thicknesses of 5, 15 and 25 nm. (b) Slow decay time as function of annealing fluence for the samples produced with method high with copper layer thicknesses of 5, 15 and 25 nm.

mJ/cm^2. The photoconductivity traces (not shown here) show the typical bi-exponential decay for black silicon with copper (Fig. 7.17). The peak photoconductivity as function of annealing fluence for the samples produced with both method low and high and for the three different copper layer thicknesses are shown in Fig. 7.20. The dotted lines are guides to the eye. The peak conductivity as function of pump fluences shows similar behavior as other black silicon samples, where the highest peak conductivity is observed when the samples were produced with an intermediate annealing fluence. A lower peak photoconductivity than for the samples with a 10 nm thick copper layer (Fig. 7.18) was observed because a much lower pump fluence was used.

From fits with a bi-exponential decay function to the photoconductivity dynamics traces, the fast and slow decay time constants are obtained. Fig. 7.21(a) and (b) show respectively the fast and slow decay time as function of annealing fluence for the samples produced with method low. Fig. 7.22(a) and (b) shows respectively the fast and slow decay times as function of annealing fluence for the samples produced with method high. Similar decay times for both the fast and slow component as for the samples with a 10 nm thick copper layer are observed. Changing the copper layer thicknesses has not a significant influence on the decay time. The shortest decay times are observed for the sample with a 15 nm thick copper layer. It seems like that around 10-15 nm there is an optimum for obtaining the shortest decay times. Both thinner and thicker copper layers will give slower dynamics. However, the limited number of different copper layer thicknesses together with the relatively small changes prevent any solid conclusions about how the amount of copper influence the decay dynamics.

7.6 X-ray diffraction spectroscopy

The crystallinity of black silicon was determined with Raman spectroscopy (Sec. 7.3). An other common measurement technique for determining the crystallinity of a sample is X-ray diffraction spectroscopy [195–197]. The transmission of a X-ray beam through a sample is measured and recorded on a X-ray sensitive photographic plate. The X-ray beam is generated in the same way as described in section 7.5, where high energy electrons remove electrons out of the K-shell of copper. The strong Kα-line of copper correspond to a wavelength of 1.542 Å. At this wavelength, comparable with the distance between the atoms, the scattering depends strongly on the orientation and distance between the atoms according to Bragg's law:

$$2d\sin[\theta] = n\lambda, \tag{7.1}$$

where d is the distance between the lattice planes, θ is the scattering angle, λ is the wavelength of the light and n is a positive integer. An amorphous

structure will result in a broad scattering range, while a crystalline structure will have a well defined scattering angle. By recording the transmitted X-ray on a photographic plate, the scattering angles can be obtained. This photographic plate contains erbium atoms, that will be excited by the X-ray photons to a metastable state. By illuminating the plate after the measurement, the population of excited atoms can be measured and hence the X-ray diffraction pattern. A crystalline structure will appear as a single dot on the plate, while an amorphous structure will show a broad band diffraction pattern. A micro- or nanocrystalline structure or a powder where the crystalline regions have random orientations, the diffraction angle will be well defined, but the direction will be random. So this will be observed as a ring. The most X-ray photons will not be scattered, so it is necessary to block the direct transmitted X-ray beam and prevent saturation of the plate.

An important parameter for calculating the scattering angle, which depends on the lattice structure, is the distance between the sample and the detector plate. To accurate determine this distance a test sample with known scattering angle is used. As a test sample a powder of silver behenate ($AgC_{22}H_{43}O_2$) is used. The diffraction pattern is shown in Fig. 7.23(a). The rings are caused by the scattering from the crystalline powder. Also visible is the shadow of the beam stop, which blocks the unscattered X-ray beam. To obtain the diffraction angle, the signal is integrated over all direction to obtain the scattered intensity as function of distance to the center of Fig. 7.23(a). The center of Fig. 7.23(a) as well as the shadow of the beam block is left out in the integration. When the distance from the sample to the detector plate is known the distance to the center can be calculated into a scattering angle. In practise the signal is measured at two times the scattering angle 2θ. The result for silver behenate is shown in Fig. 7.23(b). By comparing the positions of the peaks with the known positions, a sample-detector distance of 124 mm was obtained. This distance is used in the X-ray diffraction measurements on black silicon.

Due to the fused silica substrate, which is an amorphous material the black silicon samples used in the other experiments are not suitable for X-ray diffraction spectroscopy. Therefore black silicon on 100 μm thick sapphire substrates were used for the X-ray diffraction measurements. The sample were produced in the same way as described in Sec. 7.2. Only method high was used and no copper was deposited on the a-Si:H films. Fig. 7.24(a) shows the X-ray diffraction pattern of black silicon produced with method high with an annealing fluence of 280 mJ/cm^2. An averaging technique is used to make the scattering from the crystalline planes better visible. The ring is caused by the diffraction from crystalline silicon. The second order diffraction ring is also visible. The spots at large scattering angle (far from the center) that does not form a closed ring is from a crystalline structure with a preferred orientation. Thus this is most likely caused by diffraction from the sapphire substrate. From the diffraction pattern the

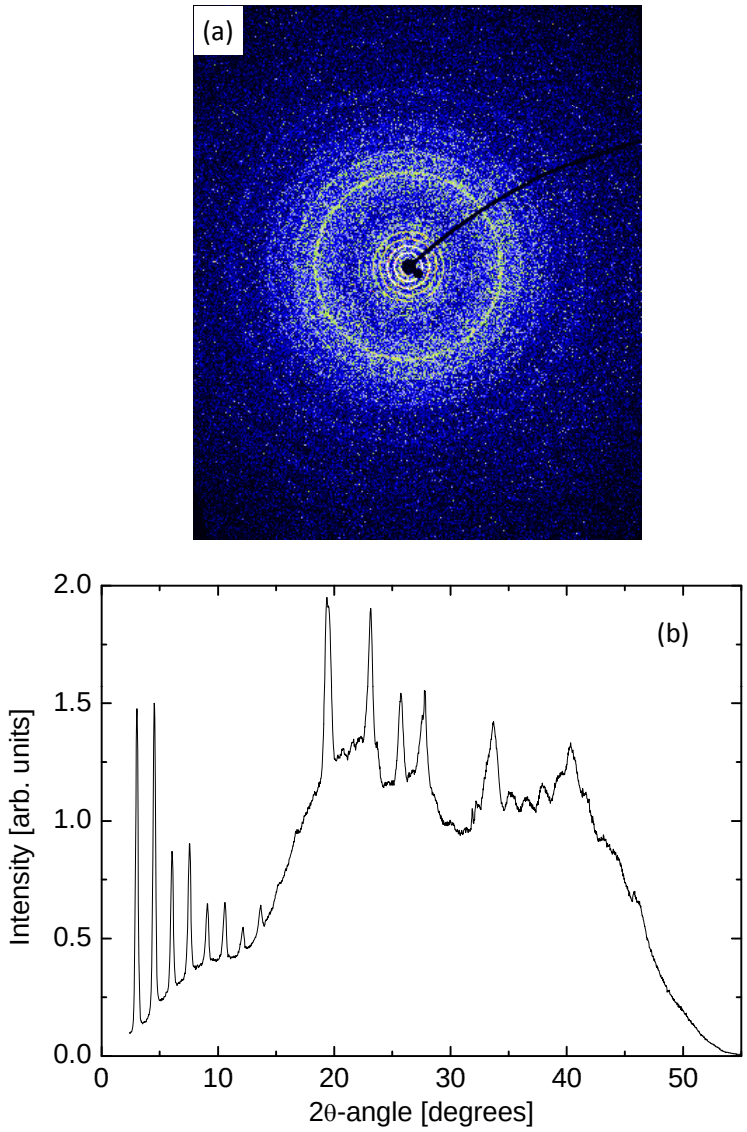

Figure 7.23: (a) X-ray diffraction pattern of silver behenate. (b) Scattered intensity as function of 2θ of silver behenate, where θ is the scattering angle.

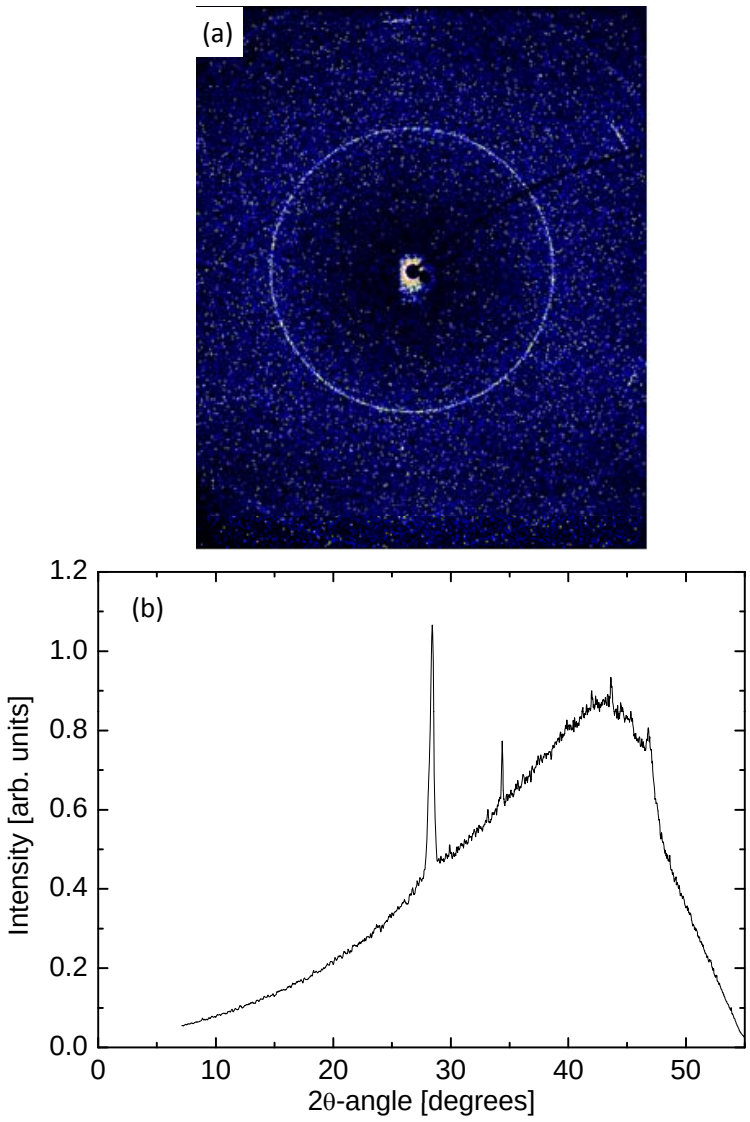

Figure 7.24: (a) X-ray diffraction pattern of black silicon produced with method high with an annealing fluence of 280 mJ/cm^2. (b) Scattered intensity as function of 2θ of black silicon produced with method high with an annealing fluence of 280 mJ/cm^2. θ is the scattering angle.

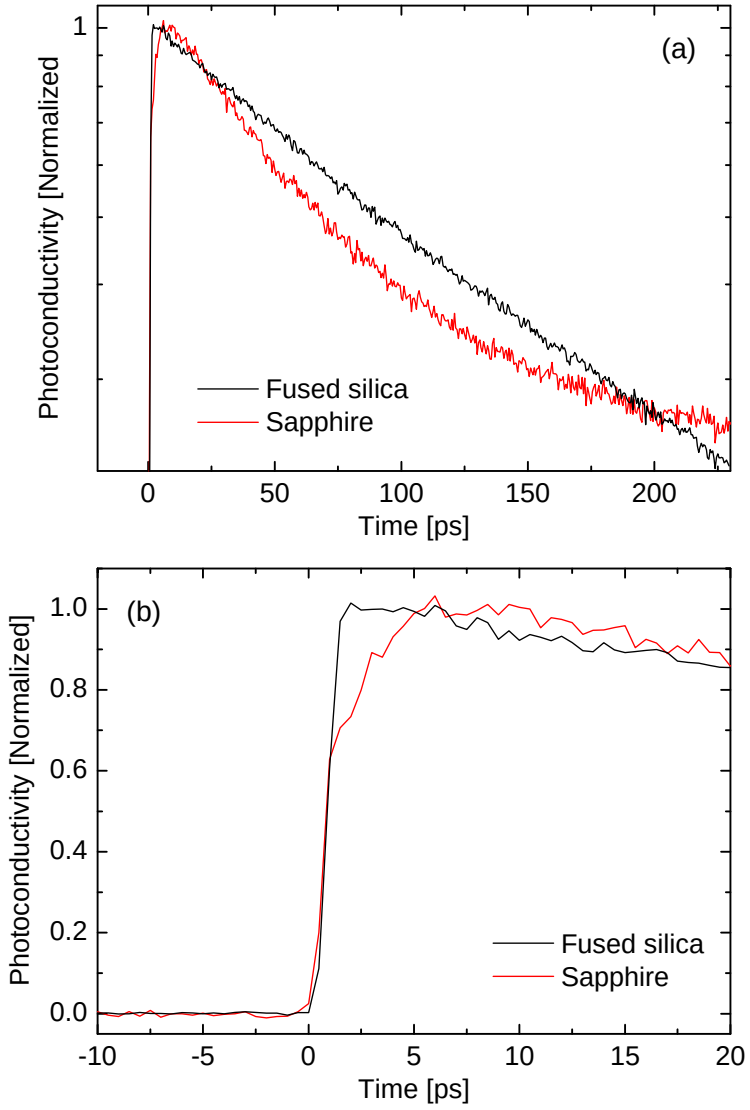

Figure 7.25: (a) Normalized photoconductivity dynamics for black silicon produced with method high with an annealing fluence of 280 mJ/cm^2 on a fused silica substrate (black line) and on a sapphire substrate (red line). (b) Close up of (a) around zero pump-probe delay time.

intensity as function of 2θ is calculated and shown in Fig. 7.24(b). The large peak at 28.5 degrees correspond to crystalline silicon. The small peak at approximately 47 degree is the second order diffraction. The peak at 34 degrees comes from a single high intensity point in Fig. 7.24(a) and the observed angle could not be linked to any element that could be present in black silicon. The fact that it is only a single point suggest that it is noise and not due to scattering of a crystalline structure. The broadband background is scattering from any amorphous material. It is not possible with X-ray diffraction to distinguish between different amorphous materials. To obtain a measure for the crystallinity of the sample, the integrated intensity from the silicon peaks are compared with the integrated intensity of the broadband background. A crystalline fraction of 2% is obtained. For samples produced with a lower annealing fluence even lower crystalline fraction are measured. This is significantly lower than the values obtained with Raman spectroscopy. It is not clear why such a low crystallinity is measured.

Besides the X-ray diffraction also time-resolved THz spectroscopy on the black silicon on sapphire substrates is performed. Fig. 7.25(a) shows the normalized photoconductivity as function of pump-probe delaytime for the sample produced with an annealing fluence of 280 mJ/cm^2 (red line). A pump fluence of 0.19 mJ/cm^2 was used. The black line in Fig. 7.25(a) shows the normalized photoconductivity dynamics of the black silicon produced with the same method and fluence but on a fused silica substrate. Two clear difference are observed. Firstly, a clear deviation from the near single exponential decay for the black silicon on fused silica is observed for black silicon on sapphire. Secondly, the rise of the photoconductivity upon optical excitation is much slower in the case of a sapphire substrate, see Fig. 7.25(b). We do not know what causes these difference and what influence the substrate has on the growth process. But these results show that a direct comparison between black silicon samples on different substrates must be carried out with great caution.

7.7 Conclusion

We showed the photoconductivity dynamics of black silicon, produced by laser annealing of a-Si:H films. The change in amplitude of the photoconductivity for different annealing fluences and method can for a large part be explained by a change in absorption of the 800 nm pump beam, supported by measurements of the transmission and absorption. However, changes in mobility need to be included to explain the change completely. The obtained photoconductivities are relatively low compared to bulk silicon, which is not so good for solar cells. A low conductivity causes that the high absorption and thus the generation of a lot of charge carriers in black silicon will not result in a high output current. However, this does not mean that black silicon

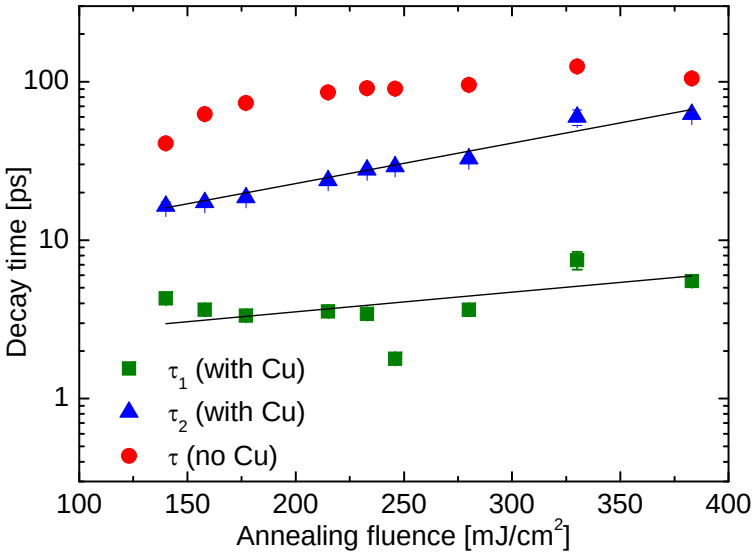

Figure 7.26: Photoconductivity decay time constants for black silicon produced with method high. The red dots are the decay time constant for black silicon without copper, the green squares are the fast decay time constant for black silicon with copper and the blue triangles are the slow decay time constants for black silicon with copper. The black lines are fits with an exponential function.

cannot be used at all for solar cells. If it is combined with other materials with better transport properties it still might be valuable. We also do not no if other fabrication processes like etching or laser annealing of crystalline silicon will lead to different optoelectronic properties. For other applications like fast photodetectors a high photoconductivity is less important.

Black silicon without copper has a double exponential decay behavior for low pump fluences. When the pump fluence is increased, the fast component of the decay gets slower and eventually disappears. For high pump fluences, the photoconductivity decays near-single exponential. The increase in the decay time constant for higher annealing fluences can be explained by crystallization of the a-Si:H film, supported by Raman spectroscopy data. The observed decrease of decay time for the highest annealing fluence in the case the samples were produced with method low can have different causes, like a change of stress in the sample or an increase of the number of traps. We explained that the latter one is more likely.

When copper is included in black silicon, the photoconductivity decay changes from near-single exponential to double exponential, indicating that copper introduces an extra decay path for the charge carriers. The photoconductivity decay times gets significantly shorter by introducing copper

into the black silicon samples. Decay times as short as 1.8-7.5 ps has been observed, depending on the annealing fluence and method used during the production. The amplitude of the photoconductivity for the samples with copper is the same order of magnitude as the amplitude of the photoconductivity of the samples without copper. So adding copper to black silicon has not a large influence on the absorption of the 800 nm pump and the carrier mobility. A summary of the photoconductivity decay time constant for black silicon produced with method high is shown in Fig. 7.26, where the red dots are the decay time constants for black silicon without copper and the green squares and blue triangles are the fast and slow decay time constants for black silicon with copper respectively. The black lines are exponential fits. For black silicon with copper the increase in decay time with increasing annealing fluence follows this exponential trend reasonable. While the for the samples without copper the increase in decay time for increasing annealing fluence is sublinear. We showed that the amount of copper does not have a large influence on the copper photoconductivity decay time. The shortest decay times are observed for the intermediate copper layer thickness of 15 nm.

The measurements in this chapter show that it is possible to produce black silicon with different absorption coefficients and different carrier lifetimes, by changing the annealing fluence or the production method. This means that it is possible to control some material properties during the production and design the black silicon to the requirements. However, the measurements described in this chapter also show the limitations. There is not one clear best method. For achieving a high absorption, a high annealing fluence should be used, just below the damaging threshold. For method low this is at 215 mJ/cm^2 and for method high this is at 280 mJ/cm^2. For obtaining a high photoconductivity, method high is preferable, because with method high about 50% higher photoconductivities can be obtained. If a short decay time is not required then a high annealing fluence is the best. But higher annealing fluence especially for method high also result in longer decay times. The shortest decay times are obtained for the lowest annealing fluences, also when copper is added. The problem with the lowest annealing fluence of 140 mJ/cm^2 is that it is still mainly amorphous silicon and the visible and infrared absorption is low.

The time-resolved THz spectroscopy experiments on black silicon gave a good idea on the carrier dynamics involved in photoexcited black silicon. However, a complete and detailed picture is not obtained. One important problem is that there is not a detailed image of the structure. We know how the structures look like and how large they are from the SEM images and we know that the silicon crystallizes during laser annealing from the Raman spectroscopy experiments. However, we do not know which part of the structure is crystalline silicon and which part is still amorphous. Since the absorption and carrier dynamics in crystalline silicon and amorphous

silicon is different, the carrier transport from one area to an other can be an important parameter in the photoconductivity dynamics. Therefore it is important to know the exact location of these areas. To obtain information about the crystalline and amorphous domains, transmission electron microscopy is needed. The complication is that for transmission electron microscopy, a thin ($\sim$10 nm) slice of the structure need to be prepared. For the black silicon with copper exist the same problem. It is known from the SEM with EDS images that the copper is mainly present in the structures, but not where in or at the structure. Again transmission electron microscopy could give this information.

In the attempt to obtain shorter decay times copper was used because of the high diffusivity in silicon and because it was known that copper in bulk silicon leads to shorter carrier lifetimes. We showed that copper in black silicon also results in shorter carrier lifetimes. However, there is no proof that adding copper to black silicon results in the best material properties in terms of short carrier lifetime, visible and infrared light absorption and high photoconductivity. So it can be interesting to try an other dopant, like e.g. Lithium, which also leads to the creation of deep traps and has a high diffusivity in silicon.

An important reason to produce black silicon by annealing amorphous silicon, is that amorphous silicon can easily be deposited on any substrate. However, a difference in the photoconductivity dynamics between black silicon on fused silicon and on sapphire is measured. To make conclusions about the influence of the substrate on the production of black silicon more experiments on black silicon on sapphire are needed, like SEM images and Raman spectroscopy. Then a direct comparison of the structures can be made which might explain the different photoconductivity dynamics.

Chapter 8

Conclusions and Outlook

The main topic of this thesis is time-resolved terahertz spectroscopy on semiconductor nanostructures. The aim was to study the ultrafast carrier dynamics in these semiconductor nanostructures. This thesis describes experiments on InGaAs/GaAs quantum dots, InGaN/GaN multiple quantum wells and black silicon, which is microstructured silicon. In an experiment charge carriers are excited with an optical pulse and are probed by measuring the transmission of a THz pulse. The advantage of using optical pump-THz probe spectroscopy is that the THz pulse is absorbed by "free" carriers. THz spectroscopy is a direct probe for the photoconductivity. So by measuring the transmission of a THz pulse for different pump-probe delay times, the photoconductivity dynamics can be studied. In many situations the carrier mobility does not change or changes only a little compare to the change in excited carrier density. In these situations, which are also shown in this thesis, THz spectroscopy can be used to directly study the ultrafast carrier dynamics. In particular the trapping of carriers into a localized state can be directly observed by an increase in the THz transmission, because localized carriers do not contribute to the photoconductivity.

Time-resolved terahertz spectroscopy can also be used to measure the frequency resolved THz conductivity. This thesis also include some measurement of the frequency resolved THz conductivity, partly because this measurement is required to validate the "1D-spectroscopy" method, where only the peak of the THz pulse is measured. This "1D-spectroscopy method, which is used to measure the photoconductivity dynamics, is the main topic of this thesis and therefore the experimental setups are designed for this purpose. The use of BNA as generation crystal and a 2-mm thick ZnTe as detection crystal result in a large amplitude of the measured THz pulse, but the bandwidth (0.3-2.5 THz) is relatively small. When only the peak of the THz pulse is measured the bandwidth is not important and a higher amplitude of the measured THz pulse will lead to a higher signal to noise ratio.

InGaAs/GaAs quantum dots

The first studied semiconductor nanostructures are InGaAs/GaAs quantum dots. As sample an InGaAs/GaAs quantum dot semiconductor saturable absorber mirror is used. Two experiments are performed. In the first experiment carriers are excited into the GaAs barrier layer with a 800 nm pump and the photoconductivity is measured with a THz probe pulse. After the instantaneous rise of the photoconductivity, limited by the time resolution of the setup a fast decay followed by a very long-lived part of the photoconductivity is observed. The fast decay of a few picoseconds is due to the trapping of charge carriers into the nonconducting quantum dots. The constant long-lived part of the photoconductivity is attributed to carriers excited in the type-II $Al_{0.9}Ga_{0.1}As$ Bragg reflector. Here, the electrons and holes are trapped in different part of the semiconductor and this separation result in a very low recombination probability. We showed that the trapping time of charge carriers into the quantum dot increases for larger pump fluence, which is attributed to state filling of the quantum dots states.

In the second experiment charge carriers are directly excited into the quantum dot ground state with a 1024 nm pump. A slow rise of the photoconductivity after excitation is observed which peaks after 35 ps and followed with a slow decay. The slow increase in photoconductivity is explained by the release of carriers from the nonconducting quantum dot states to the conducting states in the wetting layer and barrier. After 35 ps the electron-hole recombination in the conducting states starts dominating, which causes the decay of the photoconductivity. The peak photoconductivity as function of pump fluence follows a saturable absorption function with a saturation fluence of 42 ± 6 $\mu J/cm^2$. This value is comparable with measured saturation fluences in other quantum dot saturable absorber mirrors.

A simple rate equation model including only two states namely the quantum dot state and the conducting state explains the observed slow increase in the photoconductivity and the following slow decay. The release of carriers from the quantum dot to the conducting states, the trapping from the conducting states to the quantum dot states and the recombination in both states are included in the model. The model fails to explain the behavior in the first few ps after optical excitation. Where in the model the photoconductivity increases smoothly, in the measurements a kink is visible. For a detailed description the model needs to be extended. The conducting layer needs to be split up in the wetting layer and the barrier state, because the carrier mobility is different in these two states. So they will have a different contribution to the photoconductivity. Furthermore, all processes are temperature and carrier density dependent while in the model only state filling is taken into account in calculating the trapping time.

An important next step is to do a temperature dependent study, which can give important information about the physical process that causes the

release of carriers from the quantum dots to the conducting states. One physical process that could cause the release is thermal excitation. This process is strongly temperature dependent and disappears at liquid helium temperatures. An other possible process, carrier-carrier scattering is less temperature sensitive. So by measuring the THz transmission of excited quantum dots at liquid helium temperatures, the two processes could be distinguished.

Also not included in the experiments described in this thesis is the exchange of carriers between different quantum dot states. The used THz pulses have not enough energy to make a transition between different quantum dot states. However, if a larger bandwidth is used so that this transition can be made, also the inter quantum dot dynamics can be studied. When carriers are excited to the quantum dot ground state a dip in the THz transmission will be observed at the frequency that correspond to the energy difference between the quantum dot ground state and the quantum dot excited states. When carriers are excited to these excited states the THz absorption will go down due to state filling and a higher THz transmission is observed.

InGaN/GaN multiple quantum wells

InGaN/GaN multiple quantum wells are subject to a built-in piezoelectric field. The carrier dynamics in such a system are described by the quantum confined Stark effect, where the transition energy and probability depends on the excited carrier density due to the screening of the piezoelectric field. We showed that the quantum confined Stark effect has also consequences for the photoconductivity dynamics. A nonexponential decay of the photoconductivity is observed, which is attributed to the restoration of the initially screened built-in piezoelectric field as the carriers recombine. The built-in piezoelectric field is screened by excited electron-hole pairs, which due to the electric field form dipoles. The initially screened piezoelectric field result in a high recombination rate due the large overlap of the electron and hole wavefunctions. When carriers recombine the piezoelectric field is restored and the recombination rate goes down due the separation of the electron and hole wavefunctions. The dependence of the decay rate on the excited carrier density is also shown by the longer half decay time for lower pump fluences.

Further investigation is needed on the influence of carrier trapping on the photoconductivity decay dynamics in InGaN/GaN multiple quantum well. Trapping of carriers into localized state might explain the observed initial fast decay rate which lay in the 0.1 ps^{-1} regime. Localized states can be formed by changes in the quantum well thickness and compound fluctuations. Changes in quantum well thicknesses can result in the creation of a local quantum dot which can trap carriers. An extra complication is

that the quantum confined Stark effect can have an effect on the carrier trapping. To gain information about these traps the morphology need to be known. Transmission electron microscopy can give information about the local differences in quantum well thickness.

When carriers are excited in the quantum wells, the screening of the piezoelectric field will also result in the generation of acoustic waves. There are several phenomena where the THz waves and acoustic waves could be combined in the same experiments, which is interesting to study. These effects if measurable are very weak and a better signal to noise ratio is required. Firstly, directly after optical excitation the multiple quantum well superlattice structure will start vibrating at THz frequencies, because the strain which causes the built-in piezoelectric field is released when the piezoelectric field is screened. This vibration will rearrange the individual atoms and thereby modulate the piezoelectric field. The photoconductivity decay rate depends on the piezoelectric field, so a modulation of this piezoelectric field due to the vibrating supperlattice could potentially be measured with time-resolved THz spectroscopy. The vibrating lattice will launch a traveling acoustic wave into the material. When the piezoelectricity is constant the traveling acoustic wave will not generate a polarization current. However, when an interface or a surface where the sign of the acoustic wave is flipped a polarization current will be generated which leads to the radiation of an electromagnetic wave with the same frequencies as the acoustic wave. Since in the acoustic wave frequencies up to the THz regime are generated, THz electromagnetic waves could be generated from the acoustic wave.

Black silicon

Laser annealing of a-Si:H films lead to the formation of microstructures on the surface. Optical transmission experiments show that the visible and infrared light absorption is significantly increased when higher annealing fluences are used. During annealing the amorphous silicon crystallizes. This is supported by Raman spectroscopy experiments on the black silicon samples. The photoconductivity decay dynamics is measured by time-resolved THz spectroscopy. Two different pulse shaped are used in the annealing and we show that both the pulse shape and the annealing fluence have a large influence on the amplitude of the photoconductivity and on the decay time. A pump fluence dependent study showed a change in photoconductivity dynamics as more carriers are excited. For low pump fluences a double exponential decay is observed. When the pump fluence is increased the fast decay component gets slower and eventually disappears, indicating the saturation of a trap state. For high pump fluences a single exponential decay is observed.

On part of the samples a copper film was deposited on the a-Si:H layer prior to laser annealing. We showed that laser annealing result again in the

formation of microstructures, where the copper is mainly situating in or at the microstructures. The time-resolved THz spectroscopy experiments show that adding copper to black silicon results in a much fast and double exponential decay of the photoconductivity. The change from single to double exponential decay together with the shorter carrier lifetime, indicates that the copper creates an extra decay path for the photoexcited carriers. The ability of decreasing the carrier lifetime in black silicon significantly to a few ps by adding copper to the material makes it potentially interesting for a wider range of applications like fast photodiode, optical switches and THz generation, where a short carrier lifetime is a key parameter.

For a complete understanding of the ultrafast carrier dynamics detailed knowledge about the structures is important. Now only the shape and size of structures is known and some idea about the total crystallinity of the samples. For a better explanation of the measured photoconductivity, knowledge about the size and distribution of crystalline and amorphous domains is required. This information can be obtained from transmission electron microscopy images of a thin ($\sim$10 nm thick) slice of the sample. Transmission electron microscopy in combination with energy dispersive X-ray spectroscopy can also reveal the exact location of the copper in or at the structures.

A large part of the experiments on black silicon involved the quest for obtaining shorter carrier lifetimes, which was achieved by adding copper. Copper was added because it was known that copper decreases the carrier lifetime in bulk silicon and because the diffusivity of copper in silicon is high. However, copper might not be the only solution to achieve shorter carrier lifetimes. So adding other materials to black silicon might result in interesting properties.

An other aspect that needs further investigation is the influence of the substrate. One of the large advantage of the present production process of black silicon is that it can be deposited on a wide variety of substrates. At first it is assumed that the substrate has no influence on the production of black silicon. However, we measured different photoconductivity dynamics of black silicon on fused silica and black silicon on sapphire. Also the information extracted from the X-ray transmission spectroscopy experiments, measured on a sapphire substrate, contradicts the Raman spectroscopy results, measured on a fused silica substrate. One of the experiments that can give more information is Raman spectroscopy on black silicon on sapphire substrate. So that a direct comparison of the crystallinity of the sample can be made instead of via different experiments.

It is mentioned very shortly that black silicon can be used for generating THz radiation, but that it was very weak. However, improvements can be made. One idea is to built an antenna structure on the black silicon and generate the THz radiation by using it as a photoconductive switch. For the photoconductive switch a short carrier lifetime is beneficial, so black silicon

with copper would be a good candidate.

Bibliography

[1] D. H. Auston. Picosecond optoelectronic switching and gating in silicon. *Appl. Phys. Lett.*, 26:101–103, 1975.

[2] D. H. Auston, K. P. Cheung, and P. R. Smith. Picosecond photoconducting Hertzian dipoles. *Appl. Phys. Lett.*, 45:284–286, 1984.

[3] D. H. Auston, K. P. Cheung, J. A. Valdmanis, and D. A. Kleinman. Cherenkov radiation from femtosecond optical pulses in electro-optic media. *Phys. Rev. Lett.*, 53:1555–1558, 1984.

[4] P.R. Smith, D.H. Auston, and M.C. Nuss. Subpicosecond photoconducting dipole antennas. *IEEE J. Quantum Electon.*, 24:255–260, 1988.

[5] C. Fattinger and D. Grischkowsky. Point source terahertz optics. *Appl. Phys. Lett.*, 53:1480–1482, 1988.

[6] C. Fattinger and D. Grischkowsky. Terahertz beams. *Appl. Phys. Lett.*, 54:490–492, 1989.

[7] L. Xu, X.-C. Zhang, and D. H. Auston. Terahertz beam generation by femtosecond optical pulses in electro-optic materials. *Appl. Phys. Lett.*, 61:1784–1786, 1992.

[8] X.-C. Zhang, Y. Jin, and X. F. Ma. Coherent measurement of THz optical rectification from electro-optic crystals. *Appl. Phys. Lett.*, 61:2764–2766, 1992.

[9] X.-C. Zhang, X. F. Ma, Y. Jin, T.-M. Lu, E. P. Boden, P. D. Phelps, K. R. Stewart, and C. P. Yakymyshyn. Terahertz optical rectification from a nonlinear organic crystal. *Appl. Phys. Lett.*, 61:3080–3082, 1992.

[10] D. Grischkowsky, S. Keiding, M. van Exter, and C. Fattinger. Far-infrared time-domain spectroscopy with terahertz beams of dielectrics and semiconductors. *J. Opt. Soc. Am. B*, 7:2006–2015, 1990.

[11] Martin van Exter and D. Grischkowsky. Carrier dynamics of electrons and holes in moderately doped silicon. *Phys. Rev. B*, 41:12140–12149, 1990.

[12] B. M. Fischer, M. Walther, and P. Uhd Jepsen. Far-infrared vibrational modes of DNA components studied by terahertz time-domain spectroscopy. *Phys. Med. and Biol.*, 47:3807, 2002.

[13] M. Walther, P. Plochocka, B. Fischer, H. Helm, and P. Uhd Jepsen. Collective vibrational modes in biological molecules investigated by terahertz time-domain spectroscopy. *Biopolymers*, 67:310–313, 2002.

[14] M. C. Nuss, D. H. Auston, and F. Capasso. Direct subpicosecond measurement of carrier mobility of photoexcited electrons in gallium arsenide. *Phys. Rev. Lett.*, 58:2355–2358, 1987.

[15] A. Leitenstorfer, S. Hunsche, J. Shah, M. C. Nuss, and W. H. Knox. Femtosecond charge transport in polar semiconductors. *Phys. Rev. Lett.*, 82:5140 LP – 5143, 1999.

[16] A. Leitenstorfer, S. Hunsche, J. Shah, M. C. Nuss, and W. H. Knox. Femtosecond high-field transport in compound semiconductors. *Phys. Rev. B*, 61:16642 LP – 16652, 2000.

[17] R. Huber, F. Tauser, A. Brodschelm, M. Bichler, G. Abstreiter, and A. Leitenstorfer. How many-particle interactions develop after ultrafast excitation of an electron-hole plasma. *Nature*, 414:286–289, 2001.

[18] R. A. Kaindl, M. A. Carnahan, D. Hagele, R. Lovenich, and D. S. Chemla. Ultrafast terahertz probes of transient conducting and insulating phases in an electron-hole gas. *Nature*.

[19] G. Gunter, A. A. Anappara, J. Hees, A. Sell, G. Biasiol, L. Sorba, S. De Liberato, C. Ciuti, A. Tredicucci, A. Leitenstorfer, and R. Huber. Sub-cycle switch-on of ultrastrong light-matter interaction. *Nature*, 458:178–181, 2009.

[20] P. Parkinson, J. Lloyd-Hughes, Q. Gao, H. H. Tan, C. Jagadish, M. B. Johnston, and L. M. Herz. Transient terahertz conductivity of GaAs nanowires. *Nano Lett.*, 7:2162–2165, 2007.

[21] M. van Exter, C. Fattinger, and D. Grischkowsky. Terahertz time-domain spectroscopy of water vapor. *Opt. Lett.*, 14:1128–1130, 1989.

[22] P. Uhd Jepsen, U. Møller, and H. Merbold. Investigation of aqueous alcohol and sugar solutions with reflection terahertz time-domain spectroscopy. *Opt. Express*, 15:14717–14737, 2007.

[23] H. Nemec, H.-K. Nienhuys, E. Perzon, F. Zhang, O. Inganäs, P. Kuzel, and V. Sundström. Ultrafast conductivity in a low-band-gap polyphenylene and fullerene blend studied by terahertz spectroscopy. *Phys. Rev. B*, 79:245326, 2009.

[24] M. Walther, B. Fischer, M. Schall, H. Helm, and P. Uhd Jepsen. Far-infrared vibrational spectra of all-trans, 9-cis and 13-cis retinal measured by THz time-domain spectroscopy. *Chem. Phys. Lett.*, 332:389–395, 2000.

[25] M. Walther, D. G. Cooke, C. Sherstan, M. Hajar, M. R. Freeman, and F. A. Hegmann. Terahertz conductivity of thin gold films at the metal-insulator percolation transition. *Phys. Rev. B*, 76:125408–9, 2007.

[26] M. C. Beard, G. M. Turner, and C. A. Schmuttenmaer. Transient photoconductivity in GaAs as measured by time-resolved terahertz spectroscopy. *Phys. Rev. B*, 62:15764 LP – 15777, 2000.

[27] D. M. Mittleman, R. H. Jacobsen, R. Neelamani, R. G. Baraniuk, and M. C. Nuss. Gas sensing using terahertz time-domain spectroscopy. 67:379–390, 1998.

[28] J. Zhao, J. A. Bardecker, A. M. Munro, M. S. Liu, Y. Niu, I-K. Ding, J. Luo, B. Chen, A. K.-Y. Jen, and D. S. Ginger. Efficient CdSe/CdS quantum dot light-emitting diodes using a thermally polymerized hole transport layer. *Nano Lett.*, 6:463–467, 2006.

[29] S. Nakamura, M. Senoh, N. Iwasa, and S. Nagahama. High-power InGaN single-quantum-well-structure blue and violet light-emitting diodes. *Appl. Phys. Lett.*, 67:1868–1870, 1995.

[30] F. Qian, S. Gradečak, Y. Li, C.-Y. Wen, and C. M. Lieber. Core/multishell nanowire heterostructures as multicolor, high-efficiency light-emitting diodes. *Nano Lett.*, 5:2287–2291, 2005.

[31] Jerome Faist, Federico Capasso, Deborah L. Sivco, Carlo Sirtori, Albert L. Hutchinson, and Alfred Y. Cho. Quantum cascade laser. *Science*, 264:553–556, 1994.

[32] S. Fafard, K. Hinzer, S. Raymond, M. Dion, J. McCaffrey, Y. Feng, and S. Charbonneau. Red-emitting semiconductor quantum dot lasers. *Science*, 274:1350–1353, 1996.

[33] E. U. Rafailov, M. A. Cataluna, and W. Sibbett. Mode-locked quantum-dot lasers. *Nat. Photonics*, 1:395–401, 2007.

[34] X. Duan, Y. Huang, R. Agarwal, and C. M. Lieber. Single-nanowire electrically driven lasers. *Nature*, 421:241–245, 2003.

[35] Y. Arakawa and H. Sakaki. Multidimensional quantum well laser and temperature dependence of its threshold current. *Appl. Phys. Lett.*, 40:939–941, 1982.

[36] M. D. Kelzenberg, D. B. Turner-Evans, B. M. Kayes, M. A. Filler, M. C. Putnam, N. S. Lewis, and H. A. Atwater. Photovoltaic measurements in single-nanowire silicon solar cells. *Nano Lett.*, 8:710–714, 2008.

[37] N. J. Ekins-Daukes, K. W. J. Barnham, J. P. Connolly, J. S. Roberts, J. C. Clark, G. Hill, and M. Mazzer. Strain-balanced GaAsP/InGaAs quantum well solar cells. *Appl. Phys. Lett.*, 75:4195–4197, 1999.

[38] A. J. Nozik. Quantum dot solar cells. *Phys. E*, 14:115 – 120, 2002.

[39] G. Konstantatos, I. Howard, A. Fischer, S. Hoogland, J. Clifford, E. Klem, L. Levina, and E. H. Sargent. Ultrasensitive solution-cast quantum dot photodetectors. *Nature*, 442:180–183, 2006.

[40] S. A. McDonald, G. Konstantatos, S. Zhang, P. W. Cyr, E. J. D. Klem, L. Levina, and E. H. Sargent. Solution-processed PbS quantum dot infrared photodetectors and photovoltaics. *Nat. Mater.*, 4:138–142, 2005.

[41] B. F. Levine. Quantum-well infrared photodetectors. *J. of Appl. Phys.*, 74:R1–R81, 1993.

[42] H. Kind, H. Yan, B. Messer, M. Law, and P. Yang. Nanowire ultraviolet photodetectors and optical switches. *Adv. Mater.*, 14:158–160, 2002.

[43] C. Soci, A. Zhang, B. Xiang, S. A. Dayeh, D. P. R. Aplin, J. Park, X. Y. Bao, Y. H. Lo, and D. Wang. ZnO nanowire UV photodetectors with high internal gain. *Nano Lett.*, 7:1003–1009, 2007.

[44] M. C. Beard, G. M. Turner, and C. A. Schmuttenmaer. Size-dependent photoconductivity in CdSe nanoparticles as measured by time-resolved terahertz spectroscopy. *Nano Lett.*, 2:983–987, 2002.

[45] M. C. Beard, G. M. Turner, J. E. Murphy, O. I. Micic, M. C. Hanna, A. J. Nozik, and C. A. Schmuttenmaer. Electronic coupling in InP nanoparticle arrays. *Nano Lett.*, 3:1695–1699, 2003.

[46] D. G. Cooke, F. A. Hegmann, Y. I. Mazur, W. Q. Ma, X. Wang, Z. M. Wang, G. J. Salamo, M. Xiao, T. D. Mishima, and M. B. Johnson. Anisotropic photoconductivity of ingaas quantum dot chains measured by terahertz pulse spectroscopy. *Appl. Phys. Lett.*, 85:3839–3841, 2004.

[47] D. G. Cooke, A. N. MacDonald, A. Hryciw, J. Wang, Q. Li, A. Meldrum, and F. A. Hegmann. Transient terahertz conductivity in photoexcited silicon nanocrystal films. *Phys. Rev. B*, 73:193311–4, 2006.

[48] E. Hendry, M. Koeberg, B. O'Regan, and M. Bonn. Local field effects on electron transport in nanostructured TiO_2 revealed by terahertz spectroscopy. *Nano Lett.*, 6:755–759, 2006.

[49] E. Hendry, M. Koeberg, F. Wang, H. Zhang, C. de Mello Donegá, D. Vanmaekelbergh, and M. Bonn. Direct observation of electron-to-hole energy transfer in CdSe quantum dots. *Phys. Rev. Lett.*, 96:057408, 2006.

[50] J. H. Strait, P. A. George, M. Levendorf, M. Blood-Forsythe, F. Rana, and J. Park. Measurements of the carrier dynamics and terahertz response of oriented germanium nanowires using optical-pump terahertz-probe spectroscopy. *Nano Lett.*, 9:2967–2972, 2009.

[51] Feng Wang, Jie Shan, Mohammad A. Islam, Irving P Herman, Mischa Bonn, and Tony F. Heinz. Exciton polarizability in semiconductor nanocrystals. *Nat. Mater.*, 5:861–864, 2006.

[52] P. Uhd Jepsen, D. G. Cooke, and M. Koch. Terahertz spectroscopy and imaging - Modern techniques and applications. *Laser and Photon. Rev.*, pages 1–43, 2010.

[53] M. Scheller and M. Koch. Terahertz quasi time domain spectroscopy. *Opt. Express*, 17:17723–17733, 2009.

[54] K. L. Sala, G. A. Kenney-Wallace, and G. E. Hall. CW autocorrelation measurements of picosecond laser pulses. *IEEE J. Quant. Elect.*, 16:990–996, 1980.

[55] F. Salin, P. Georges, G. Roger, and A. Brun. Single-shot measurements of a 52−fs pulse. *Appl. Opt.*, 26:4528–4531, 1987.

[56] G. D. Boyd and A. Ashkin. Theory of parametric oscillator threshold with single-mode optical masers and observation of amplification in $LiNbO_3$. *Phys. Rev.*, 146:187–198, 1966.

[57] T. Nakazato, M. Oyamada, N. Niimura, S. Urasawa, O. Konno, A. Kagaya, R. Kato, T. Kamiyama, Y. Torizuka, T. Nanba, Y. Kondo, Y. Shibata, K. Ishi, T. Ohsaka, and M. Ikezawa. Observation of coherent synchrotron radiation. *Phys. Rev. Lett.*, 63:1245–1248, 1989.

[58] G. L. Carr, M. C. Martin, W. R. McKinney, K. Jordan, G. R. Neil, and G. P. Williams. High-power terahertz radiation from relativistic electrons. 420:153–156, 2002.

[59] R. Köhler, A. Tredicucci, F. Beltram, H. E. Beere, E. H. Linfield, A. G. Davies, D. A. Ritchie, R. C. Iotti, and F. Rossi. Terahertz semiconductor-heterostructure laser. *Nature*, 417:156–159, 2002.

[60] E. R. Brown, F. W. Smith, and K. A. McIntosh. Coherent millimeter-wave generation by heterodyne conversion in low-temperature-grown gaas photoconductors. *J. of Appl. Phys.*, 73:1480–1484, 1993.

[61] H. Hamster, A. Sullivan, S. Gordon, W. White, and R. W. Falcone. Subpicosecond, electromagnetic pulses from intense laser-plasma interaction. *Phys. Rev. Lett.*, 71:2725–2728, 1993.

[62] Xu Xie, Jianming Dai, and X.-C. Zhang. Coherent control of THz wave generation in ambient air. *Phys. Rev. Lett.*, 96:075005, 2006.

[63] A. Sell, R. Scheu, A. Leitenstorfer, and R. Huber. Field-resolved detection of phase-locked infrared transients from a compact er:fiber system tunable between 55 and 107 THz. *Appl. Phys. Lett.*, 93:251107, 2008.

[64] Mark Cronin-Golomb. Cascaded nonlinear difference-frequency generation of enhanced terahertzwave production. *Opt. Lett.*, 29:2046–2048, 2004.

[65] J. Liu, X. Guo, J. Dai, and X.-C. Zhang. Optical property of beta barium borate in terahertz region. *Appl. Phys. Lett.*, 93:171102, 2008.

[66] Y.-S. Lee, T. Meade, V. Perlin, H. Winful, T. B. Norris, and A. Galvanauskas. Generation of narrow-band terahertz radiation via optical rectification of femtosecond pulses in periodically poled lithium niobate. *Appl. Phys. Lett.*, 76:2505–2507, 2000.

[67] Y.-S. Lee, T. Meade, M. DeCamp, T. B. Norris, and A. Galvanauskas. Temperature dependence of narrow-band terahertz generation from periodically poled lithium niobate. *Appl. Phys. Lett.*, 77:1244–1246, 2000.

[68] K.-L. Yeh, M. C. Hoffmann, J. Hebling, and Keith A. Nelson. Generation of 10 μJ ultrashort terahertz pulses by optical rectification. *Appl. Phys. Lett.*, 90:171121, 2007.

[69] Matthias C. Hoffmann, Ka-Lo Yeh, János Hebling, and Keith A. Nelson. Efficient terahertz generation by optical rectification at 1035 nm. *Opt. Express*, 15:11706–11713, 2007.

[70] H. Hashimoto, K. Kuroyanagi H. Takahashi, T. Yamada, and T. Kobayashi. Characteristics of the terahertz radiation from single crystals of N-substituted 2-methyl-4-nitroaniline. *J. Phys. Condens. Matter*, 13, 2001.

[71] K. Kuroyanagi, M. Fujiwara, H. Hashimoto, H. Takahashi, S.-I. Aoshima, and Y. Tsuchiya. All organic terahertz electromagnetic wave emission and detection using highly purified N-Benzyl-2-methyl-4-nitroaniline crystals. *Jpn J. of Appl. Phys.*, 45:4068–4073, 2006.

[72] P. L. Richards. Bolometers for infrared and millimeter waves. *J. Appl. Phys.*, 76:1–24, 1994.

[73] M. J. E. Golay. A pneumatic infra-red detector. *Rev. of Sci. Instr.*, 18:357–362, 1947.

[74] P. H. Siegel. Terahertz technology. *IEEE Trans. Microwave Theory Tech.*, 50:910–928, 2002.

[75] E. Budiarto, J. Margolies, S. Jeong, J. Son, and J. Bokor. High-intensity terahertz pulses at 1-kHz repetition rate. *IEEE J. Quant. Elect.*, 32:1839–1846, 1996.

[76] X.-C. Zhang and D. H. Auston. Optoelectronic measurement of semiconductor surfaces and interfaces with femtosecond optics. *J. of Appl. Phys.*, 71:326–338, 1992.

[77] P. Uhd Jepsen, R. H. Jacobsen, and S. R. Keiding. Generation and detection of terahertz pulses from biased semiconductor antennas. *J. Opt. Soc. Am. B*, 13:2424–2436, 1996.

[78] Q. Wu and X.-C. Zhang. Free-space electro-optic sampling of terahertz beams. *Appl. Phys. Lett.*, 67:3523–3525, 1995.

[79] P. Uhd Jepsen, C. Winnewisser, M. Schall, V. Schyja, S. R. Keiding, and H. Helm. Detection of THz pulses by phase retardation in lithium tantalate. *Phys. Rev. E*, 53:R3052 LP – R3054, 1996.

[80] Ajay Nahata, David H. Auston, Tony F. Heinz, and Chengjiu Wu. Coherent detection of freely propagating terahertz radiation by electro-optic sampling. *Appl. Phys. Lett.*, 68:150–152, 1996.

[81] A. Nahata, D. H. Auston, T. F. Heinz, and C. Wu. Coherent detection of freely propagating terahertz radiation by electro-optic sampling. *Appl. Phys. Lett.*, 68:150–152, 1996.

[82] P. C. M. Planken, H.-K. Nienhuys, H. J. Bakker, and T. Wenckebach. Measurement and calculation of the orientation dependence of terahertz pulse detection in ZnTe. *J. Opt. Soc. Am. B*, 18:313–317, 2001.

[83] D. Turchinovich and J. I. Dijkhuis. Performance of combined <1 0 0>-<1 1 0> ZnTe crystals in an amplified THz time-domain spectrometer. *Opt. Commun.*, 270:96 – 99, 2007.

[84] N. Katzenellenbogen and D. Grischkowsky. Electrical characterization to 4 THz of N- and P-type GaAs using THz time-domain spectroscopy. *Appl. Phys. Lett.*, 61:840–842, 1992.

[85] M. Brucherseifer, M. Nagel, P. Haring Bolivar, H. Kurz, A. Bosserhoff, and R. Buttner. Label-free probing of the binding state of DNA by time-domain terahertz sensing. *Appl. Phys. Lett.*, 77:4049–4051, 2000.

[86] L. Thrane, R.H. Jacobsen, P. Uhd Jepsen, and S.R. Keiding. Thz reflection spectroscopy of liquid water. *Chem. Phys. Lett.*, 240:330 – 333, 1995.

[87] M. C. Nuss, K. W. Goossen, J. P. Gordon, P. M. Mankiewich, M. L. O'Malley, and M. Bhushan. Terahertz time-domain measurement of the conductivity and superconducting band gap in niobium. *J. of Appl. Phys.*, 70:2238–2241, 1991.

[88] R. A. Kaindl, M. A. Carnahan, J. Orenstein, D. S. Chemla, H. M. Christen, H.-Y. Zhai, M. Paranthaman, and D. H. Lowndes. Far-infrared optical conductivity gap in superconducting MgB_2 films. *Phys. Rev. Lett.*, 88:027003, 2001.

[89] M. Born and E. Wolf. *Principles of Optics.* Cambridge University Press, 7th edition, 1999.

[90] C. A. Schmuttenmaer. Exploring dynamics in the far-infrared with terahertz spectroscopy. *Chem. Rev.*, 104:1759–1780, 2004.

[91] R. E. Glover and M. Tinkham. Transmission of superconducting films at millimeter-microwave and far infrared frequencies. *Phys. Rev.*, 104:844 LP – 845, 1956.

[92] M. Tinkham. Energy gap interpretation of experiments on infrared transmission through superconducting films. *Phys. Rev.*, 104:845–846, 1956.

[93] J. C. Maxwell-Garnett. Colours in metal glasses and metal films. *Philos. Trans. R. Soc. Lond.*, 203:385, 1904.

[94] J. C. Maxwell-Garnett. Colours in metal glasses, in metallic films, and in metallic solutions. II. *Philos. Trans. R. Soc. Lond.*, 205:237, 1906.

[95] D. A. G. Bruggeman. The calculation of various physical constants of heterogeneous substances. I. The dielectric constants and conductivities of mixtures composed of isotropic substances. *Ann. Phys.*, 24:636, 1935.

[96] D. Stroud. Generalized effective-medium approach to the conductivity of an inhomogeneous material. *Phys. Rev. B*, 12:3368–3373, 1975.

[97] N. V. Smith. Classical generalization of the drude formula for the optical conductivity. *Phys. Rev. B*, 64:155106, 2001.

[98] P. Uhd Jepsen, B. M. Fischer, A. Thoman, H. Helm, J. Y. Suh, R. Lopez, and R. F. Haglund. Metal-insulator phase transition in a VO_2 thin film observed with terahertz spectroscopy. *Phys. Rev. B*, 74:205103, 2006.

[99] D. J. Hilton, R. P. Prasankumar, S. Fourmaux, A. Cavalleri, D. Brassard, M. A. El Khakani, J. C. Kieffer, A. J. Taylor, and R. D. Averitt. Enhanced photosusceptibility near T_c for the light-induced insulator-to-metal phase transition in vanadium dioxide. *Phys. Rev. Lett.*, 99:226401, 2007.

[100] J. B. Baxter and C. A. Schmuttenmaer. Conductivity of ZnO nanowires, nanoparticles, and thin films using time-resolved terahertz spectroscopy. *J. of Phys. Chem. B*, 110:25229–25239, 2006.

[101] H. Nemec, P. Kuzel, and V. Sundström. Far-infrared response of free charge carriers localized in semiconductor nanoparticles. *Phys. Rev. B*, 79:115309–7, 2009.

[102] K. P. H. Lui and F. A. Hegmann. Ultrafast carrier relaxation in radiation-damaged silicon on sapphire studied by optical-pump–terahertz-probe experiments. *Appl. Phys. Lett.*, 78:3478–3480, 2001.

[103] K. P. H. Lui and F. A. Hegmann. Fluence- and temperature-dependent studies of carrier dynamics in radiation-damaged silicon-on-sapphire and amorphous silicon. *J. of Appl. Phys.*, 93:9012–9018, 2003.

[104] K. Iwaszczuk, D. G. Cooke, M. Fujiwara, H. Hashimoto, and P. Uhd Jepsen. Simultaneous reference and differential waveform acquisition in time-resolved terahertz spectroscopy. *Opt. Express*, 17:21969–21976, 2009.

[105] http://www.ioffe.ru/sva/nsm/semicond/gaas/bandstr.html.

[106] G. L. Dakovski, B. Kubera, S. Lan, and J. Shan. Finite pump-beam size effects in optical pump-terahertz probe spectroscopy. *J. Opt. Soc. Am. B*, 23:139, 2006.

[107] E.U. Rafailov, S.J. White, A.A. Lagatsky, A. Miller, W. Sibbett, D.A. Livshits, A.E. Zhukov, and V.M. Ustinov. Fast quantum-dot saturable absorber for passive mode-locking of solid-state lasers. *IEEE Phot. Tech. Lett.*, 16:2439 –2441, 2004.

[108] R. Herda, O.G. Okhotnikov, E.U. Rafailov, W. Sibbett, P. Crittenden, and A. Starodumov. Semiconductor quantum-dot saturable absorber mode-locked fiber laser. *IEEE Phot. Tech. Lett.*, 18:157 –159, 2006.

[109] H. C. Liu, M. Gao, J. McCaffrey, Z. R. Wasilewski, and S. Fafard. Quantum dot infrared photodetectors. *Appl. Phys. Lett.*, 78:79–81, 2001.

[110] A. A. Lagatsky, F. M. Bain, C. T. A. Brown, W. Sibbett, D. A. Livshits, G. Erbert, and E. U. Rafailov. Low-loss quantum-dot-based saturable absorber for efficient femtosecond pulse generation. *Appl. Phys. Lett.*, 91:231111–3, 2007.

[111] S. Raymond, S. Fafard, P. J. Poole, A. Wojs, P. Hawrylak, S. Charbonneau, D. Leonard, R. Leon, P. M. Petroff, and J. L. Merz. State filling and time-resolved photoluminescence of excited states in $In_xGa_{1-x}As$/GaAs self-assembled quantum dots. *Phys. Rev. B*, 54:11548–11554, 1996.

[112] D. Morris, N. Perret, and S. Fafard. Carrier energy relaxation by means of Auger processes in InAs/GaAs self-assembled quantum dots. *Appl. Phys. Lett.*, 75:3593–3595, 1999.

[113] M. Paillard, X. Marie, P. Renucci, T. Amand, A. Jbeli, and J. M. Gérard. Spin relaxation quenching in semiconductor quantum dots. *Phys. Rev. Lett.*, 86:1634–1637, 2001.

[114] J. Feldmann, S. T. Cundiff, M. Arzberger, G. Bohm, and G. Abstreiter. Carrier capture into InAs/GaAs quantum dots via multiple optical phonon emission. *J of Appl Phys*, 89:1180–1183, 2001.

[115] T. Müller, F. F. Schrey, G. Strasser, and K. Unterrainer. Ultrafast intraband spectroscopy of electron capture and relaxation in InAs/GaAs quantum dots. *Appl. Phys. Lett.*, 83:3572–3574, 2003.

[116] D. A. Yarotski, Ri. D. Averitt, N. Negre, S. A. Crooker, A. J. Taylor, G. P. Donati, A. Stintz, L. F. Lester, and K. J. Malloy. Ultrafast carrier-relaxation dynamics in self-assembled InAs/GaAs quantum dots. *J. Opt. Soc. Am. B*, 19:1480–1484, 2002.

[117] James E. Murphy, Matthew C. Beard, and Arthur J. Nozik. Time-resolved photoconductivity of PbSe nanocrystal arrays. *J. of Phys. Chem. B*, 110:25455–25461, 2006.

[118] D. Turchinovich, K. Pierz, and P. Uhd Jepsen. InAs/GaAs quantum dots as efficient free carrier deep traps. *Phys. Stat. Sol. (c)*, 0:1556–1559, 2003.

[119] R. P. Prasankumar, A. Scopatz, D. J. Hilton, A. J. Taylor, R. D. Averitt, J. M. Zide, and A. C. Gossard. Carrier dynamics in self-assembled ErAs nanoislands embedded in GaAs measured by optical-

pump terahertz-probe spectroscopy. *Appl. Phys. Lett.*, 86:201107–3, 2005.

[120] D. Turchinovich, P. Uhd Jepsen, B. S. Monozon, M. Koch, S. Lahmann, U. Rossow, and A. Hangleiter. Ultrafast polarization dynamics in biased quantum wells under strong femtosecond optical excitation. *Phys. Rev. B*, 68:241307, 2003.

[121] H. P. Porte, P. Uhd Jepsen, N. Daghestani, E. U. Rafailov, and D. Turchinovich. Ultrafast release and capture of carriers in InGaAs/GaAs quantum dots observed by time-resolved terahertz spectroscopy. *Appl. Phys. Lett.*, 94:262104–3, 2009.

[122] T. R. Nielsen, P. Gartner, and F. Jahnke. Many-body theory of carrier capture and relaxation in semiconductor quantum-dot lasers. *Phys. Rev. B*, 69:235314, 2004.

[123] J. Feldmann, J. Nunnenkamp, G. Peter, E. Göbel, J. Kuhl, K. Ploog, P. Dawson, and C. T. Foxon. Experimental study of the γ -X electron transfer in type-II (Al,Ga)As/AlAs superlattices and multiple-quantum-well structures. *Phys. Rev. B*, 42:5809 LP – 5821, 1990.

[124] M. Haiml, R. Grange, and U. Keller. Optical characterization of semiconductor saturable absorbers. *Appl. Phys. B*, 79:331–339, 2004.

[125] S. Nakamura, M. Senoh, S.-I. Nagahama, N. Iwasa, T. Yamada, T. Matsushita, H. Kiyoku, and Y. Sugimoto. InGaN-based multi-quantum-well-structure laser diodes. *Jpn. J. of Appl. Phys.*, 35:L74 – L76, 1996.

[126] S. Nakamura. The roles of structural imperfections in InGaN-based blue light-emitting diodes and laser diodes. *Science*, 281:956–961, 1998.

[127] D. A. B. Miller, D. S. Chemla, T. C. Damen, A. C. Gossard, W. Wiegmann, T. H. Wood, and C. A. Burrus. Band-edge electroabsorption in quantum well structures: The quantum-confined stark effect. *Phys. Rev. Lett.*, 53:2173 LP – 2176, 1984.

[128] D. Turchinovich, B. S. Monozon, and P. Uhd Jepsen. Role of dynamical screening in excitation kinetics of biased quantum wells: Nonlinear absorption and ultrabroadband terahertz emission. *J. of Appl. Phys.*, 99:013510–8, 2006.

[129] Ü. Özgür, C.-W. Lee, and H. O. Everitt. Control of coherent acoustic phonons in semiconductor quantum wells. *Phys. Rev. Lett.*, 86:5604 LP – 5607, 2001.

[130] E. Makarona, B. Daly, J.-S. Im, H. Maris, A. Nurmikko, and J. Han. Coherent generation of 100 GHz acoustic phonons by dynamic screening of piezoelectric fields in AlGaN/GaN multilayers. *Appl. Phys. Lett.*, 81:2791–2793, 2002.

[131] C.-K. Sun, J.-C. Liang, and X.-Y. Yu. Coherent acoustic phonon oscillations in semiconductor multiple quantum wells with piezoelectric fields. *Phys. Rev. Lett.*, 84:179 LP – 182, 2000.

[132] T. Takeuchi, S. Sota, M. Katsuragawa, M. Komori, H. Takeuchi, H. Amano, and I. Akasaki. Quantum-confined Stark effect due to piezoelectric fields in GaInN strained quantum wells. *Jpn. J. of Appl. Phys.*, 36:382–385, 1997.

[133] T. Takeuchi, C. Wetzel, S. Yamaguchi, H. Sakai, H. Amano, I. Akasaki, Y. Kaneko, S. Nakagawa, Y. Yamaoka, and N. Yamada. Determination of piezoelectric fields in strained GaInN quantum wells using the quantum-confined Stark effect. *Appl. Phys. Lett.*, 73:1691–1693, 1998.

[134] S. F. Chichibu, A. C. Abare, M. S. Minsky, S. Keller, S. B. Fleischer, J. E. Bowers, E. Hu, U. K. Mishra, L. A. Coldren, S. P. DenBaars, and T. Sota. Effective band gap inhomogeneity and piezoelectric field in InGaN/GaN multiquantum well structures. *Appl. Phys. Lett.*, 73:2006–2008, 1998.

[135] A. Pinos, S. Marcinkevičius, K. Liu, M. S. Shur, E. Kuokštis, G. Tamulaitis, R. Gaska, J. Yang, and W. Sun. Screening dynamics of intrinsic electric field in AlGaN quantum wells. *Appl. Phys. Lett.*, 92:061907–3, 2008.

[136] X. Liu, E. U. Rafailov, D. Livshits, and D. Turchinovich. Quantum well saturable absorber mirror with electrical control of modulation depth. *Appl. Phys. Lett.*, 97:051103, 2010.

[137] J. S. Im, H. Kollmer, J. Off, F. Scholz, and A. Hangleiter. Carrier confinement in GaInN/AlGaN/GaN quantum wells with asymmetric barriers: direction of the piezoelectric field. *Mat. Sci. Eng. B*, 59:315–318, 1999.

[138] W. Zhang, Abul K. Azad, and D. Grischkowsky. Terahertz studies of carrier dynamics and dielectric response of n-type, freestanding epitaxial GaN. *Appl. Phys. Lett.*, 82:2841–2843, 2003.

[139] T. Nagashima, K.e Takata, S. Nashima, H. Harima, and M. Hangyo. Measurement of electrical properties of GaN thin films using terahertz-time domain. *Jpn. J. of Appl. Phys.*, 44:926–931, 2005.

[140] T.-R. Tsai, S.-J. Chen, C.-F. Chang, S.-Hs. Hsu, T.-Yu. Lin, and C.-C. Chi. Terahertz response of GaN thin films. *Opt. Express*, 14:4898–4907, 2006.

[141] S. R. Wenham and M. A. Green. Silicon solar cells. *Prog. in Photovolt.*, 4:3–33, 1996.

[142] J. Zhao, A. Wang, P. Altermatt, and M. A. Green. Twenty-four percent efficient silicon solar cells with double layer antireflection coatings and reduced resistance loss. *Appl. Phys. Lett.*, 66:3636–3638, 1995.

[143] J. Zhao, A. Wang, M. A. Green, and F. Ferrazza. 19.8% efficient "honeycomb" textured multicrystalline and 24.4% monocrystalline silicon solar cells. *Appl. Phys. Lett.*, 73:1991–1993, 1998.

[144] S. Pillai, K. R. Catchpole, T. Trupke, and M. A. Green. Surface plasmon enhanced silicon solar cells. *J. of Appl. Phys.*, 101:093105, 2007.

[145] B. Tian, X. Zheng, T. J. Kempa, Y. Fang, N. Yu, G. Yu, J. Huang, and C. M. Lieber. Coaxial silicon nanowires as solar cells and nanoelectronic power sources. *Nature*, 449:885–889, 2007.

[146] H. Jansen, M. de Boer, R. Legtenberg, and M. Elwenspoek. The black silicon method: a universal method for determining the parameter setting of a fluorine-based reactive ion etcher in deep silicon trench etching with profile control. *J. Micromech. Microeng.*, 5:115.

[147] T.-H. Her, R. J. Finlay, C. Wu, S. Deliwala, and E.c Mazur. Microstructuring of silicon with femtosecond laser pulses. *Appl. Phys. Lett.*, 73:1673–1675, 1998.

[148] Y. F. Tang, S. R. P. Silva, B. O. Boskovic, J. M. Shannon, and M. J. Rose. Electron field emission from excimer laser crystallized amorphous silicon. *Appl. Phys. Lett.*, 80:4154–4156, 2002.

[149] M.Z. Shaikh, K.A. O'Neill, S. Anthony, S.K. Persheyev, and M.J. Rose. Optical and electronic properties of HWCVD and PECVD silicon films irradiated using excimer and Nd:Yag lasers. *Thin Solid Films*, 501:125 – 128, 2006.

[150] Y. Fan, M. J. Rose, S.K. Persheyev, and M. Z. Shaikh. Excimer laser microstructuring of amorphous silicon films for electron field emission applications. *IEEE Conference eXpress. The 1st Symposium on Photonics and Optoelectronics (SOPO 2009), Wuhan, P. R. China*, 2009.

[151] Y. Fan, M. J. Rose, S.K. Persheyev, and M. Z. Shaikh. Fabrication of black silicon on glass substrates by excimer laser irradiation of thick a-Si:H films. *10th International Conference on Laser Ablation (COLA 2009), Singapore.*, 2009.

[152] M. Halim, A. Abdolvand, Y. Fan, S.K. Persheyev, C. Main, E. U. Rafailov, and M. J. Rose. Laser assisted microstructuring of amorphous silicon for microelectronics. *CLEO/QELS 2010 San Jose, California, USA*, 2010.

[153] S. K. Persheyev, Y. Fan, S. Reynolds, and M. J. Rose. Excimer laser wet oxidation of hydrogenated amorpheous silicon. *Phys. Stat. Sol. C*, 7:968–971, 2010.

[154] M. Stubenrauch, M. Fischer, C. Kremin, S. Stoebenau, A. Albrecht, and O. Nagel. Black silicon - new functionalities in microsystems. *J. Micromech. Microeng.*, 16:S82–S87, 2006.

[155] L. Sainiemi, H. Keskinen, M. Aromaa, L. Luosujärvi, K. Grigoras, T. Kotiaho, J. M Mäkelä, and S. Franssila. Rapid fabrication of high aspect ratio silicon nanopillars for chemical analysis. *Nanotechnology*, 18:505303.

[156] C. Dorrer and J. Rühe. Wetting of silicon nanograss: From superhydrophilic to superhydrophobic surfaces. *Adv. Mater.*, 20:159–163, 2008.

[157] S. Koynov, M. S. Brandt, and M. Stutzmann. Black nonreflecting silicon surfaces for solar cells. *Appl. Phys. Lett.*, 88:203107–3, 2006.

[158] L. L. Ma, Y. C. Zhou, N. Jiang, X. Lu, J. Shao, W. Lu, J. Ge, X. M. Ding, and X. Y. Hou. Wide-band "black silicon" based on porous silicon. *Appl. Phys. Lett.*, 88:171907.

[159] J.S. Yoo, I.O. Parm, U. Gangopadhyay, K. Kim, S.K. Dhungel, D. Mangalaraj, and J. Yi. Black silicon layer formation for application in solar cells. *Sol. Energy Mater. Sol. Cells*, 90:3085 – 3093, 2006.

[160] A. Serpenguezel, A. Kurt, I. Inanc, J. E. Cary, and E. Mazur. Luminescence of black silicon. *J. of Nanophoton.*, 2:021770, 2008.

[161] H. M. Branz, V. E. Yost, S. Ward, K. M. Jones, B. To, and P. Stradins. Nanostructured black silicon and the optical reflectance of graded-density surfaces. *Appl. Phys. Lett.*, 94:231121–3, 2009.

[162] H. C. Yuan, V. E. Yost, M. R. Page, P. Stradins, D. L. Meier, and H. M. Branz. Efficient black silicon solar cell with a density-graded nanoporous surface: Optical properties, performance limitations, and design rules. *Appl. Phys. Lett.*, 95:123501–3, 2009.

[163] A. A. Istratov, and E. R. Weber. Physics of copper in silicon. *J. Electrochem. Soc.*, 149:G21, 2002.

[164] R. N. Hall, and J. H. Racette. Diffusion and Solubility of Copper in Extrinsic and Intrinsic Germanium, Silicon, and Gallium Arsenide. *J. Appl. Phys.*, 35:379, 1964.

[165] P. Hoyer, M. Theuer, R. Beigang, and E.-B. Kley. Terahertz emission from black silicon. *Appl. Phys. Lett.*, 93:091106–3, 2008.

[166] Hi. Mimura and Y. Hatanaka. Energy-band discontinuities in a heterojunction of amorphous hydrogenated Si and crystalline Si measured by internal photoemission. *Appl. Phys. Lett.*, 50:326–328, 1987.

[167] C. H. Crouch, J. E. Carey, M. Shen, E. Mazur, and F. Y. Genin. Infrared absorption by sulfur-doped silicon formed by femtosecond laser irradiation. 79:1635–1641, 2004.

[168] W. B. Jackson, N. M. Amer, A. C. Boccara, and D. Fournier. Photothermal deflection spectroscopy and detection. *Appl. Opt.*, 20:1333–1344, 1981.

[169] H. Kataura, Y. Kumazawa, Y. Maniwa, I. Umezu, S. Suzuki, Y. Ohtsuka, and Y. Achiba. Optical properties of single-wall carbon nanotubes. *Synth. Met.*, 103:2555 – 2558, 1999.

[170] O. Vetterl, F. Finger, R. Carius, P. Hapke, L. Houben, O. Kluth, A. Lambertz, A. Mück, B. Rech, and H. Wagner. Intrinsic microcrystalline silicon: A new material for photovoltaics. *Sol. Energy Mater. Sol. Cells*, 62:97 – 108, 2000.

[171] D. S. Knight and W. B. White. Characterization of diamond films by Raman spectroscopy. *J. of Mater. Res.*, 4:385–393.

[172] M. S. Dresselhaus, G. Dresselhaus, A. Jorio, A. G. Souza Filho, and R. Saito. Raman spectroscopy on isolated single wall carbon nanotubes. *Carbon*, 40:2043 – 2061, 2002.

[173] I. de Wolf. Micro-Raman spectroscopy to study local mechanical stress in silicon integrated circuits. *Semicond. Sci. Technol.*, 11:139–154, 1996.

[174] W. J. Zhang and S. Matsumoto. Investigations of crystallinity and residual stress of cubic boron nitride films by Raman spectroscopy. *Phys. Rev. B*, 63:073201, 2001.

[175] A. S. Nielsen, D. N. Batchelder, and R. Pyrz. Estimation of crystallinity of isotactic polypropylene using Raman spectroscopy. *Polymer*, 43:2671 – 2676, 2002.

[176] L. Fekete, P. Kuzel, H. Nemec, F. Kadlec, A. Dejneka, J. Stuchlik, and A. Fejfar. Ultrafast carrier dynamics in microcrystalline silicon probed by time-resolved terahertz spectroscopy. *Phys. Rev. B*, 79:115306–13, 2009.

[177] R. Tsu, J. Gonzalez-Hernandez, S. S. Chao, S. C. Lee, and K. Tanaka. Critical volume fraction of crystallinity for conductivity percolation in phosphorus-doped Si:F:H alloys. *Appl. Phys. Lett.*, 40:534–535, 1982.

[178] E. Bustarret, M. A. Hachicha, and M. Brunel. Experimental determination of the nanocrystalline volume fraction in silicon thin films from Raman spectroscopy. *Appl. Phys. Lett.*, 52:1675–1677, 1988.

[179] V. T. Srikar, A. K. Swan, and M. S. Ünlü. Micro-Raman measurement of bending stresses in micromachined silicon flexures. *J. of Microelectomech. Syst.*, 12:779–787, 2003.

[180] X. Wu, J. Yu, T. Ren, and L. Liu. Micro-Raman spectroscopy measurement of stress in silicon. *Microelectron. J.*, 38:87–90, 2007.

[181] Y. Kobayashi, M. Nakamura, and T. Suzuki. Effect of heat treatment on residual stress and electron hall mobility of laser annealed silicon-on-sapphire. *Appl. Phys. Lett.*, 40:1040–1042, 1982.

[182] D. Bersani, P. P. Lottici, and X.-Z. Ding. Phonon confinement effects in the raman scattering by TiO_2 nanocrystals. *Appl. Phys. Lett.*, 72:73–75, 1998.

[183] R.-P. Wang, G.-W. Zhou, Y.-L. Liu, S.-H. Pan, H.-Z. Zhang, D.-P. Yu, and Z. Zhang. Raman spectral study of silicon nanowires: High-order scattering and phonon confinement effects. *Phys. Rev. B*, 61:16827–16832, 2000.

[184] A.V. Vasudevan Nampoothiri and S.L. Dexheimer. Ultrafast conductivity in amorphous semiconductors by time-resolved THz spectroscopy. *Conference on Lasers and Electro-Optics, 2004. (CLEO)*, 1:2, 2004.

[185] S. Komuro, Y. Aoyagi, Y. Segawa, S. Namba, A. Masuyama, H. Okamoto, and Y. Hamakawa. Carrier dynamics at surface and interface in hydrogenated amorphous silicon observed by the transient grating method. *Appl. Phys. Lett.*, 43:968–970, 1983.

[186] A. Esser, K. Seibert, H. Kurz, G. N. Parsons, C. Wang, B. N. Davidson, G. Lucovsky, and R. J. Nemanich. Ultrafast recombination and trapping in amorphous silicon. *Phys. Rev. B*, 41:2879 LP – 2884, 1990.

[187] S. Piscanec, M. Cantoro, A. C. Ferrari, J. A. Zapien, Y. Lifshitz, S. T. Lee, S. Hofmann, and J. Robertson. Raman spectroscopy of silicon nanowires. *Phys. Rev. B*, 68:241312, 2003.

[188] P. Uhd Jepsen, W. Schairer, I. H. Libon, U. Lemmer, N. E. Hecker, M. Birkholz, K. Lips, and M. Schall. Ultrafast carrier trapping in microcrystalline silicon observed in optical pump-terahertz probe measurements. *Appl. Phys. Lett.*, 79:1291–1293, 2001.

[189] P. Van Espen, H. Nullens, and F. Adams. An in-depth study of energy-dispersive x-ray spectra. *X-Ray Spectrom.*, 9:126–133, 1980.

[190] http://xdb.lbl.gov/.

[191] J. Weber, H. Bauch, and R. Sauer. Optical properties of copper in silicon: Excitons bound to isoelectronic copper pairs. *Phys. Rev. B*, 25:7688–7699, 1982.

[192] K. Graff and H. Pieper. Degradation of carrier lifetime in silicon crystals at room temperature. *Phys. Stat. Sol. (a)*, 49:137–144, 1978.

[193] S. J. Pearton and A. J. Tavendale. The electrical properties of deep copper- and nickel-related centers in silicon. *J. of Appl. Phys.*, 54:1375–1379, 1983.

[194] C. B. Collins and R. O. Carlson. Properties of silicon doped with iron or copper. *Phys. Rev.*, 108:1409–1414, 1957.

[195] J. P. Pouget, M. E. Jozefowicz, A. J. Epstein, X. Tang, and A. G. MacDiarmid. X-ray structure of polyaniline. *Macromolecules*, 24:779–789, 1991.

[196] K. Chen, X. Huang, J. Xu, and D. Feng. Visible photoluminescence in crystallized amorphous Si:H/SiN_x:H multiquantum-well structures. *Appl. Phys. Lett.*, 61:2069–2071, 1992.

[197] L. Guo, M. Kondo, M. Fukawa, K. Saitoh, and A. Matsuda. High rate deposition of microcrystalline silicon using conventional plasma-enhanced chemical vapor deposition. *Jpn. J. Appl. Phys.*, 37:L1116–L1118, 1998.

Publications

The author of this thesis has contributed in the following journal publication, conference contributions and book chapters during his PhD. project.

Journal publications

H. P. Porte, P. Uhd Jepsen, N. Daghestani, E. U. Rafailov, and D. Turchinovich, "Ultrafast release and capture of carriers in InGaAs/GaAs quantum dots observed by time-resolved terahertz spectroscopy", Appl. Phys. Lett. **94**, 262104 (2009).

H. P. Porte, D. Turchinovich, S. Persheyev, Y. Fan, M. J. Rose, and P. Uhd Jepsen, "Effect of copper on the carrier lifetime in black silicon", J. Infrared Milli. Terahz. Waves **32**, 883 (2011)

Conference contributions

H. P. Porte, D. Turchinovich, D. G. Cooke, and P. Uhd Jepsen, "Ultrafast carrier dynamics in InGaN/GaN multiple quantum wells", 1st Nordic Meeting in Physics. Kgs. Lyngby (2009) (talk).

D. Turchinovich, H. P. Porte, N. Daghestani, K. G. Wilcox, E. U. Rafailov, and P. Uhd Jepsen, "Capture and release of carriers in InGaAs/GaAs quantum dots", J. of Physics: Conference Series **193** 012085 (2009). Presented at: 16th International Conference on Electron Dynamics In Semiconductors, Optoelectronics and Nanostructures. Montpellier, France, (2009) (proceedings + poster).

H. P. Porte, D. Turchinovich, D. G. Cooke, and P. Uhd Jepsen, "Terahertz study of ultrafast carrier dynamics in InGa/GaN multiple quantum wells", J. of Physics: Conference Series **193** 012085 (2009). Presented at: 16th International Conference on Electron Dynamics In Semiconductors, Optoelectronics and Nanostructures. Montpellier, France, (2009) (proceedings + poster).

H. P. Porte, P. Uhd Jepsen, N. Daghestani, E. U. Rafailov, and D. Turchinovich, "Observation of trapping and release of carriers in InGaAs/GaAs quantum dots by ultrafast THz spectroscopy", 22nd Annual Meeting of the IEEE Photonics Society. Antalya, Turkey, (2009) (talk).

H. P. Porte, D. Turchinovich, D. G. Cooke, and P. Uhd Jepsen, "Transient photoconductivity in InGaN/GaN multiple quantum wells, measured by time-resolved terahertz spectroscopy", 22nd Annual Meeting of the IEEE Photonics Society. Antalya, Turkey, (2009) (talk).

D. Turchinovich, H. P. Porte, D. G. Cooke, and P. Uhd Jepsen, "Ultrafast conductivity dynamics in optically excited InGaN/GaN multiple quantum wells, observed by transient THz spectroscopy", Proceedings of SPIE, **7600**, 76001W (2010). Presented at: Photonics West. San Francisco, CA, USA (2010) (proceedings + poster).

H. P. Porte, D. Turchinovich, P. Uhd Jepsen, S. Persheyev, Y. Fan, and M. J. Rose, "Time-resolved terahertz spectroscopy of black silicon", International Conference on Infrared, Millimeter and THz Waves, Rome, Italy (2010) (talk).

H. P. Porte, D. Turchinovich, S. Persheyev, Y. Fan, M. J. Rose, and P. Uhd Jepsen, "Effects of copper on the carrier dynamics in black silicon", International Workshop on Optical Terahertz Science and Technology, Santa Barbara, USA (2011) (talk).

Book chapters

K. Iwaszczuk, H. P. Porte, R. K. Olsson, D. G. Cooke, D. Turchinovich, and P. Uhd Jepsen, "Terahertz technology: terahertz sources and detectors", in: "Beyond optical horizons: today and tomorrow with photonics", pp. 113-129, 1 ed. - Kgs. Lyngby : DTU Fotonik (2009)

Acknowledgements

Although sometimes the work as a PhD-student can be lonely, a lot of people have in many different ways contributed to this work and I would like to thank them for that.

First of all my supervisors, Peter Uhd Jepsen and Dmitry Turchinovich for giving me the opportunity to perform my PhD-study in the terahertz technology group at DTU Fotonik - Department of Photonics Engineering, Technical University of Denmark. Furthermore, I thank them for their help with many scientific challenges and the interesting discussions. A learned a lot about terahertz technology and semiconductor physics from you.

I would like to thank all the current and former group members of the terahertz technology group. I would like to mention a few in particular. David G. Cooke, although officially not my supervisor, always open to help with anything, especially with any problems in the lab. Krzysztof Iwaszczuk, who started his PhD. about the same time as me. Thanks for all the good discussions both scientific and nonscientific and for proofreading the manuscript of this theses. Good luck with the final phase of your PhD. Uffe Møller also for proofreading the manuscript of this thesis and Jonas Christian Due Buron for translating the abstract into Danish. Furthermore, I want to thank Binbin Zhou for his help in fixing the laser many times and for the many off-topic discussions in the lab while I was waiting for my measurement. I hope, I did not kept you too much from your work. Besides the group members, I would like to thank the technical and administrative staff at DTU Fotonik.

Part of the work in this thesis was done outside DTU Fotonik and the people involved deserves a special acknowledgement. Firstly, the people from the School of Engineering, Physics and Mathematics, University of Dundee and especially Saydulla Persheyev for producing the black silicon samples, taking some of the scanning electron images, performing the Raman spectroscopy experiments, and many discussions about black silicon.

I am grateful to Martin Meedom Nielsen from Risø DTU - National Laboratory for Sustainable Energy, Technical University of Denmark for letting

me use his X-ray diffraction spectrometer and with the help in analyzing the results.

Thanks to the people from DTU CEN - Center of Electron Nanoscopy, Technical University of Denmark who made the electron microscopy experiments possibly. A special thanks to Adam Fuller, Thomas Willum Hansen, and Berit Wenzell for introducing me to the different electron microscopes.

Finally, I want to thank the people who kept me from my work. The people at the Fotonik Friday Bar, which always gave me an excellent start of the weekend, my other friends outside DTU and last but least my family, who have always supported me.